TECHNISCHE UNIVERSITÄT MÜNCHEN

Lehrstuhl für Technische Chemie II

Bifunctional Ni/Zeolite Catalysts for Hydrodeoxygenation of Microalgae Oil and Lignin

Wenji Song

Vollständiger Abdruck der von der Fakultät für Chemie der Technischen Universität München zur Erlangung des akademischen Grades eines

Doktors der Naturwissenschaften (Dr. rer. nat.)

genehmigten Dissertation.

Vorsitzender:　　　　Univ.–Prof. Dr. Dr. h. c. B. Rieger

Prüfer der Dissertation:

　　　　　　1.　Univ.–Prof. Dr. J. A. Lercher

　　　　　　2.　Univ.–Prof. Dr. F. E. Kühn

Die Dissertation wurde am 17.03.2015 bei der Technischen Universität München eingereicht und durch die Fakultät für Chemie am 21.05.2015 angenommen.

For the loving memory of my grandmother, Cuizhen Fang

"Education is what remains after one has forgotten everything he learned in school."

Albert Einstein (1879 – 1955)

Acknowledgements

This doctoral thesis has come to a successful completion, with the help of many people during the endeavor. My sincere gratitude goes to all the members from the Chair of Technical Chemistry II at Technische Unviersität München.

First and foremost, I am deeply grateful to Professor Dr. Johannes A. Lercher for his patient guidance and unconditional support. Despite of his tight schedules, Johannes has always made himself available when I have doubts and concerns. It has been a nice experience to do my Ph. D. thesis under his supervision and to learn from his research expertise.

Next, I would like to thank my former supervisor Prof. Dr. Chen Zhao, who continues to contribute valuable feedback, advice and encouragement throughout my research work while also giving me the freedom to pursue various projects that I have been interested in.

I am also very thankful to Prof. Dr. Andreas Jentys for his scientific advice and insightful discussions, as well as Dr. Eszter Baráth for being my mentor in the last phase of my graduation study.

My colleagues, Dr. Hui Shi, Dr. Sonja Wryzgol, Elisabeth Hanrieder and Linus Schulz, who spared their time to perform TEM and TPD measurements for my samples, I acknowledge your contributions. And special thanks to my co-worker Yuanshuai Liu, who has consistently shared his knowledge with me. I value our academic collaboration and friendship forged over the years.

The technical and administrative staffs of TCII have been very kind and helpful, and I would like to acknowledge all of them here. I thank Xaver Hecht for the numerous BET and hydrogen chemisorption measurements and for solving technical problems whenever I approach him. Martin Neukamm, who has helped with AAS and SEM measurements, and extended his support in the order of chemicals and labwares. I also thank Andreas Marx, for his efforts with all the electronic devices. I am grateful to our nice secretaries, Steffi Maier, Bettina Federmann, Ulrike Sanwald, Helen Lemmermöhle and Karen Schulz, for their great assistance with all the miscellaneous administrative matters.

Furthermore, I would like to express my gratitude to our privileged research partners from Pacific Northwest National Laboratory (United States). I am indebted to Dr. Donghai Mei, for the DFT calculations and wonderful collaborations on octadecanol dehydration. I also thank Dr. Donald M. Camaioni, Dr. John L. Fulton, Dr. Aleksei Vjunov and Zizwe A. Chase, for the support and cooperation during the EAXFS measurements at Argonne National Laboratory.

I am very grateful to the members of biomass group, Dr. Baoxiang Peng, Dr. Jiayue He, Yuchun Zhi, Stanislav Kasakov, Sebastian Foraita, Guoju Yang, Moritz Schreiber, Yang Song, Peter Hintermeier, Sebastian Eckstein, Marco Peroni, Martina Braun, Manuel Wagenhofer, for all the insightful discussions; as well as the present and former colleagues of TCII: Dr. Oliver Gutiérrez, Dr. Erika Ember, Dr. Maricruz Sanchez-Sanchez, Bo Peng, Navneet Gupta, Kai Sanwald, Sebastian Müller, Eva Schachtl, Yu Lou, Dr. Wenhao Luo, Dr. Yue Liu, Maximilian Hahn, Matthias Steib, Jennifer Hein, Claudia Himmelsbach, Dr. Despina Tzoulaki, Dr. Stefanie Simson, Dr. Jeongnam Kim, Dr. Robin Kolvenbach, Dr. John Ahn, Dr. Yanzhe Yu, Dr. Luis Francisco Gonzalez Peña, Dr. Yulia Martynova, as well as my loving friends whose names are not mentioned here, for their friendship and all the great times that we have shared.

Last, but not least, I owe a great debt of thanks to my family for their love and sacrifices. My parents have offered me unconditional understanding and support in every possible way, holding faith in me and sticking by my side years by years. Without them, this thesis would never have been possible. My beloved grandmother, Cuizhen Fang, unfortunately would not be able to see my graduation. Her roles in my life were, and remain, immense. My love and gratitude for her can hardly be conveyed in words, I dedicate this thesis to my grandma:

外婆，我爱你。

Many thanks to all of you, Wenji

Mar. 2015

Abbreviations

Å	Angstrom
AAS	Atomic absorption spectroscopy
BAS	Brønsted acid site
BET	Brunauer-Emmett-Teller
CO	Carbon monoxide
DFT	Density Functional theory
DP	Deposition-precipitation
FAME	Fatty acid methyl ester
GC	Gas chromatography
h	Hour
HC	Hydrocarbon
HDO	Hydrodeoxygenation
IR	Infrared
K	Kelvin
(k)J	(Kilo) joule
(k)Pa	(Kilo) pascal
kV	Kilovolt
LAS	Lewis acid site
(m)L	(Milli) liter
min	Minute
nm	Nanometer
NMR	Nuclear magnetic resonance
NP(s)	Nanoparticle(s)
TEM	Transmission electron microscopy
TOF	Turn over frenquency
TPR	Temperature programmed reduction
wt.%	Weight percent
XRD	X-ray diffraction

Abstract

Synergistic effects between proximal metal and acid sites in zeolites have been studied with respect to elementary reactions of biomass conversion. Uniformity of Ni particles is crucial to prevent particle growth during hydrodeoxygenation (HDO). Bifunctional Ni/HZSM-5 at fixed metal loading catalyzes phenol HDO, with a rate increasing in proportion to the Brønsted acid site concentration. Activities of acid site catalyzed dehydration and alkylation of alcohols and phenols not only scale with the concentrations of Brønsted and Lewis acid sites, but also depend on the synergy between them.

Kurzzusammenfassung

Synergistische Effekte der räumlichen Nähe von Metall und Säurezentren in Zeolithen wurden in Bezug auf elementare Reaktionen bei der Umsetzung von Biomasse untersucht. Identische Größe von Ni Partikeln ist wichtig um deren Wachstum während der Hydrodeoxygenierung (HDO) zu verhindern. Bei konstanter Metallbeladung katalysiert bifunktioneller Ni/HZSM-5 Phenol HDO mit einer Rate, die proportional zur Brønstedsäure Konzentration ansteigt. Die Aktivitäten der säurekatalysierten Dehydratisierung und Alkylierung von Alkoholen und Phenolen hängen nicht nur von den Konzentrationenen der Brønsted- und Lewis-Säurezentren ab, sondern auch deren Synergie.

Table of contents

CHAPTER 3

3. **Dehydration of 1-Octadecanol over H-BEA: A Combined**

   Experimental and Computational Study………………………….**55**

CHAPTER 6

CHAPTER 7

Chapter 1

Introduction

1.1. General background

The global community, increasingly aware of declining petroleum reserves, expanding reliance on imported petrochemical feedstocks, as well as the rising environmental concerns on fossil fuel usage, is hence seeking renewable alternatives.[1] In this context, considerable research has focused on the development of economical and energy-efficient processes for producing higher value chemicals and energy from biomass resources, which appear to be the only current sustainable source of organic carbon.[2,3]

Renewable transportation fuels derived from biomass feedstock have the potential to reduce greenhouse gas emissions and diversify global fuel supplies.[4,5] Due to the importance of the transportation sector in our society, biofuel production worldwide has been rapidly growing since last century. Countries with large biomass resources, such as the United States, has set ambitious goals to derive 20% of liquid fuels from biomass by 2030.[6,7] The European Union has also identified renewable fuels as a sustainable contributor up to 20% of energy consumption by 2020.[8]

At present, triglycerides (oil), lignocellulose, and starch (including sugars) are the general classes of biomass derived feedstocks used for biofuel production. A more detailed classification is summarized in Table 1-1.[9] Among them, lignocellulosic material is the most abundant and an inexpensive nonedible biomass which can be converted into liquid fuels by three primary processes. The first two routes involve gasification or pyrolysis to produce upgradeable syn-gas and bio-oil, which can be subsequently refined toward transportation fuels. The third employs complicated hydrolysis process to break lignocellulose into its constituent units. Further conversion of sugar monomers and associated lignin intermediates lead to the production of liquid fuels of ethanol, gasoline, and diesel.[10] Another class of feedstocks with potential are energy crops having high energy densities that are easily converted into liquid fuels. Although vegetable oils are more expensive than lignocellulosic biomass and are limited by their quantities, biodiesel obtained from transesterification of rapeseed oil or other triglycerides with methanol (or ethanol) represents 80% of the current European biofuel market.[11]

Table 1-1. Characterization of feedstocks for biofuel production.[9]

Feedstock type	Classification	Sources
1. 1st generation	1. Food (energy) crops	1. Rapeseed, soybeans, sunflower seeds, canola, camelina, palm fruits, babassu kemel, coconut kernel, cotton seeds, wheat, barley, sugarcane, cassava, com/maize.
	2. Animal fats	2. Lard, animal intestines, animal parts.
2. 2nd generation	1. Agricultural residues	1. Lignocellulosic materials such as straw, grass, leaves, prunings, miscanthus, willow, com stover, rice husks, palm empty fruit bunches, etc.
	2. Forest residues	2. Lignocellulosic materials like wood chippings, branches, foliage, roots, etc.
	3. Animal and oil wastes	3. Animal manure, tallow, chicken fat, fish oils, waste cooking oil
	4. Nonfood (energy) crops	4. Jatropha seeds, soap nut seeds, mahua seeds (*Madhuca indica*), indian beech/pongame seeds (*Pongamia pinnata*), karanj seeds, castor beans, Hemp, etc.
	5. Biowastes streams	5. Municipal solid wastes (*e.g.*, kitchen/household wastes, construction wood wastes, packaging wastes, etc.), sewage sludge, industrial liquid wastes.
3. 3rd generation (green, brown and red algae)	1. Microalgae	1. Botryococcus, Chlamydomonas, chlorella, spirulina, etc.
	2. Macroalgae (macrophytes or seaweeds)	2. Cladophora, Spirogyra, Hydrodictyon, *Batracho spermum,* Halimeda, Maiden's Hair, Caulerpa, etc.

Currently, biodiesel and bioethanol are the primary alternatives to diesel or gasoline. While biodiesel is mainly obtained from transesterification process, bioethanol is primarily produced from edible biomass sources like corn or sugarcane by sugar fermentation. These biofuels suffer from several drawbacks, such as low oxidation stability, corrosive nature and poor flow properties, which limit their direct application as transportation fuels.[12,13] Therefore, development of new approaches for producing high energy density next-generation biofuels from nonedible feedstocks has been the subject of numerous research during the past decade. In this sense, heterogeneous catalysis is a key parameter to fulfil the promise of biofuels and improve the sustainability of chemical processes in general. In this thesis, bifunctional catalysts containing metal nanoparticles and zeolite acid sites are employed to investigate the transformations of platform molecules including triglyceride, fatty acid and phenolic compounds.

1.2. Triglyceride feedstocks

1.2.1. Potential of microalgae

Table 1-2. Comparison of common sources of biodiesel.[14]

Crop	Oil yield (L/ha)	Land area needed (M ha) [a]	Percent of existing US cropping area [a]
Corn	172	1540	846
Soybean	446	594	326
Canola	1190	223	122
Jatropha	1892	140	77
Coconut	2689	99	54
Oil palm	5950	45	24
Microalgae [b]	136.900	2	1.1
Microalgae [c]	58.700	4.5	2.5

[a] For meeting 50% of all transport fuel needs of the United States.

[b] 70 wt.% oil in biomass. [c] 30 wt.% oil in biomass.

At present, biodiesel is primarily produced from oil crops, waste cooking oil and animal fat, whose availability is far below the potential market demand. These limitations have motivated the research in developing second generation biofuels based on non-edible feedstocks such as microalgae, lignocellulosic materials, agricultural residues, and systematically grown energy crops, which offer great potential in the longer term. Table 1-2 presents a comparison of microalgae with other common feedstocks used for biodiesel production.

Among them, microalgae appear to be a promising source that is capable of meeting the large scale demand for renewable biodiesel. The oil productivity of microalgae greatly exceeds that of many conventional agricultural crops, requiring much less land area, up to 132 times less compared to soybeans, for a 30 wt.% oil content in algae biomass. They grow extremely fast and commonly double their biomass within 24 hours.[15] Cultivation of microalgae is considered socially and environmetally benign, as they don't compete for arable land or fresh water supply for human consumption.[16]

1.2.2. Conventional technologies for triglyceride conversion
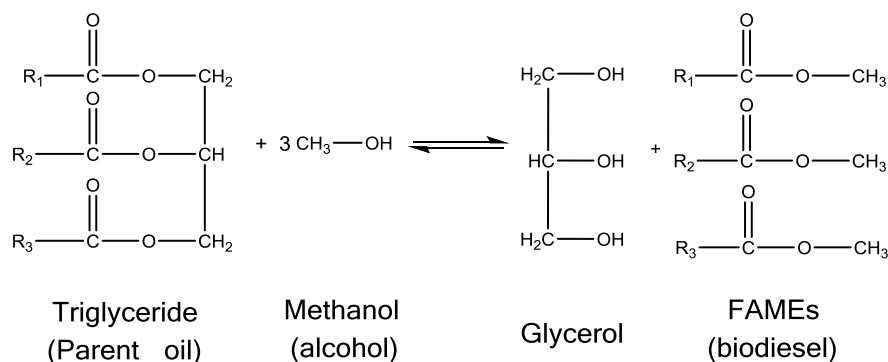
Scheme 1-1. Transesterification of triglycerides with methanol

Biodiesel produced from transesterification of triglycerides is the main alternative to diesel fuel in EU, and it is still growing in Europe, Brazil, and United States. The reaction consists of three consecutive reversible reactions, with diglycerides and monoglycerides as intermediates, and finally towards the production of fatty acid methyl esters (FAMEs) and glycerol. The overall reaction is shown in Scheme 1-1. Transesterification can be

catalyzed by acids, alkalis[17,18] or enzymes.[19] The homogeneous alkaline catalysts such as sodium methoxide is the most widely used commercial catalyst for biodiesel production at a concentration of about 1 wt.%. [17]

Although most of the current biodiesels are produced through transesterification process, these FAMEs suffer from relative high oxygen content and low heating value which limits their application as high grade fuels.[20] In this sense, catalytic deoxygenation through decarboxylation, decarbonylation or hydrodeoxygenation routes are employed to convert fatty acids and triglycerides into diesel range hydrocarbons. It has been shown that stearic acid can be nearly completely transformed into linear C_{17} alkanes over commercial Pd/C catalyst at 573 K under 17 bar of 5% H_2 in argon. The deoxygenation rates of various metals decrease in the sequence of Pd > Pt > Ni > Rh > Ir > Ru > Os.[21] Though noble metals are highly active for the selective conversion of fatty acids toward desired alkanes, large-scale industrial applications of these catalysts are economically infeasible due to their high prices. Moreover, their activities and selectivities are much lower when triglyceride feeds are directly applied.

Alternatively, parent oil can be upgraded using conventional hydrotreating catalysts by the existing petroleum refinery infrastructure. For instance, triglycerides can be hydrotreated with sulfided NiMo or CoMo at 623 – 723 K in presence of 40-150 bar H_2, producing straight chain alkanes (C_{12} to C_{18}),[20,22] which could be further isomerized over Pt/MCM41 into branched alkanes to lower the freezing point of the final product. This process has been commercialized by Neste Oil. The reaction involves, 1) hydrogenation of double bonds in the alkyl chain, 2) hydrogenolysis of the saturated triglycerides leading to the respective fatty acids and propane as a valuable byproduct, 3) deoxygenation of the formed fatty acids toward alkanes through decarboxylation, decarbonylation or via hydrodeoxygenation.[22] The drawbacks of such hydrotreating process lie in the usage of sulfided catalysts which contaminate the products through sulfur leaching, and sulfur containing compounds such as H_2S or DMDS have to be continuously fed during the reaction in order to keep the catalysts active. Therefore, it would be attractive to develop stable and non-sulfided catalysts based on lower costs transition metals for triglycerides conversion.

1.2.3. Hydrodeoxygenation of microalgae oil

Recently, Lercher group has reported a novel and sulfur-free catalyst, i.e., Ni nanoparticles supported on and in zeolite HBEA, which are able to quantitatively convert crude microalgae oil under mild conditions (533 K, 40 bar H_2) into diesel range alkanes as high-grade second generation biofuels.[23] The overall reaction pathway is illustrated in Scheme 1-2.

Scheme 1-2. Proposed reaction pathway for transformation of microalgae oil to alkanes over bifunctional Ni/HBEA catalysts. [23]

Hydrodeoxygenation of microalgae oil over Ni/HBEA has been proposed to proceed via an initial metal catalyzed hydrogenation of the double bonds in the alkyl chain, followed by hydrogenolysis of the formed saturated triglyceride leading to fatty acid and propane production. Subsequent hydrogenation of the carboxylic group of fatty acid leads to the corresponding aldehyde (octadecanal). Followed by either decarbonylation of octadecanal to produce *n*-heptadecane and carbon monoxide (minor route), or

hydrogenation of octadecanal to 1-octadecanol (major route). Acid catalyzed alcohol dehydration and metal catalyzed alkene hydrogenation produce the final *n*-octadecane.[23]

The cascade reactions require two catalytic functions, with metallic Ni sites responsible for the integrated steps of hydrogenolysis, hydrogenation and decarbonylation, while zeolite acid function catalyzes dehydration, hydroisomerization (and hydrocracking). Hydrogenation of the intermediately formed stearic acid has been determined to be the rate determining step, which is catalyzed by supported Ni nanoparticles (NPs).

However, these metal NPs are conventionally incorporated into zeolite framework by incipient wetness impregnation method, which usually leads to large and non–uniform Ni particles, and resultantly low hydrogenation activity.[24] Therefore, small and uniform Ni nanoparticles with high metal dispersion would be crucial to realize high activity and stability of the novel Ni/HBEA bifunctional catalyst during the hydrodeoxygenation of microalgae oil.

1.3. Lignocellulose derived feedstocks

1.3.1. Structure of lignocellulose biomass

Lignocellulosic materials represent the most abundant terrestrial biomass.[25] As shown in Figure 1-1, lignocellulose is mainly composed of cellulose (40-50%) which is a crystalline polymer of glucose; and hemicellulose (25-35%), an amorphous polymer containing mostly xylose units. Lignin comprises the remainder of biomass, it is a three-dimensional hetero-polymer consisting of methoxylated phenylpropane units responsible for the structure rigidity of plants.[26] Lignin fills the spaces between cellulose and hemicellulose in plant cell walls.
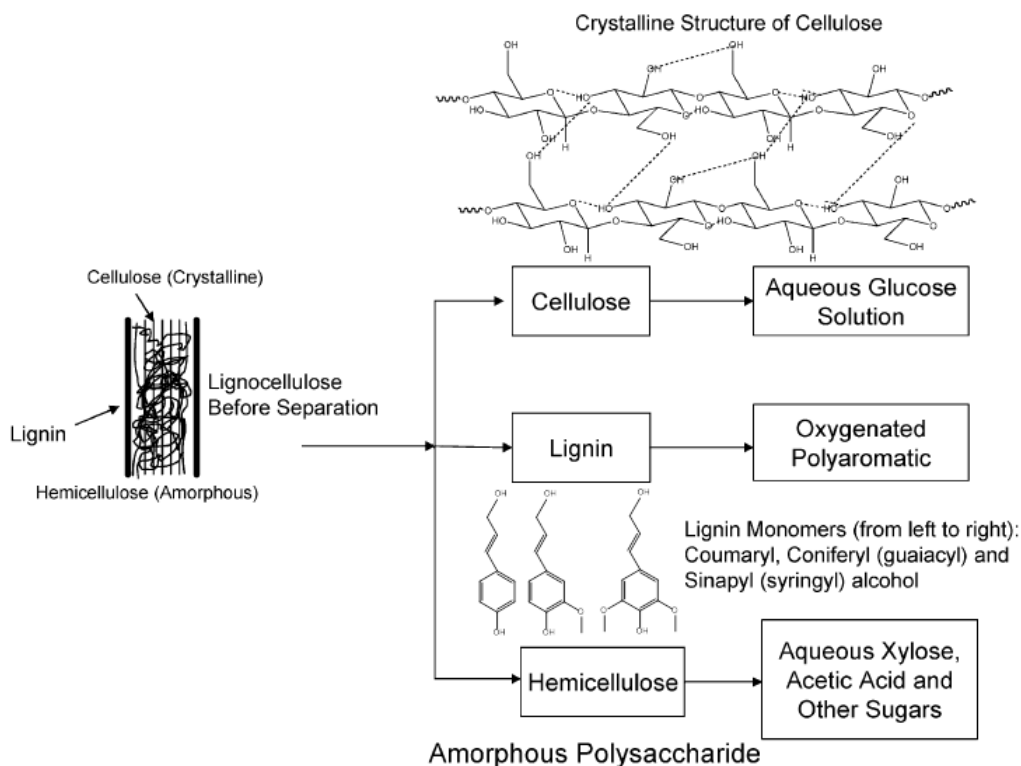
Figure 1-1. Structures of different biomass fractions (cellulose, hemicellulose and lignin).[27]

1.3.2. Technologies for lignocellulose conversion

Generally, targeted upgrading of cellulosic biomass involves an initial depolymerization step to produce smaller platform molecules, this could be achieved by thermochemical processes such as gasification, pyrolysis or liquefaction as discussed in section 1.1 (Figure 1-2). Apart from these, enzymatic hydrolysis is an alternative strategy for lignocellulose treatment. In this method, lignin and some hemicellulose fraction is first extracted at the pretreatment stage to increase the accessibility of cellulose and the remaining hemicellulose, which can be subsequently hydrolyzed by enzymes. However, the economic feasibility of the enzymes in industrial biorefineries is still under debate.[28]

Gasification is a well-established process which has been widely practiced to convert biomass, coal or other carbonaceous materials into syn-gas or producer gas. At present, commercial biomass gasification units mainly generate heat and electricity. The production of biofuel involves further conversion of syn-gas by Fischer-Tropsch synthesis (FTS) to produce diesel fuel, or through methanol synthesis.[4]
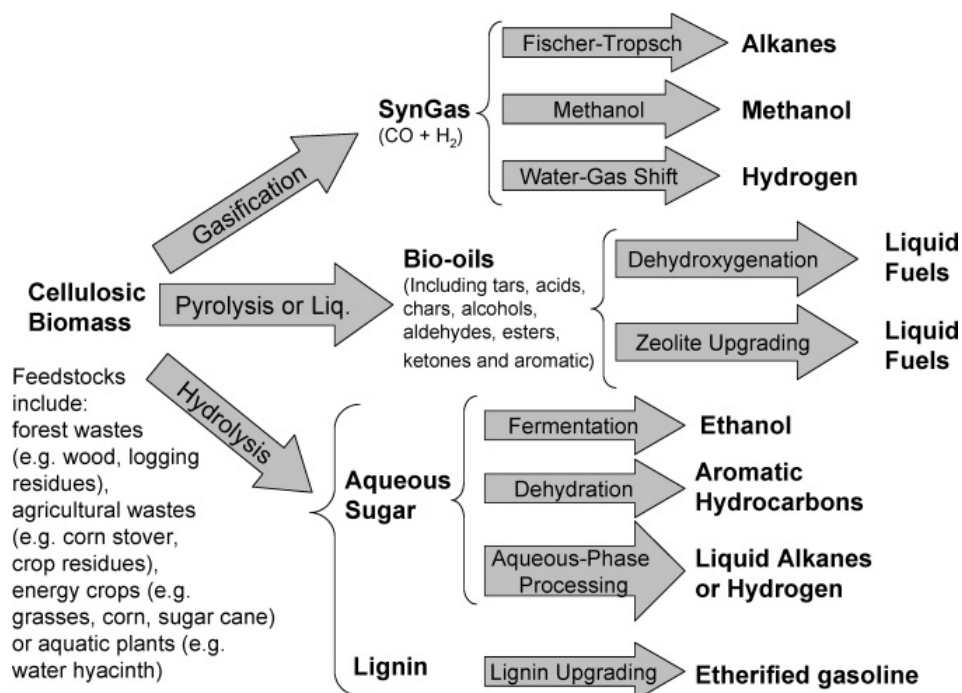
Figure 1-2. Strategies for biofuels production from lignocellulose.[10]

In addition to syn-gas, thermochemical treatment of biomass can also produce liquids and solids depending on processing parameters. Generally, short residence times, fast heating rates, and moderate temperatures favour liquids (bio-oil), and their compositions are non-thermodynamically controlled. The compounds present in bio-oil can vary drastically with diverse feedstock as well as different reaction and storage conditions.[29] Typical components found in bio-oil are shown in Figure 1-3. They are derived from fragmentation of the three key building blocks of lignocellulose, with oxygenates, sugars, and furans formed from the cellulose and hemicellulose fraction, and guaiacols and syringols from the lignin fraction.

It has been shown that lignin components in bio-oils mainly include coniferyl alcohol and sinapyl alcohol which are the first products from lignin pyrolysis, lower molecular weight compounds like guaiacol and catechol are formed later.[31] In this thesis, phenol, catechol and guaiacol are selected as the simplest model compounds to elucidate the integrated reaction pathways occurred during the upgrading of lignin derived bio-oil.
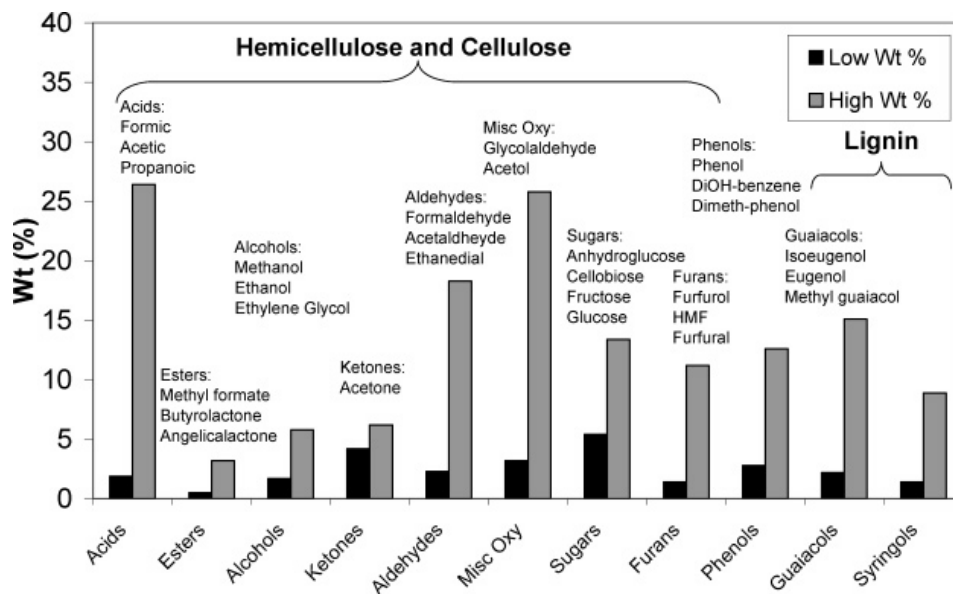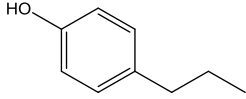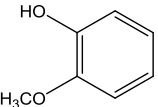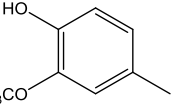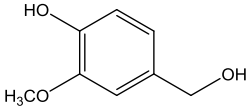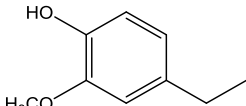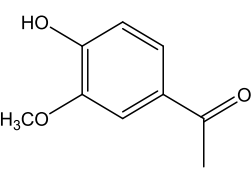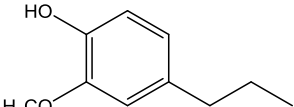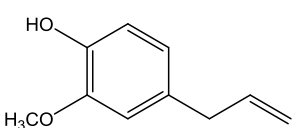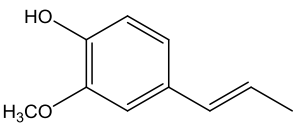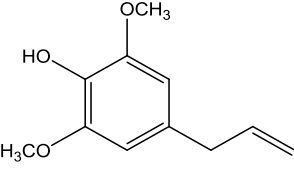
Figure 1-3. Chemical composition of bio-oils according to Milne et al.[30]

1.3.3. Bio-oil upgrading

The main concerns for direct applications of bio-oil are difficult ignition due to low heating value, corrosiveness resulted from the acid components, and coking problems due to thermally unstable oxygenates.[32] In this contest, hydrodeoxygenation is considered an effective method for bio-oil upgrading by reducing its oxygen content and functionality. Hydrodeoxygenation is normally carried out at $573 - 872$ K at the presence of high H_2 pressure. During the reaction, oxygen containing compounds in bio-oils react with hydrogen to form water and saturated C-C bonds. Conventional hydrotreating catalysts such as Co or Ni-doped Mo sulfides are currently used. The problems associated with these sulfided catalysts have been discussed in section 1.2.2, which mainly concern products contamination and catalyst deactivation due to sulfur removal via a reverse Mars van Krevelen mechanism.[33]

Table 1-3. Hydrodeoxygenation of phenolic monomers on Ni/HZSM-5.[38]

Phenolic reactant	Conversion (%)	Selectivity (%)		
		cycloalkanes	aromatics	methanol
	100	92	8.0	-
	100	74	13	13
	100	73	15	12
	99	80	9.6	10
	99	79	10	11
	100	77	12	11
	98	84	6.0	10
	100	80	11	9.0
	100	79	12	9.0
	93	78	5.0	17

Reaction conditions: reactant (0.010 mol), 20 wt.% Ni/HZSM-5 (0.5 g), H_2O (80 mL), 523 K, 5 MPa H_2 (at ambient temperature), 2 h, stirred at 680 rpm.

Recently, Lercher group has reported reductive upgrading of lignin-derived phenolic oil toward C_6–C_9 gasoline-range hydrocarbons (naphthas/aromatics) in the aqueous phase under mild conditions (473 – 523 K).[34-40] The reaction relies on dual functional catalysts containing a metal (Pd or Ni) and an acid (H_3PO_4, Nafion/SiO_2, and HZSM-5). Water as an environmentally benign solvent is also beneficial for the separation of hydrocarbon products from the aqueous phase. A series of model compounds from lignin derived bio-oil including alkyl-, ketone-, or hydroxy-substituted phenols and guaiacols, as well as an alkylsubstituted syringol phenol were shown to be effectively hydrodeoxygenated over a 20 wt.% Ni/HZSM-5 catalyst to cycloalkanes (73–92%) and aromatics (5.0–15%), at 523 K and 5 MPa of H_2 (Table 1-3).[38] The ratio of cycloalkanes to aromatics is dependent on the relative extent of hydrogenation and dehydro-aromatization reactions, which can be altered by varying reaction conditions such as reaction temperature. With the bifunctional Ni/HZSM-5 catalyst, supported Ni particles catalyze hydrogenation and dehydro-aromatization reactions, while Brønsted acid sites of the zeolite are responsible for dehydration and hydrolysis steps.[34-36]

Hydrodeoxygenation reaction is undoubtedly important for the conversion of highly oxygenated compounds from bio-oil, nevertheless, it would also be interesting to combine such oxygen removal process with the adjustment of the molecular weight via C–C coupling of the reactive intermediates. This is especially important for the production of heavier hydrocarbons (diesel range) from sugar or phenolic components based bio-oil derived from lignocellulose biomass. In this context, our group also reported highly selective conversion of lignin derived C_6–C_9 phenolic oil to C_{12}–C_{18} hydrocarbons by combining hydrodeoxygenation and alkylation steps over Pd/C and zeolite H-BEA catalysts.[41] The produced bi- or tri-cycloalkanes are free of sulfur, oxygen, or polyaromatics which can be applied as high-grade bio-fuels. The overall reaction network is illustrated in Scheme 1-3, where phenol selectively reacts with the in-situ formed cyclohexanol or cyclohexene on Brønsted acid sites.

The selectivity of hydroalkylation depends on the relative concentrations of phenol and cyclohexanol produced from phenol hydrogenation, which are dependent on the rate of hydrogenation and the extent of reaction. Moreover, competing acid-catalyzed alkylation and dehydration of the cycloalcohol intermediate occur in parallel, hence in

order to reach high yields of alkylation products, it is necessary to optimally balance the rates of hydrogenation, dehydration, and alkylation steps in the cascade reactions by adjusting the concentrations of metal and acid sites in the dual functional catalyst.
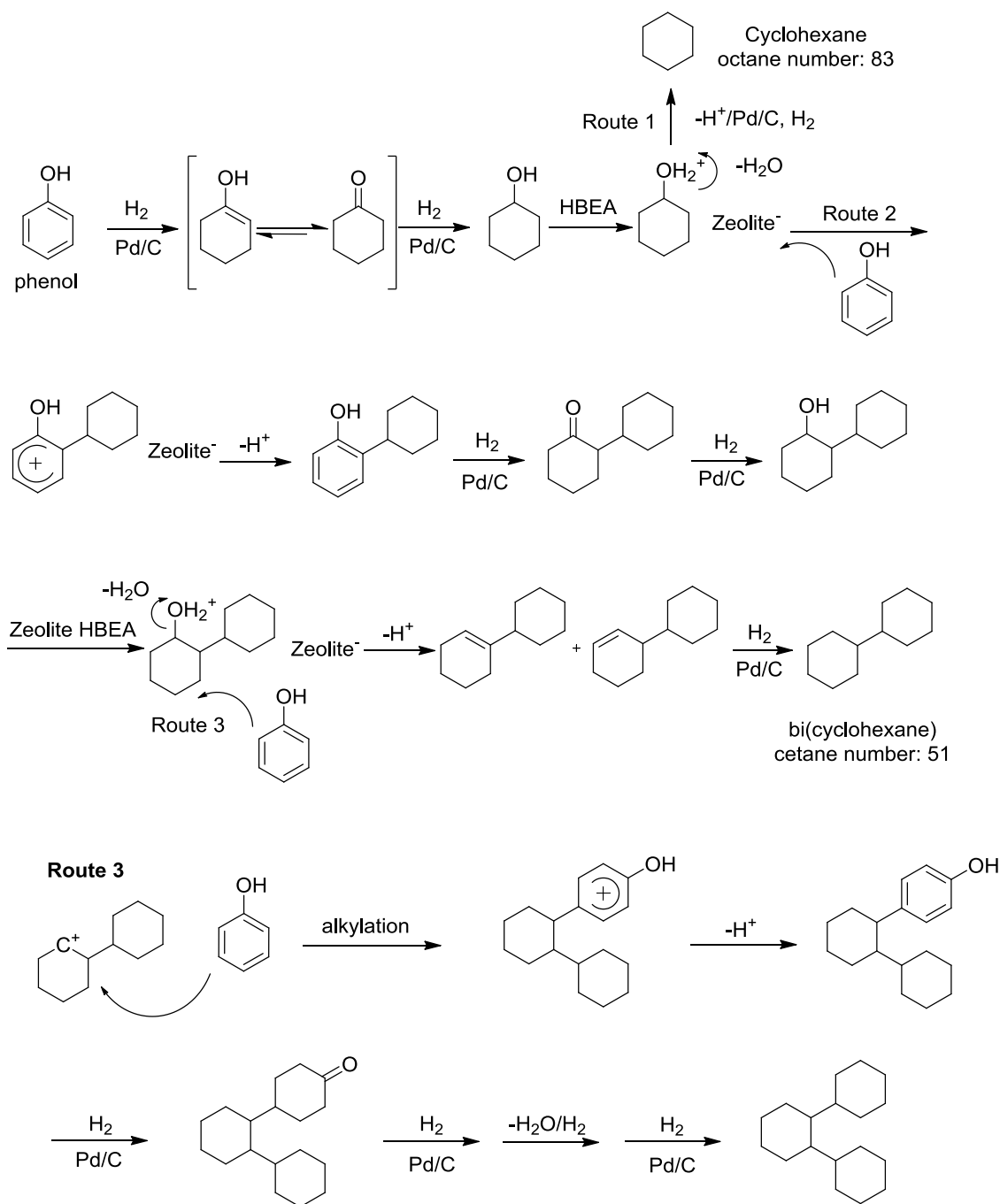
Scheme 1-3. Proposed reaction pathway for the formation of C_{12}, C_{18} hydrocarbons from phenol in presence of H_2, Pd/C, and HBEA catalysts.[41]

1.4. Bifunctional catalysts based on metal nanoparticles and zeolites

1.4.1. Applications of metal-acid bifunctional catalysts

In most cases, processing and upgrading of highly functionalized biomass molecules involves multistep conversion, it is hence desirable if solid catalysts can perform cascade reactions without the necessities of intermediates separation and purification. This would be possible with tailored design of multifunctional catalysts by integrating functions of various active sites. Design and optimization of multifunctional catalysts for the selective conversion of biomass into chemicals and biofuels has been widely investigated.[42-46] Incorporation of metal nanoparticles into solid acids enables the preparation of catalysts that combine the hydrogenation-dehydrogenation abilities of a metal and carbocation rearrangement functions of Brønsted or Lewis acid sites. In some cases, addition of a second metal is shown to be beneficial for catalyst performances in terms of activity, selectivity and stability,[46-48] this is not discussed in this thesis.

We have shown in the previous sections that platform molecules such as fatty acids and phenolic compounds can be converted to biofuels over metal-acid bifunctional catalysts in one-pot process. Selective oxygen removal can be achieved via acid catalyzed reactions including dehydration and hydrolysis in combination with metal catalyzed steps like hydrogenation, hydogenolysis and decarbonylation.[23,34-38] C-C bond coupling reactions such as alkylation which proceeds over Brønsted acid sites is also appealing for the production of heavier hydrocarbons from lignin derived $C_6−C_9$ phenolic oil.[41]

An extensively studied reaction sequence is hydrogenation/dehydration, which can be exemplified by aqueous phase hydrodeoxygenation of the simplest model compound, i.e. phenol over a Ni/HZSM-5 catalyst. The reaction pathway is shown in Scheme 1-4, in which phenol is first converted to cyclohexanol by sequential hydrogenation steps over Ni particles, subsequent dehydration of cyclohexanol on acid sites leads to the formation of cyclohexene which is in turn hydrogenated to produce saturated cyclohexane.
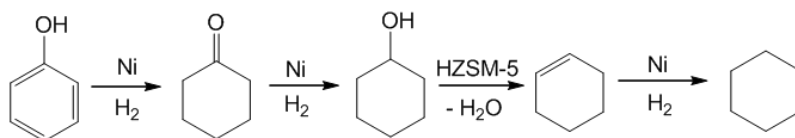
Scheme 1-4. Reaction pathway for phenol hydrodeoxygenation over Ni/HZSM-5 in the aqueous phase.[49]

1.4.2. Synthesis of Ni/zeolite bifunctional catalysts

A renewed interest for the preparation of supported nickel nanoparticles arouse as it represents an efficient catalyst for upgrading triglycerides feedstock and lignocellulose derived bio-oil.[23,38,50] While the performances of Pd- or Pt-catalysts are not strongly dependent on particle size,[51] the preparation of supported Ni catalyst is more demanding since very small particle size is required for an optimum catalytic activity due to its lower hydrogenation-dehydration abilities compared to noble metals.

Ni nanoparticles can be conventionally loaded in-/onto supports by impregnation (solvent evaporation or incipient wetness impregnation). In a typical synthesis, the solid support with defined pore volume is impregnated with an aqueous solution of metal salt (*e.g.*, nickel nitrate), the Ni(II) phase deposits on the support surface mainly via capillary adsorption. The catalyst precursor is then dried to get rid of excess amount of solution prior to calcination in air, when Ni oxides are formed and can be subsequently reduced by H_2 to obtain metallic Ni nanoparticles. Impregnation is convenient and easy to carry out, but the maximum metal loading attainable is dependent on the solubility of its precursor. The Ni particle size in the reduced catalyst is hard to control, and a wide size distribution is normally resulted.[24]

Ion exchange is an alternative method to prepare supported metal catalyst, as zeolites can accommodate a wide variety of cations including Na^+, K^+, Ca^{2+}, Mg^{2+}, which are readily exchangeable for mobile metal ions from an external salt solution.[52] Compared with impregnation, ion exchange is more reproducible to obtain small and uniform metal nanoparticles, due to the strong interaction of metal cations with negative oxygens in the support which resembles the formation of a coordination bond.[53] However, the

maximum metal loading that can be achieved through ion exchange is generally low and is limited by the exchange capacity of the zeolite material.

In this sense, the deposition-precipitation (DP) method developed by Geus et al.[54,55] has been envisioned as a promising approach to achieve high Ni dispersion at relatively high loading. During the synthesis, zeolite supports are suspended in a solution containing nickel precursor salts, which precipitate through basification of the suspension by Urea ($CO(NH_2)_2$). Hydroxide ions are gradually and homogeneously generated via urea hydrolysis at elevated temperature, such that local super-saturation and the sole precipitation of Ni hydroxide are avoided. The advantages of the DP method include higher achievable metal loading compared to ion exchange approach, as well as small Ni particles with narrow size distributions which are also sintering resistant due to the metal-support interaction.[56-58]
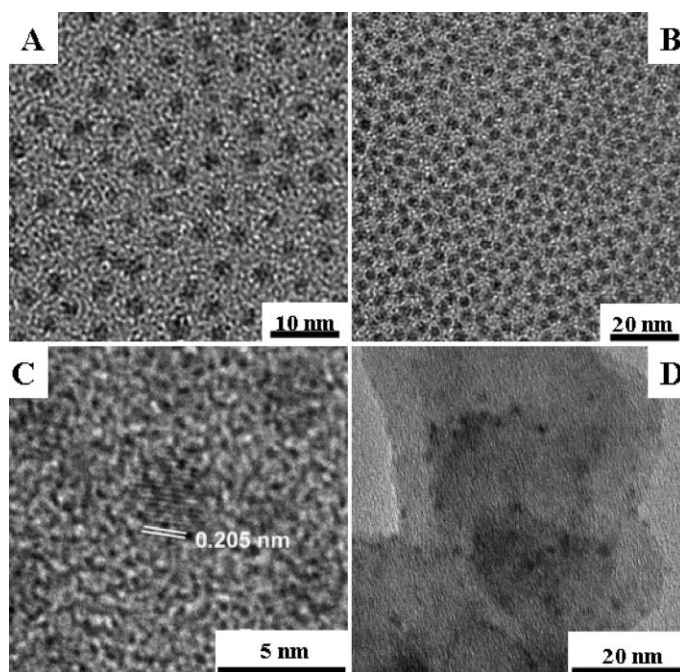
Figure 1-4. TEM images of (A)-(C) the 3.2 nm Ni NPs synthesized in solution phase, and (D) the 3.2 nm Ni NPs deposited on carbon support.[61]

Apart from reduction treatment of the catalyst precursor by H_2, solution phase synthesis of metallic nanoparticles represents a robust route to prepare monodispersed Ni NPs. The procedure normally involves reduction of Ni(II) precursors in the presence of

amine and/or carboxylic acid,[59] or strong reducing agent such as borohydride derivatives.[60] Surfactants that strongly bind to Ni are required, which are generally detrimental to the catalytic activities of the nanoparticles. It is recently reported that Ni NPs can be synthesized by reducing Ni(II) acetylacetonate with a borane tributhylamine complex in the presence of oleylamine and oleic acid acting as solvent and surfactant. Sub-10 nm NPs have been formed (Figure 1-4) and showed high activities on hydrolytic dehydrogenation of the ammonia borane complex even without necessities to remove the surfactants.[61]

The above discussed synthesis methods have been well developed and widely used to prepare supported or colloidal metal nanoparticles. Nevertheless, applications of these approaches for the synthesis of metal-acid bifunctional catalysts in the context of selective conversion of biomass feedstocks into transaportation fuels are scarce. Therefore, they will be the subjects of interests in the second chapter of this thesis.

1.5. Scope of this thesis

The major purpose of this dissertation is preparation of bifunctional catalysts based on small and uniform nickel nanoparticles and zeolites (Figure 1-5), and their applications for the hydrodeoxygenation of biomass derived platform molecules including fatty acids and phenolic compounds. Meanwhile, the individual and cooperative roles of metal and acid sites are explored by studying the kinetics of reactants and intermediates conversion.

Figure 1-5. Schematic illustration of Ni NPs supported on and/or in zeolite pores.

In the second chapter of this thesis, alternative synthetic methods including Ni NP, DP and ion-exchange have been employed to synthesize Ni nanoparticles sup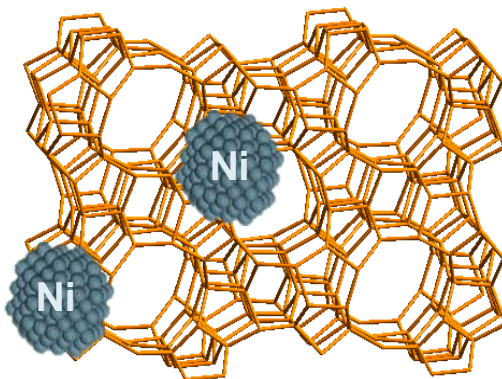ported on HBEA zeolite. The improved catalysts have been extensively characterized and compared with that prepared by conventional impregnation technique. The significance of small size and good size uniformity of the metal nanoparticles are highlighted in terms of catalyst activity and stability for the hydrodeoxygenation of stearic acid and microalgae oil.

After detailed investigation and optimization of nickel catalyzed steps, dehydration of the intermediately formed 1-octdecanol during the cascade reactions of microalgae oil conversion is explored with a combined experimental and computational method. The impacts of acid sites' distribution on the overall activity and selectivity of the long chain alcohol dehydration are demonstrated experimentally. The parallel intra- and inter-molecular dehydration pathways with different activation energies are studied by density functional theory (DFT) calculations, with the roles of steric constraints imposed by the uniform microporous structure of BEA also discussed.

In the following chapter, bifunctional Ni/HZSM-5 catalyst prepared by the improved method is applied for the hydrodeoxygenation of phenol, catechol and guaiacol. The detailed kinetics including individual reaction steps towards the formation of targeted cycloalkanes are described. The synergistic effects of Ni and acid sites during hydrogenation and C–O bond cleavage reactions are also addressed.

Apart from hydrodeoxygenation, aqueous phase hydroalkylation of phenol is explored using Pd/C combined with H-BEA and La-exchanged BEA catalyst. An optimal ratio of metal to acid sites has been determined by detailed kinetic studies of the individual reaction steps including phenol hydrogenation as well as cyclohexanol dehydration and alkylation. The higher selectivity towards hydroalkylation achieved by La-BEA is explained by the supressed dehydration step in the cascade reactions.

The final chapter concludes the general findings from this thesis where we have shown that liquid hydrocarbon fuels can be obtained from biomass derived feedstocks over well-optimized bifunctional catalysts which balance the rates of multisteps in the cascade reactions by adjusting the concentrations of catalytically active acid and metal sites.

1.6. References

[1] J. W. Tester in *Sustainable energy,* MIT Press, **2005**.

[2] D. L. Klass in *Biomass for Renewable Energy, Fuels and Chemicals*, Academic Press, San Diego, **1998**.

[3] C. E. Wyman, S .R. Decker, M. E. Himmel, J. W. Brady, C. E. Skopec, L. Viikari, in *Polysaccharides, 2nd ed.* (Ed.: S. Dumitriu), Marcel Dekker, New York, **2005**.

[4] G. W. Huber, S. Iborra, A. Corma, *Chem. Rev.* **2006,** *106,* 4044.

[5] D. Carpenter, T. L. Westover, S. Czernik, W. Jablonski, *Green Chem.* **2014,***16,* 384.

[6] *Biomass Research and Development Technical Advisory Committee Roadmap for Biomass Technologies in the U.S.;* U. S. Government, 2002; http://www1.eere.energy.gov/biomass/publications.html.

[7] J. Zakzeski, P. C. A. Bruijnincx, A. L. Jongerius, B. M. Weckhuysen, *Chem. Rev.* **2010,** *110,* 3552.

[8] European Parliament and the Council, Directive 2009/28/EC, **2009**.

[9] K. T. Lee, C. Ofori-Boateng in *Sustainability of Biofuel Production from Oil Palm Biomass,* Springer, Singapore, **2013**.

[10] G. W. Huber, J. A. Dumesic, *Catal. Today* **2006,** *111,* 119.

[11] K. Bozbas, *Renewable Sustainable Energy Rev.* 2008, 12, 542.

[12] J. R. Regalbuto, *Science* **2009,** *325,* 822.

[13] J. C. Lopez-Linares, I. Romero, M. Moya, C. Cara, E. Ruiz, E. Castro, *Bioresour. Technol.* **2013,** *128,* 180.

[14] Y. Chisti, *Biotechnol. Adv.* 2007, 25, 294.

[15] T. M. Mata, A. A. Martins, N. S. Caetano, *Renewable Sustainable Energy Rev.* **2010,** *14,* 217.

[16] Y. Chisti, Biofuels **2010,** *1,* 233.

[17] H. Fukuda, A. Kondo, H. Noda, *J. Biosci. Bioeng.* **2001,** *92,* 405.

[18] L. C. Meher, D. Vidya Sagar, S. N. Naik, *Renew. Sustain. Energy. Rev.* **2006,** *10,* 248.

[19] R. Sharma, Y. Chisti, U. C. Banerjee, *Biotechnol. Adv.* **2001,** *19,* 627.

[20] P. Šimácek, D. Kubicka, G. Šebor, M. Pospíšil, *Fuel* **2009,** *88,* 456.

[21] M. Snåre, I. Kubičková, P. Mäki-Arvela, K. Eränen, D. Y. Murzin, *Ind. Eng. Chem. Res.* **2006,** *45,* 5708.

[22] G. W. Huber, P. O'Connor, A. Corma, *Appl. Catal. A* **2007,** *329,* 120.

[23] B. Peng, Y. Yao, C. Zhao, *Angew. Chem. Int. Ed.* **2012,** *51,* 2072.

[24] R. Nares, J. Ramírez, A. Gutiérrez–Alejandre, C. Louis, T. Klimova, *J. Phys. Chem. B* **2002,** *106,* 13287.

[25] J. S. Luterbacher, D. Martin Alonsoa, J. A. Dumesic, *Green Chem.* **2014,** *16,* 4816.

[26] M. J. Climent, A. Corma, S. Iborra, *Green Chem.* **2014,** *16,* 516.

[27] T. A. Hsu, M . R. Ladisch, G. T. Tsao, *Chem. Technol.* **1980,** *10,* 315.

[28] D. Klein-Marcuschamer, P. Oleskowicz-Popiel, B. A. Simmons, H. W. Blanch, *Biotechnol. Bioeng.* **2012,** *109,* 1083.

[29] J. P. Diebold, J. P. *A Review of the Chemical and Physical Mechanisms of the Storage Stability of Fast Pyrolysis Bio-Oils,* Report No. NREL/SR-570-27613, National Renewable Energy Laboratory, Golden, CO, **2000**; http://www.osti.gov/bridge.

[30] T. A. Milne, F. Agblevor, M. Davis, S. Deutch, D. Johnson, in *Developments in Thermal Biomass Conversion* (Eds.: A. V. Bridgwater, D. G. B. Boocock), Blackie Academic and Professional, London, **1997**.

[31] R. J. Evans, T. A. Milne, *Energy Fuels* **1987,** *1,* 123.

[32] S. Czernik, A. V. Bridgwater, *Energy Fuels* **2004,** *18,* 590.

[33] E. Laurent, B. Delmon, *J. Catal.* **1994,** *146,* 281.

[34] C. Zhao, Y. Kou, A. A. Lemonidou, X. Li, J. A. Lercher, *Angew. Chem. Int. Ed.* **2009,** *48,* 3987.

[35] C. Zhao, Y. Kou, A. A. Lemonidou, X. Li, J. A. Lercher, *Chem. Commun.* **2010,** *46,* 412.

[36] C. Zhao, J. He, A. A. Lemonidou, X. Li, J. A. Lercher, *J. Catal.* **2011,** *280,* 8.

[37] C. Zhao, J.A. Lercher, *ChemCatChem* **2012,** *4,* 64.

[38] C. Zhao, J. A. Lercher, *Angew. Chem. Int. Ed.* **2012,** *51,* 5935.

[39] C. Zhao, S. Kasakov, J. He, J. A. Lercher, *J. Catal.* **2012,** *296,* 12.

[40] C. Zhao, Y. Yu, A. Jentys, J. A. Lercher, *Appl. Catal. B* **2013,** *132,* 282.

[41] C. Zhao, D. Camaioni, J. A. Lercher, *J. Catal.* **2012,** *288,* 92.

[42] F. M. A. Geilen, B. Engendahl, A. Harwardt, W. Marquardt, J. Klankermayer, W. Leitner, *Angew. Chem., Int. Ed.* **2010,** *49,* 5510.

[43] P. N. R. Vennestroem, C. H. Christensen, S. Pedersen, S. J. D. Grunwaldt, J. M. Woodley, *ChemSusChem* **2010,** *2,* 249.

[44] M. Chia, Y. J. Pagan-Torres, D. Hibbitts, Q. H. Tan, H. N. Pham, A. K. Datye, M. Neurock, R. J. Davis, J. A. Dumesic, *J. Am. Chem. Soc.* **2011,** *133,* 12675.

[45] R. Alamillo, M. Tucker, M. Chia, Y. Pagan-Torres, J. A. Dumesic, *Green Chem.* **2012,** *14,* 1413.

[46] M. Sankar, N. Dimitratos, P. J. Miedzia, P. P. Wells, C. J. Kiely, G. J. Hutchings, *Chem. Soc. Rev.* **2012,** *41,* 8099.

[47] D. M. Alonso, S. G. Wettstein, J. A. Dumesic, *Chem. Soc. Rev.* **2012,** *41,* 8075.

[48] M. Besson, P. Gallezot, *Catal. Today* **2003,** *81,* 547.

[49] W. Song, Y. Liu, E. Barath, C. Zhao, J. A. Lercher, *Green Chem.* **2015,** *17,* 1204.

[50] B. Peng, X. Yuan, C. Zhao, J. A. Lercher, *J. Am. Chem. Soc.* **2012,** *134,* 9400.

[51] B. L. Cushing, V. L. Kolesnichenko, C. J. O'Connor, *Chem. Rev.* **2004,** *104,* 3893.

[52] R.P. Townsend, E.N. Cocker, *Stud. Surf. Sci. Catal.* **2001**, *137,* 467.

[53] A. Corma, H. Garcá, A. Leyva, *J. Catal.* **2004,** *225,* 350.

[54] J. W. Geus, Dutch Pat. Appl. 6705,259, 1967; 6813,236, 1968.

[55] L. A. M. Hermans, J. W. Geus, in *Preparation of Catalysts II* (Eds.: B. Delmon, P. Grange, P. A. Jacobs, G. Poncelet), Elsevier, Amsterdam, **1979,** p 113.

[56] B. Delmon, *J. Mol. Catal.* **1990,** *59,* 179.

[57] A. Gil, A. Diaz, L. M. Gandia, M. Montes, *Appl. Catal. A* **1994,***109,* 167.

[58] P. Burattin, M. Che, C. Louis, *J. Phys. Chem. B* **1997,** *101,* 7060.

[59] M. Han, Q. Liu, J. He, Y. Song, Z. Xu, J. Zhu, *J. Adv. Mater.* **2007,** *19,* 1096.

[60] H. Bönnemann, W. Brijoux, R. Brinkmann, T. Joussen, *Angew. Chem. Int. Ed.* **1990,** *29,* 273.

[62] Ö. Metin, V. Mazumder, S. Özkar, S. Sun, *J. Am. Chem. Soc.* **2010,** *132,* 146.

Chapter 2

Importance of Size and Distribution of Ni Nanoparticles for the Hydrodeoxygenation of Microalgae Oil

Improved synthetic approaches for preparing small-sized Ni nanoparticles (d=3 nm) supported on HBEA zeolite have been explored and compared with the traditional impregnation method. The formation of surface nickel silicate/aluminate involved in the two precipitation processes are inferred to lead to the stronger interaction between the metal and the support. The lower Brønsted acid concentrations of these two Ni/HBEA catalysts compared with the parent zeolite caused by the partial exchange of Brønsted acid sites by Ni^{2+} cations do not influence the hydrodeoxygenation rates, but alter the product selectivity. Higher initial rates and higher stability have been achieved with these optimized catalysts for the hydrodeoxygenation of stearic acid and microalgae oil. Small metal particles facilitate high initial catalytic activity in the fresh sample and size uniformity ensures high catalyst stability.

2.1. Introduction

Selective conversion of biomass resources such as polysaccharides[1,2], lignin[3,4], bio-ethanol, and glycerol[5-11] requires highly efficient catalysts. Within this biomass feedstock, glycerol is a very attractive option due to its relatively low cost and wide availability as a by-product of bio-diesel production. It is considered to be, therefore, one of the top 12 building block chemicals of a biorefinery process.[12]

Developing alternative energy sources has become a key factor to ensure the sustainable growth through minimizing the carbon footprint. In this context, microalgae have been envisioned as one of the promising biomass resources because of their rapid growth rate[1] and high lipid content.[2] Cultivation of microalgae is also considered to be socially and environmentally benign, as it does not directly compete with agricultural products or freshwater supply.[3] In a recent contribution, Ni nanoparticles supported onto or/and into HBEA zeolites or ZrO_2 have been reported as sulfur-free catalysts, which are able to realize quantitative transformation of crude microalgae oil into diesel-range alkanes as high-grade second-generation biofuels under mild conditions (533 K, 40 bar H_2).[4]

Incorporation of nickel into zeolite framework enables the preparation of dual-functional catalysts that combine the hydrogenation–dehydrogenation abilities of a metal and the carbocation rearrangement functions of solid Brønsted acids. Nickel catalyzes the first hydrogenation reaction (rate-determining step), whereas the zeolite Brønsted acid sites catalyze water elimination.[5] However, the Ni/zeolite bifunctional catalyst prepared by conventional incipient wetness impregnation method as reported[4] suffers from large and non-uniform Ni particles, leading to relatively low Ni dispersion and resultantly low hydrogenation activity.[6] In addition to impregnation, supported Ni catalysts are usually prepared by ion-exchange and sol–gel techniques, both of which have limitations. For instance, the sol–gel method can generate homogeneously dispersed Ni particles at higher metal content, but the resulting particle size increases with the increasing Ni content (typically larger than 10 nm, when the Ni content exceeds 10 wt%).[7] However, the ion-exchange approach can achieve high metal dispersion, but the attainable Ni loading is rather low and is limited by the exchange capacity of the zeolite.

The deposition–precipitation (DP) method developed by Geus et al.[8] has been considered as a promising approach to prepare the Ni/SiO$_2$ catalyst with high metal dispersion at relatively high loading, and effort was also made to rationalize the feasibility of extending the DP method to zeolite support.[9] DP consists of precipitating a Ni(II) phase by basification of a suspension containing nickel salt solution and the support. Urea (CO(NH$_2$)$_2$) is used as the precipitation/basification agent. It begins to hydrolyze at elevated temperature (363 K), so that hydroxide (OH$^-$) ions are generated gradually and homogeneously to avoid local supersaturation and the sole precipitation of Ni hydroxide in solution.

Attempts are also made to realize a two-step synthesis, in which monodispersed Ni nanoparticles (NPs) are prepared separately, followed by grafting of the as-synthesized Ni NPs onto/into the support by mechanical mixing. Solution-phase synthesis of Ni NPs normally involves reduction of Ni(II) metal precursors either in the presence of amine and/or carboxylic acid,[10] or by a strong reducing agent such as boro-hydride derivatives.[11] The former synthesis involves complex mechanisms including intermediate formation and acid–base equilibria, which makes tailored synthesis hardly achievable. In the latter case of chemical reduction, nucleation is usually too rapid to control.[12] The other challenge with respect to solution-phase synthesis of Ni NPs lies in the selection of appropriate protecting ligands (i.e., surfactants) that stabilize the NPs,[13] because robust protecting agents binding strongly to Ni^0 usually show detrimental effects to the catalytic activities. The efforts to remove surfactants usually require high temperatures, which inevitably lead to the aggregation of NPs. It is recently reported that monodispersed Ni NPs, synthesized by reducing Ni(II) acetylacetonate with a borane tributylamine complex in the presence of oleylamine and oleic acid acting as solvent and surfactant, showed high activities on hydrolytic dehydrogenation of the ammonia borane complex even without the necessity to remove the surfactants.[14]

In general, the processes for synthesizing Ni/HBEA catalysts by using four preparation routes including impregnation, ion exchange/precipitation, deposition/precipitation, and Ni NPs methods are summarized in Scheme 2-1. We explore and compare the catalytic properties and performances of these four Ni/HBEA catalysts, with the goal to obtain small and homogeneously dispersed Ni particles, in

order to realize high activity and stability with respect to the catalytic hydrodeoxygenation of stearic acid and crude microalgae oil.
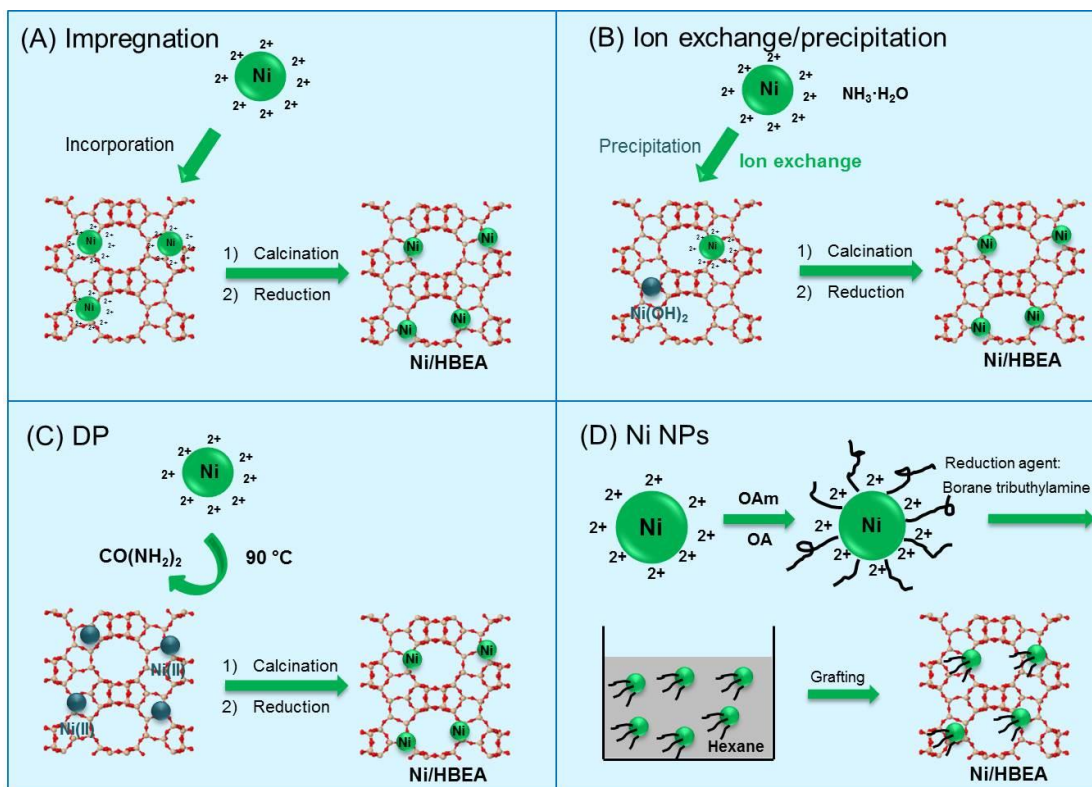
Scheme 2-1. The processes for forming supported Ni nanoparticles onto/into HBEA with four routines.

2.2. Experimental section

2.2.1. Chemicals

All chemicals were obtained from commercial suppliers and used as received. Stearic acid (Fluka, analytical standard), dodecane (Sigma–Aldrich, $\geq 99\%$, Reagent Plus), Ni(II) nitrate hexahydrate (Sigma–Aldrich, $\geq 98.5\%$), Ni(II) acetylacetonate (Aldrich, 95%), ammonium hydroxide solution (Sigma–Aldrich, 28.0–30.0% NH_3 basis, ACS reagent), urea (Sigma–Aldrich, BioReagent), oleylamine (Aldrich, 70%, technical grade), oleic

acid (Fluka, Ph Eur), borane triethylamine complex (Aldrich, 97%), *n*-hexane (Sigma–Aldrich, $\geq 97\%$), ethanol (Roth, $\geq 99.5\%$), HBEA (Clariant, Si/Al=75).

2.2.2. Catalyst preparation

Preparation of Ni/HBEA by incipient wetness impregnation

In a typical synthesis, $Ni(NO_3)_2 \cdot 6H_2O$ (2.91 g) was dissolved in doubly distilled water (10 g), and then the solution was slowly dropped onto HBEA zeolite (10 g) with continuous stirring at ambient temperature for a total of 4 h. After completing this procedure, the material was firstly dried overnight at ambient temperature and then further at 383 K for 12 h. Afterwards, the catalyst precursor was calcined in air (flow rate: 100 ml min^{-1}) at 673 K for 4 h and reduced with pure hydrogen (flow rate: 150 ml min^{-1}) at 733 K for 5 h with a temperature increment of 1 K min^{-1}.

Preparation of Ni/HBEA by ion exchange

For a standard ion-exchange procedure, the parent HBEA zeolite (5 g) was suspended in an aqueous solution of $Ni(NO_3)_2$ (0.14 M, 250 mL). The suspension was stirred for 6 h at 343 K. Later, the solid was separated by filtration, and the resulting materials were washed three times with doubly distilled water and ovendried at 383 K overnight. Subsequently, the catalysts precursors were calcined at 673 K for 4 h with a heating rate of 1 K min^{-1}. The exchange procedures were repeated three times. Finally, the calcined catalyst was reduced at 733 K for 5 h with a heating rate of 1 K min^{-1} and a hydrogen flow of 150 ml min^{-1}.

Preparation of Ni/HBEA by ion exchange/precipitation with ammonia solution

Firstly, HBEA zeolite (5 g) was suspended in aqueous solution of $Ni(NO_3)_2$ (0.14 M, 250 mL), and a solution of ammonia was added dropwise until the pH value of the suspension reached 7.5, and the suspension was then kept under constant stirring at room temperature for 90 min. Afterwards, the solid was filtered out and washed three times with doubly distilled water. The samples were dried at 383 K overnight and calcined at

673 K for 4 h with a heating rate of 1 K min^{-1}. The calcined catalyst was reduced at 733 K for 5 h with a heating rate of 1 K min^{-1} and a hydrogen flow of 150 ml min^{-1}.

Preparation of Ni/HBEA by deposition–precipitation (DP) method

The typical synthesis adopted procedures described in literature.[6] An aqueous solution of Ni(NO$_3$)$_2$ (0.14 M, 250 mL) was prepared, and 210 mL of which was used to make a suspension with 2 g of the parent HBEA zeolite. Urea was dissolved in the rest of Ni(NO$_3$)$_2$ solution (40 mL), and added drop-wise into the zeolite suspension when the latter was heated to 343 K. The mixture was then brought up to 363 K at which DP started. After 1 h, the suspension was cooled to room temperature, vacuum filtered, and the solid was washed three times with doubly distilled water. Subsequently, the samples were dried at 383 K overnight. The catalyst precursors were calcined at 673 K for 4 h with a heating rate of 1 K min^{-1}, and then reduced at 733 K for 5 h with a heating rate of 1 K min^{-1} and a hydrogen flow of 150 ml min^{-1}.

Preparation of Ni/HBEA by grafting as-synthesized Ni nanoparticles (NPs)

The Ni NPs were synthesized by using the following procedure developed by Metin et al.[14] Firstly, Ni(acac)$_2$ (1.03 g, 4 mmol) was mixed with oleylamine (OAm; 60 mL) and oleic acid (OA; 1.27 mL, 4 mmol). The mixture was heated up to 383 K under the protection of nitrogen and maintained for 1 h to remove air and moisture. Subsequently, it was cooled down to 363 K and then borane triethylamine (BTE, 1.2 mL, 8 mmol) was quickly injected. The formation of Ni^0 NPs was observed through a visible color change from green to brownish-black. The resultant solution was kept at 363 K for another 1 h before cooling down to room temperature. Afterwards, ethanol (120 mL) was added into the suspension, and the Ni NPs were separated by centrifugation and then re-dispersed in *n*-hexane (80 mL) by means of ultrasonication. To graft the as-synthesized Ni NPs, the parent HBEA zeolite (2.5 g) was carefully added into the obtained NP colloid, and the mixture was stirred overnight. Before applying the catalyst to reaction, *n*-hexane was vacuum filtered and Ni/HBEA was dried at 343 K and reduced by H$_2$ at 733 K for 5 h with a heating rate of 1 K min^{-1} and a hydrogen flow of 150 ml min^{-1}.

2.2.3. Catalyst characterization

Elemental analysis was measured by atomic absorption spectroscopy (AAS) on a UNICAM 939 AA-Spectrometer. The BET specific surface area and pore volume were determined by nitrogen adsorption-desorption isotherms measured at 77 K by using a PMI automatic BET-Sorptometer. The sample was activated in vacuum at 473 K for 2 h before measurement.

Transmission electron microscopy (TEM) images were taken by a JEM-2010 Jeol transmission microscope operating at 120 kV. The sample was firstly made suspension in ethanol by ultrasonication, and a drop of such suspension was deposited onto a carbon-coated Cu grid. More than 300 particles were counted for the histograms of particle size distribution.

The temperature-programmed reduction (TPR) measurement was performed on a self-constructed instrument, by using a stream of 3% H_2/He mixture and a heating rate of 5 K min^{-1}. The H_2O formation during the TPR experiments was monitored by mass spectrometry.

Temperature-programmed desorption (TPD) of NH_3 was performed in a 6-fold parallel reactor system. The catalysts were activated in He at 773 K with a heating rate of 5 K min^{-1} for 1 h. NH_3 was adsorbed with a partial pressure of 1 mbar at 373 K. Afterwards, the samples were purged with He (30 ml min^{-1}) for 2 h to remove physisorbed molecules. For the temperature-programmed desorption measurement, the samples were heated in flowing He from 373 to 1033 K with an increment of 10 K min^{-1} to desorb ammonia. The desorbed species were monitored by mass spectrometry (Balzers QME 200). For the quantification of acid sites presented in the samples, a reference (HZSM-5, Si/Al=45 from Clariant) with known acidity was used to calibrate the signal.

The Infrared (IR) spectra of adsorbed pyridine were recorded with a Perkin–Elmer 2000 spectrometer at a resolution of 4 cm^{-1}. The catalyst sample was prepared as self-supporting wafer and activated in vacuum (P=10^{-7} mbar) at 723 K for 1 h (heating rate=10 K min^{-1}). After cooing to 423 K, the sample was equilibrated with 0.1 mbar of pyridine for 30 min followed by evacuating the system for 1 h, a spectrum was recorded thereafter. For quantification, molar integral extinction coefficients of 0.73 and 0.96

cm µmol^{-1} were used for Brønsted and Lewis acid sites, respectively. These were determined from a standard (HZSM-5, Si/Al=45 from Clariant).

The IR spectra of adsorbed CO were recorded on a Bruker VERTEX 70 spectrometer at a resolution of 4 cm^{-1} with 128 scans. The catalyst wafer was firstly in-situ-reduced in hydrogen (1 bar) at 723 K for 1 h (heating rate=10 K min^{-1}), and then allowed outgassing for 1 h (P=10^{-6} mbar). CO was adsorbed at 313 K, and a spectrum was taken at 0.5 mbar of CO equilibrium pressure. Afterwards, the system was evacuated to remove physically adsorbed CO, and the IR spectra were recorded every five minutes until no changes observed. To directly compare the surface coverage of adsorbed CO, all spectra were normalized with the weight of the respective wafers.

2.2.4. Catalytic measurements

Catalytic reactions on stearic acid and microalgae oil: A typical experiment was carried out as follows: Stearic acid (or microalgae oil) (1.0 g), dodecane (100 mL), and Ni/HBEA catalyst (0.2 g) were charged into a batch autoclave (Parr Instrument, 300 mL). The reactor was firstly flushed with N_2 at ambient temperature, and then heated up to 533 K when 40 bar of H_2 was purged, and the reaction started at a stirring speed of 700 rpm. The liquid products were sampled in situ during the catalytic runs, and analyzed by a Shimadzu GC-MS equipped with a FID detector and a HP-5 capillary column. For the conversion of microalgae oil, docosane was used as an internal standard for quantification of liquid products. Conversion = (weight of converted reactant/weight of the starting reactant) $\times$ 100%. Yield of liquid products (C%) = (C atoms in liquid products/C atoms in the starting reactant) $\times$ 100%. Selectivity (C%) = (C atoms of each product/C atoms in all the liquid products) $\times$ 100%.

2.3. Results and discussion

2.3.1. Comparison of four synthesis methods for Ni/HBEA catalysts

In the present work, four synthetic methods were selected to prepare Ni/HBEA catalysts. The first traditional incipient impregnation method incorporated Ni(II) nitrate hexahydrate aqueous solution with HBEA and reached 5.2 wt.% Ni content in Ni/HBEA (see Table 2-1). Ion exchange with Ni(II) nitrate hexahydrate solution was performed on HBEA zeolite in aqueous suspension three times successively, and the resulting Ni content, determined by atomic absorption spectroscopy (AAS), was only 0.6 wt.%, which was tested to be insufficient to catalyze hydrodeoxygenation (HDO) of C_{18} fatty acid. With the aim to increase the Ni content to around 5 wt.%, an ammonia solution was added to adjust the pH value of the suspension. Consequently, precipitated Ni(II) hydroxide phases as well as ion-exchanged Ni^{2+} existed simultaneously in the resultant catalyst precursor, annotated herein as "ion exchange/precipitation". In the DP synthesis, Ni contents in the final product increased almost linearly from 5 to 15 wt.% with DP durations from 1 to 3 h in a highly reproducible manner (Figure 2A-1, the Appendix). The evolution of the pH value during the first hour of DP is shown in Figure 2A-2 (the Appendix). An increase in the pH (initial: 3.5) was firstly observed due to the fast generation of OH$^-$ ions by urea hydrolysis at 363 K. Then, the pH of mixture reached a maximum at 5.6 and stabilized at a slightly lower value of 5.5 due to the dynamic equilibrium between the formation of OH$^-$ ions and their consumption for precipitation of Ni(II) hydrooxoaqua species on the surface of HBEA (Figure 2A-2, the Appendix). The Ni loadings at different DP duration and the shape of the pH variation curve are similar to the DP cases with Ni(II) on both silica and HBEA zeolite,[6, 9] demonstrating that DP is a controllable and reproducible method for synthesizing Ni/HBEA catalysts. In the fourth case, the synthetic strategy with Ni NPs involved firstly the preparation of soluble Ni NPs by reducing Ni(acac)$_2$ (acac=acetylacetonate) with borane tributylamine (BTB) in the presence of oleylamine (OAm) and oleic acid at 363 K, followed by grafting the as-synthesized NPs onto the zeolite under stirring at ambient temperature in hexane.

Table 2-1. Physicochemical properties of parent HBEA and Ni/HBEA prepared by different methods.

Method	Ni loading (wt.%)	BET surface area ($m^2\,g^{-1}$)	Pore volume ($cm^3\,g^{-1}$)		
			Micro	Meso	Total
Parent HBEA	–	615	0.20	0.17	0.37
Impregnation	5.2	603	0.19	0.19	0.38
Ion Exchange/ Precipitation	5.1	562	0.17	0.23	0.40
DP	5.9	508	0.14	0.24	0.38
Ni NPs	5.8	596	0.19	0.18	0.37

2.3.2. Physicochemical properties

All Ni/HBEA samples had similar Ni contents of approximately 5 wt.% (see Table 2-1). The nitrogen adsorption–desorption isotherms were nearly identical for parent HBEA and Ni/HBEA materials prepared by impregnation and Ni NPs methods (see Table 2-1), indicating minimal impact of Ni introduction on the surface property (Brunauer–Emmett–Teller (BET) surface area: 500–600 $m^2\,g^{-1}$) and pore structure (pore volume: 0.37–0.40 $cm^3\,g^{-1}$) of the zeolite by these two methods. For samples prepared by ion exchange/precipitation and DP, the remarkable decrease in micropore volumes by 0.03 and 0.06 $cm^3\,g^{-1}$ infers that Ni nanoparticles are partially located in the micropores of HBEA.

The nature of the different preparation methods has led to the different morphologies of Ni nanoparticles presented in the reduced Ni/HBEA samples (see Figure 2-1). Ni/HBEA prepared by impregnation showed much larger Ni particles with average diameters of 25 nm compared with sizes of 2–4 nm obtained from the other three methods. The DP method resulted in the smallest Ni particles (2.5 nm) with the most uniform size distribution (standard deviation: 0.7 nm), whereas ion exchange/precipitation led to similar Ni particle size but in a wider range of size distribution with 1.4 nm deviation. This difference is attributed to a sudden increase of local pH value upon the addition of ammonia in the method of ion exchange/precipitation,

which caused unevenly precipitated Ni(II) species. In contrast, in the case of DP, hydroxide ions are slowly and homogeneously generated through hydrolysis of urea at elevated temperature, leading to more evenly dispersed Ni particles. In the solution-phase synthetic routine, grafting Ni NPs onto HBEA also produced uniform Ni particles with a derivation of 1.0 nm at an average size of 3.9 nm.
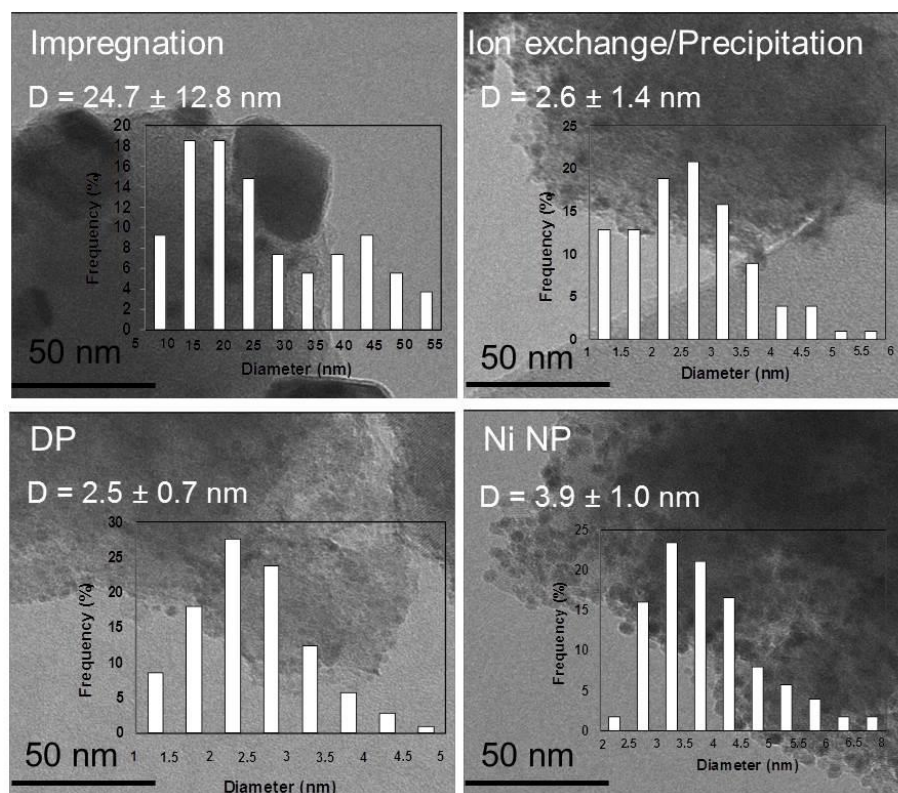

Figure 2-1. TEM images of reduced Ni/HBEA samples prepared by different methods; the respective insets are the histograms of Ni particle size distribution (after counting 300 particles).

To further investigate the underlying differences on metal-support interaction, temperature-programmed reduction (TPR) was performed on the calcined catalyst precursors prepared by the three incorporation methods, and the sample prepared by the Ni NPs method (see Figure 2-2). For the impregnated sample, the most prominent reduction peak occurred at 635 K, which is characteristic for the reduction temperature of a supported "NiO"-like phase,[15,16] suggesting that NiO clusters have a weak interaction with the zeolite support after impregnation.[17]
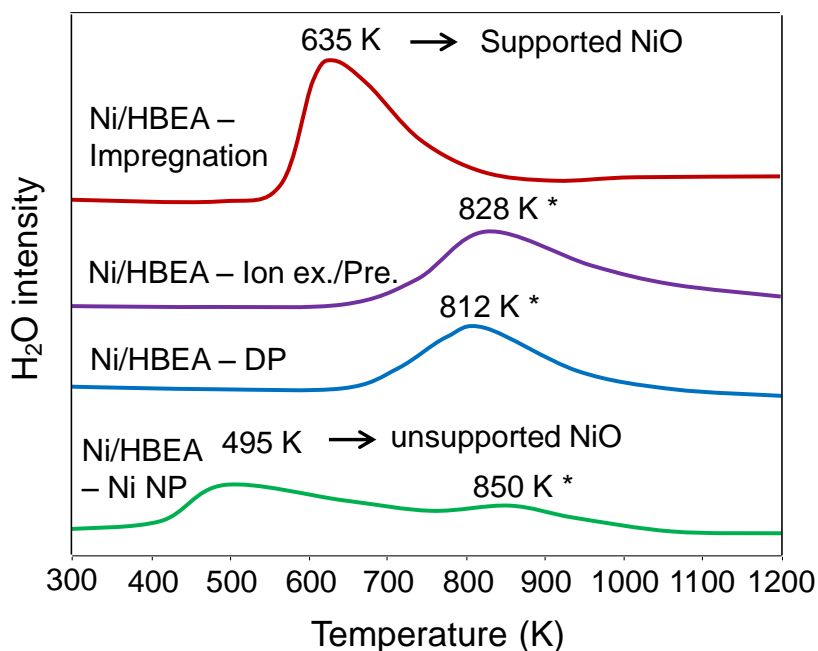
Figure 2-2. TPR profiles of calcined Ni/HBEA precursors prepared by the first three methods, and the as-synthesized catalyst sample prepared by using the Ni NP method. * =Layered structure at Ni-support interface consisting of nickel silicate/nickel aluminate species.

The TPR profiles of catalyst precursors prepared by ion exchange/precipitation and DP both showed broad peaks with maxima at 828 and 812 K, respectively. These peaks can be assigned to the reduction of surface Ni silicate in agreement with literature,[9,15] or Ni aluminate species, depending on the position of hydroxyl groups of the HBEA surface that react with the Ni(II) hydrooxoaqua complex during the synthesis. Burratin et al.[9] confirmed the existence of Ni silicate in the calcined Ni/SiO$_2$ sample prepared by DP method, whereas in our case with the altered support of HBEA, Ni-silicate and Ni-aluminate are both likely to be formed due to the coexistence of surface Si–OH and Al–OH groups. The presence of either one or two Ni species appears to strengthen the interaction of Ni with HBEA support.

The catalyst precursor prepared by the Ni–NP method produced two asymmetric peaks with maxima at 495 and 850 K, respectively (Figure 2-2). Although metallic Ni nanoparticles were readily synthesized, these neo-formed 4 nm Ni^0 clusters were inevitably oxidized upon exposure to the atmospheric environment.[11b,18] The first peak in TPR profiles at 495 K is attributed to the reduction of oxidized Ni nanoparticles by air

in the atmospheric environment. This "re-oxidized" NiO phase (reduced at 495 K) differs from the bulk NiO (reduced at 635 K)[19] in nature, leading to the lower reduction temperature. The other insignificant peak appeared at 850 K, which is close to the reduction temperature of Ni silicate/aluminate. Such a peak indicates that an interaction between metallic Ni nanoparticles and HBEA exists, probably due to the oxidation of NPs by the oxygen and/or water in the pores of zeolite. In general, the enhanced metal-support interaction is manifested by the surface Ni-silicate/aluminate species presented in the latter three catalyst precursors. It is speculated that the stronger interaction is important in preventing sintering of Ni during reduction.

To investigate the influence of reduction temperature on the catalyst activity, Ni/HBEA catalysts prepared by the DP method were reduced at 733, 833, 933 K respectively, and tested in the hydrodeoxygenation of stearic acid (see Figure 2A-3a, the Appendix). The results showed that catalyst precursors reduced at 733 K had the highest catalytic activity. Although higher temperatures would be beneficial for the complete reduction of Ni species, it also leads to Ni sintering, which was visible in the TEM images (see Figure 2A-3b, the Appendix). Thus, 733 K was chosen as the reduction temperature for Ni samples prepared by the four methods in this study.

The state of Ni species as well as the dispersion of supported metallic Ni NPs was also explored by IR spectroscopy using CO as a probe molecule (Figure 2-3). In the spectra with adsorbed CO under equilibrium pressure, bands above $2100 \, cm^{-1}$ were detected, which are typical for carbonyls formed with Ni cations.[20–23] The reduction temperature at 733 K was lower than the maxima of reduction in the TPR profiles for the latter three samples (Figure 2-2). This led to the presence of cationic Ni. The bands at $2210–2212 \, cm^{-1}$ are assigned to $Ni^{2+}–CO$,[24–27] whereas the two bands at 2136–2137 and $2092–2094 \, cm^{-1}$ are ascribed to the symmetric and asymmetric CO stretching of geminal $Ni^+(CO)_2$ dicarbonyls.[21,22, 28,29] The Ni^+ ion is speculated to originate from the reduction of Ni^{2+} in the reducing environment of CO.[30] The fact that two CO molecules are attached to one Ni^+ cation compared with $Ni^{2+}–CO$ can be rationalized by the higher ionic radius of Ni^+.[25] Both $Ni^{2+}–CO$ and $Ni^+(CO)_2$ were unstable and readily decomposed upon evacuation (solid black lines in Figure 2-3). Moreover, disappearance of the bands representing $Ni^+(CO)_2$ geminal dicarbonyls was accompanied by the

emergence of a new band at around 2100 cm^{-1} in the spectra after outgassing. This band is characteristic for the stable linear Ni^+ monocarbonyl.[21–23,25,27] Such a species is resistant against evacuation and more stable than Ni^{2+}–CO. Its higher stability is attributed to the π backbonding between Ni^+ and CO as well as to the synergistic effect between the π and σ bonds.[25] The carbonyls formed with ionic Ni species were also observed on Ni/HBEA prepared by impregnation, since a small proportion of Ni silicate is also possibly formed.[31]
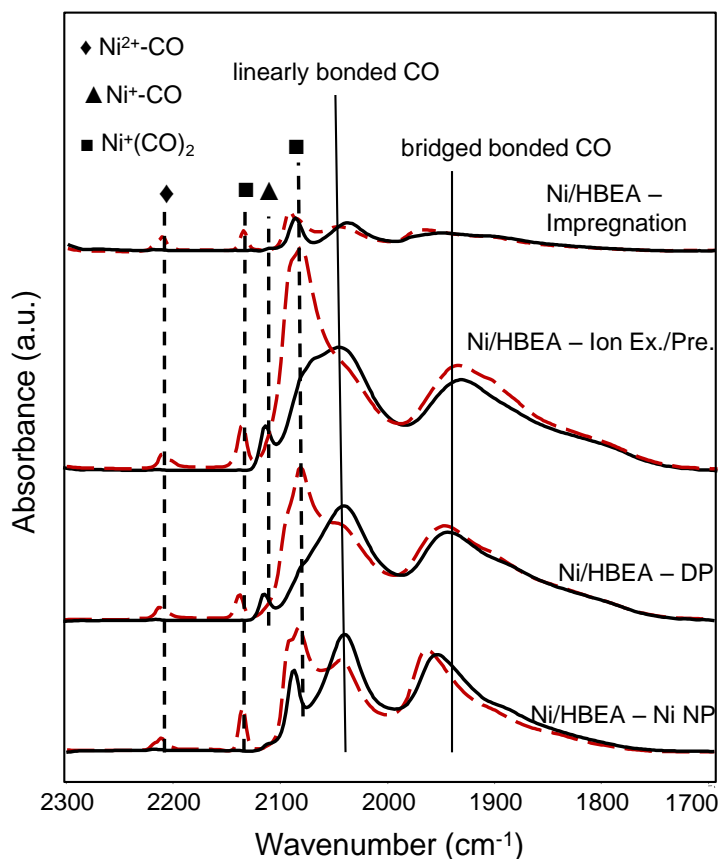
Figure 2-3. IR spectra of adsorbed CO at 313 K recorded at 0.5 mbar CO partial pressure (red dashed lines), and after outgassing for 15 min (black solid lines). All spectra have been normalized by the weights of the catalyst pellets.

The other two pronounced bands in the IR spectra after evacuation appeared at 2040–2045 cm^{-1} (linearly bonded CO adsorption on metallic Ni^0) and 1910–1970 cm^{-1} (two or three-fold bridged CO adsorption on Ni0).[19–21, 24, 27, 32] Ni/HBEA prepared by ion

exchange/precipitation, DP, and Ni NP methods showed much higher integral intensities under these two bands representing linearly and bridged-bonded CO, indicating higher concentrations of accessible metallic Ni species present in these samples. This observation also indicates that much smaller Ni nanoparticles with higher metal dispersions are achieved by the optimized synthetic methods (see Table 2-1).
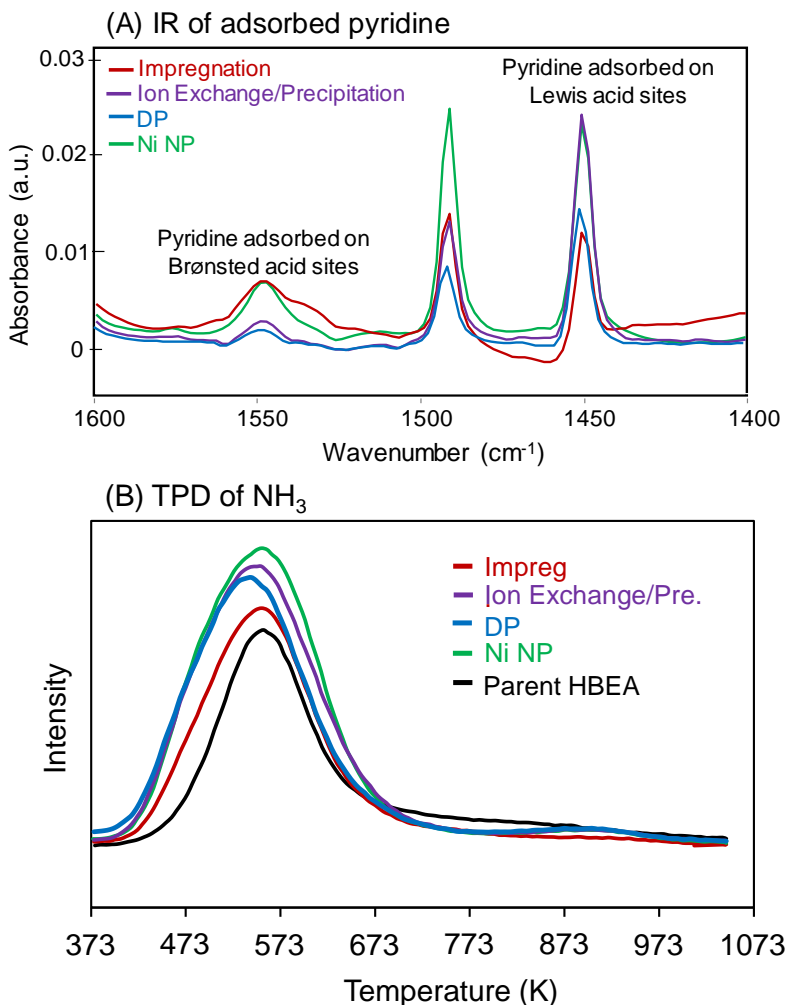

Figure 2-4. A) IR spectra of adsorbed pyridine. B) Profiles of temperature programmed-desorption of NH3.

The acidities of four Ni/HBEA samples were probed by IR spectroscopy of adsorbed pyridine (pyridine-IR) and temperature-programmed-desorption of NH_3 (TPD-NH_3). Compared with parent HBEA (119 mmolg^{-1}), Ni/HBEA catalysts prepared by DP and

ion-exchange methods possessed lower concentrations of Brønsted acid sites of 36 mmolg^{-1} (Figure 2-4A), possibly due to the heterocondensation between acidic hydroxyl groups and Ni(II) hydrooxoaqua complexes during these two syntheses. In addition, increased concentrations of Lewis acid sites were also observed with Ni/HBEA compared with the parent HBEA (see Table 2A-2, the Appendix). These Ni-based samples had unreduced ionic Ni species as evidenced by the IR spectra of adsorbed CO (see Figure 2-3) and TPR-H$_2$ (see Figure 2-2), which are speculated to be potential Lewis acid sites,[34] causing the increase in the Lewis acid concentration. Evolution of total acidity for the four catalysts measured by both NH$_3$-TPD and pyridine-IR techniques showed a similar trend (see Table 2A-2, the Appendix).

2.3.3. Activity and stability for stearic acid hydrodeoxygenation
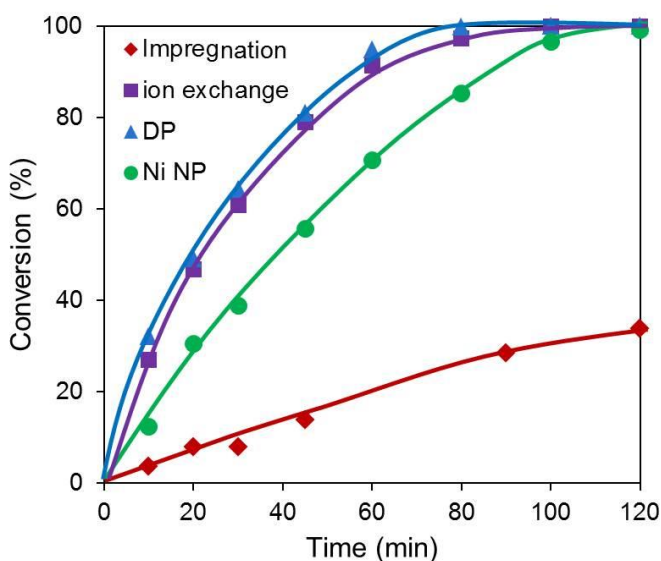
Figure 2-5. Hydrodeoxygenation (HDO) of stearic acid as a function of time over Ni/HBEA prepared by four different methods. Reaction conditions: stearic acid (1.0 g), catalyst (0.2 g), dodecane (100 mL), 40 bar H$_2$ (at reaction temperature 533 K), at a stirring speed of 700 rpm.

The catalytic activities were tested for hydrodeoxygenation of stearic acid at 533 K at 40 bar H$_2$. The catalyst prepared by DP with the smallest Ni particles had the highest hydrodeoxygenation activity with an initial rate of 18 mmol g^{-1} h^{-1}, whereas the

traditional impregnation method resulted in the slowest initial rate of 3.5 mmol g^{-1} h^{-1} (Figure 2-5 and Table 2-2). The initial rates of 17 and 14 mmol g^{-1} h^{-1} were obtained over the other two Ni/ HBEA catalysts prepared by ion-exchange/precipitation and Ni NP approaches (see Table 2-2). When normalized to the amount of the surface Ni atoms, turnover frequencies (TOFs) for the hydrogenation of stearic acid were 125, 243, 178, and 140 mol $mol_{Surf\ Ni\ atom}^{-1}$ h^{-1} over the four Ni/HBEA samples, indicating that hydrogenation of stearic acid is insensitive to the structure of Ni nanoparticles. The yields of cracking products were below 5% (among products in the liquid phase) after 2 h. Analysis of the product distribution in the liquid phase (Table 2-2 and Figure 2-6) showed that a relatively higher selectivity towards heptadecane (C_{17}) and lower selectivity to isooctadecane (C_{18}) was observed for Ni/HBEA catalysts synthesized by the later three methods as compared with those catalyzed by the impregnated sample.

Table 2-2. Hydrodeoxygenation of stearic acid over Ni/HBEA by four methods.[a]

Method	Conv. (%)	Initial rate [b]	TOF [c]	Yield of liquid products (C%)				
				n-C_{18}	*Iso*-C_{18}	n-C_{17}	C_{18}-OH	Cracking
Impreg.	33	3.5	125	16	3.4	9.2	0.21	4.1
Ion Ex./Pre.	97	17	243	61	2.5	33	0.01	3.5
DP	100	18	178	61	2.1	34	–	3.3
Ni NP	100	14	140	61	2.3	32	0.1	3.8

[a] The reaction conditions are identical to that in Figure 2-5, reaction time: 2 h. [b] Unit: mmol g^{-1} h^{-1}. [c] Unit: mol·$mol_{Surf.\ Ni\ atom}^{-1}$ h^{-1}, Ni dispersions are 3.3%, 8.2%, 9.9%, 9.8% for Ni/HBEA catalysts synthesized by impregnation, ion exchange/precipitation, DP, and Ni NP methods, respectively, as determined by H_2 chemisorption measurement.

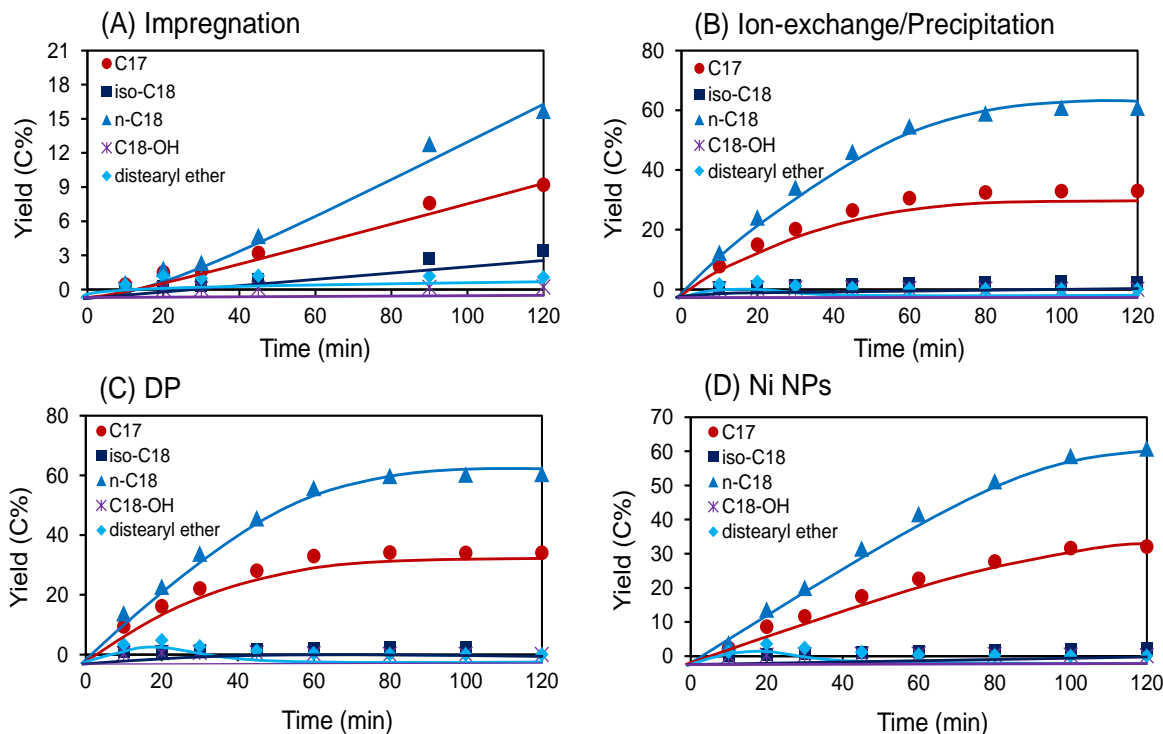**Figure 2-6.** Product distributions on stearic acid conversion over Ni/HBEA prepared by four different methods. Reaction conditions: stearic acid (1.0 g), catalyst (0.2 g), dodecane (100 mL), 40 bar H_2 (at reaction temperature 533 K), at a stirring speed of 700 rpm.

We have explored the mechanism of stearic acid hydrodeoxygenation with Ni/HBEA in the previous work.[4a] It showed that stearic acid is firstly hydrogenated to octadecanal on Ni sites and then converted to 1-octadecanol through a dehydrogenation–hydrogenation equilibrium (favored at high hydrogen pressure). Parallel routes of decarbonylation with Ni sites and dehydration on acidic sites can take place with 1-octadecanol, producing C_{17} and C_{18} hydrocarbons, respectively. In the current reaction network of C_{18} stearic acid conversion, hydrodeoxygenation (HDO) proceeds preferentially through a hydrogenation–dehydration–hydrogenation pathway, with C_{18} octadecane yields exceeding 60%. However, the C_{17} and C_{18} hydrocarbon product distributions were quite different over the four Ni/HBEA catalysts.

With Ni samples prepared by impregnation, the relatively large Ni particles led to a slower metal-catalyzed decarbonylation step, and thus, the relatively more rapid dehydration–hydrogenation and isomerization steps resulted in higher selectivity to *n*-

and *iso*-C_{18} hydrocarbons, maintaining a C_{18}/C_{17} ratio of 2.2 (see Table 2-2). For the other three Ni/HBEA catalysts, the small and evenly dispersed Ni nanoparticles enhanced the rate of decarbonylation, and the decreased Brønsted acidity suppressed the dehydration and isomerization steps, leading to a lower C_{18}/C_{17} ratio of 1.9 among the alkane products (see Table 2-2). The C_{18} hydrocarbon with its selectivity higher than 60% was still the major product, which suggests that with the improved catalysts prepared by DP and ion exchange/precipitation, dehydration is still much faster than decarbonylation on the C_{18}-alcohol intermediate. Therefore, the reduced Brønsted acidity caused by these two precipitation methods would have a negligible impact on the overall hydrodeoxygenation activity. In addition, distearyl ether was also observed as a reaction intermediate, which was produced through an intermolecular dehydration of the in situ-formed 1–octadecanol. The C–O aliphatic ether bond was in turn cleaved by Ni sites through hydrogenolysis as the reaction proceeded, followed by dehydration of the C_{18} alcohol and subsequent hydrogenation of the respective alkene to produce the C_{18} hydrocarbon.

Ni leaching was explored by heating hexane to reflux with Ni catalysts in a Soxhlet extractor. The Ni content extracted in the solvent after seven days was below the detection limit of atomic absorption spectroscopy (1 ppm), indicating that these four supported Ni catalysts are very stable against leaching in nonpolar organic solvents.

In a following step, the stabilities of the four Ni/HBEA catalysts were tested by evaluating their catalytic activities during the recycling runs on stearic acid conversion at 533 K in the presence of 40 bar H_2. After each reaction, the catalysts were washed with acetone followed by drying in air at 343 K, and afterwards reused for the next catalytic run. Significant catalyst deactivation was observed for Ni/HBEA prepared by ion exchange/precipitation (see Figure 2-7A), which lost 60% of its initial activity after four reaction runs. As Ni leaching in organic solvent has been excluded, the activity loss is attributed to the aggregation of Ni nanoparticles during the successive reactions. This was confirmed by TEM measurements on the recycled catalyst samples (see Figure 2-7B). For Ni/HBEA synthesized by ion exchange/precipitation, the Ni particle size increased from 2.6 to 8.5 nm after four runs of reaction, accompanied with a drastic increase in size discrepancy (the standard deviation increased from 1.4 to 7.5 nm). Moreover, a large

portion (about 18%) of the strongly aggregated Ni particles (17–30 nm) was observed, which were absent in its fresh sample (see Figure 2-1). Therefore, it could be concluded that the most severe aggregation of Ni particles in sample prepared by ion exchange/precipitation was responsible for the highest degree of catalyst deactivation during the successive reactions.

On the other hand, Ni/HBEA prepared by DP and Ni NP methods still retained high activities even after four runs, showing comparable rates to the fresh catalysts. The higher activities and stabilities of these two catalysts are attributed to the smaller and more evenly distributed Ni particles (TEM images in Figures 2-1 and 2-7B). In recycled samples of DP and Ni NP, not only were the average diameters of Ni particles much smaller (around 5.0 nm), more importantly, these particles were more evenly distributed with deviations of 3–4 nm. Notably, the NP method led to the most stable Ni/HBEA catalyst against sintering, with only 1.1 nm growth in average particle size as well as fewest aggregated large Ni particles (> 7 nm) after recycling. Impregnated catalysts with much larger Ni particles (see Figure 2-1) were less prone to further aggregation during the reaction compared with nanometer-range Ni in the other three samples. But still, it had the lowest activities throughout the recycling tests. In contrast, the ion-exchange/precipitation method resulted in a small Ni size, which facilitated high initial reaction rates in its fresh sample. However, the large differences in particle size reduced the stability of nanoparticles, and the catalyst showed a dramatic particle size increase together with activity decrease during recycling (Figure 2-7). Therefore, we conclude that the average size and size uniformity of Ni particles are both crucial for maintaining a highly active and stable catalyst system, that is, concentration of accessible Ni facilitates high initial activity of the fresh sample, whereas good uniformity ensures high catalyst stability over prolonged usage.
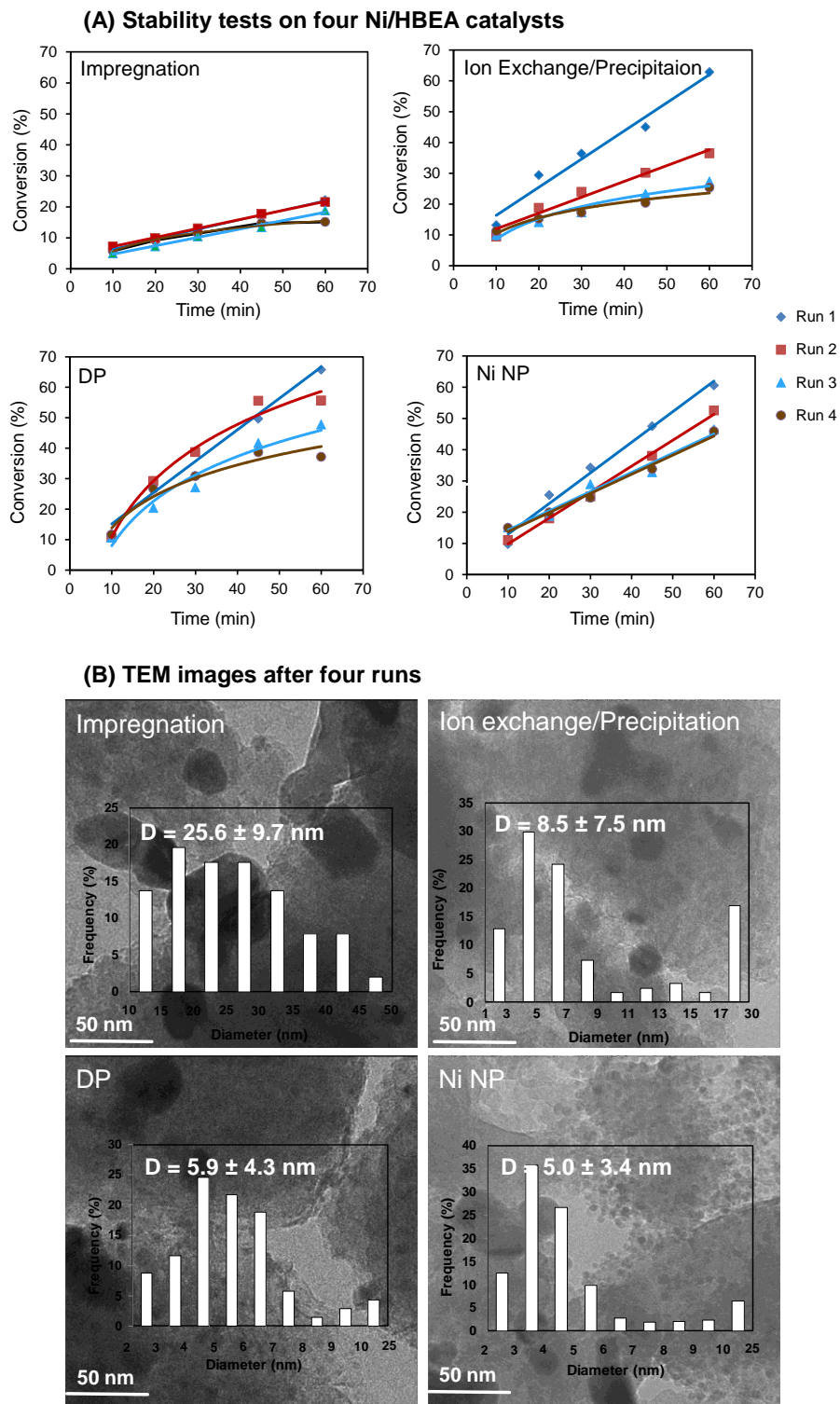
(A) Stability tests on four Ni/HBEA catalysts

(B) TEM images after four runs

Figure 2-7. A) Stability tests for the Ni/HBEA catalysts prepared by four different methods. Reaction conditions: stearic acid (2.5 g), catalyst (0.4 g), dodecane (100 mL), 40 bar H_2 (at reaction temperature 533 K), at stirring speed of 700 rpm. B) TEM images and the size distribution histograms of Ni/HBEA samples after four runs.

Generally speaking, two mechanisms are applied to explain the growth of the metal nanoparticle (shown in Figure 2-8), namely coalescence and Ostwald ripening.[35] The latter suggests a dynamic process of atom exchange between nanoclusters, and is usually considered for the discussion of catalyst growth and sintering. Ostwald ripening demonstrates the behavior of catalyst deactivation reported in the current work with four Ni/HBEA samples, in which larger Ni clusters grow further at the expense of the smaller ones which eventually shrink and disappear. Therefore, the wider size-distribution, for instance with Ni nanoparticles prepared by ion exchange/precipitation, will lead to more pronounced Ostwald ripening and faster catalyst deactivation as shown in TEM images of Figure 2-7B.
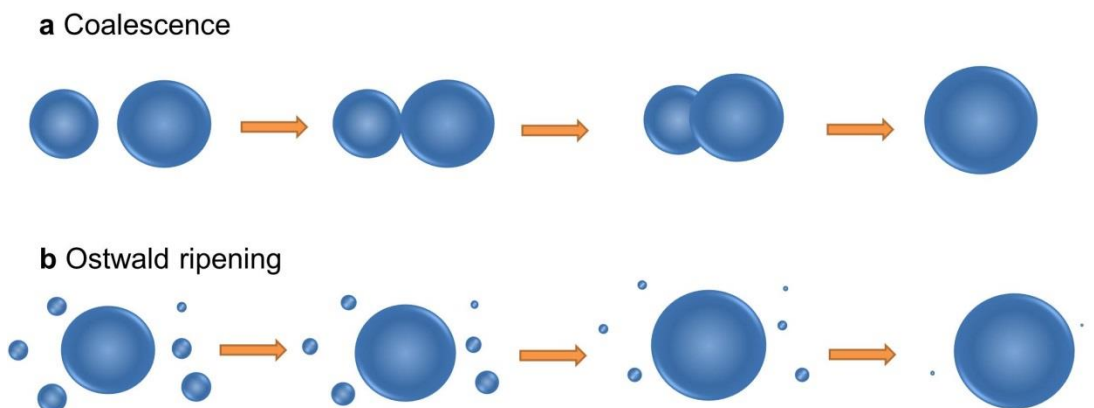

Figure 2-8. Mechanisms for the metal nanoparticle growth through
A) coalescence, B) Ostwald ripening.

2.3.4. Hydrodeoxygenation of crude microalgae oil.

Crude microalgae oil was hydrodeoxygenated with the four Ni/HBEA catalysts in the batch reactor at 533 K in the presence of 40 bar H_2 (see Figure 2-9). Microalgae oil mainly consists of neutral lipids such as mono-, di-, and triglyceride. The microalgae oil (provided by Verfahrenstechnik Schwedt GmbH) used here is composed of unsaturated C_{18} fatty acids (88.4 wt.%), saturated C_{18} fatty acids (4.4 wt.%), as well as some other C_{14}, C_{16}, C_{20}, C_{22}, and C_{24} fatty acids (7.1 wt.% in total). The mechanism for hydrodeoxygenation of microalgae oil[4a] has been proposed to proceed through an initial

metal-catalyzed hydrogenation of the double bonds in the alkyl chain, followed by hydrogenolysis of the formed saturated triglyceride leading to fatty acid and propane production. The subsequent hydrogenation of the carboxylic group of fatty acid leading to the corresponding aldehyde, for example, octadecanal, is the rate-determining step. Followed by either decarbonylation of octadecanal to produce C_{17} *n*-heptadecane and carbon monoxide (minor route), or hydrogenation of octadecanal to 1-octadecanol (major route). Acid-catalyzed alcohol dehydration and metal-catalyzed alkene hydrogenation produce the final *n*-octadecane.
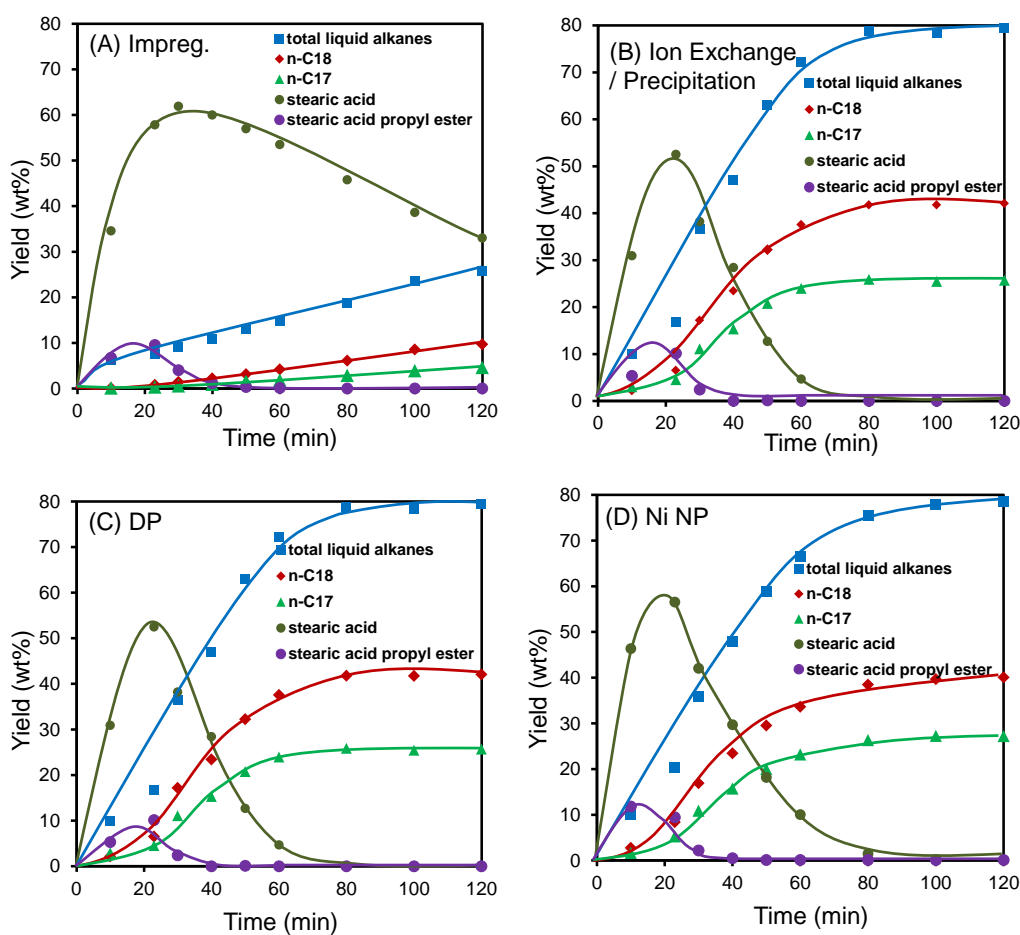

Figure 2-9. Product distributions on conversion of crude microalgae oil. Reaction conditions: microalgae oil (1.0 g), Ni/HBEA catalyst (0.2 g), dodecane (100 mL), 40 bar H_2 (at 533 K), at a stirring speed of 700 rpm.

The yields of major intermediates of stearic acid and stearic acid propyl ester firstly increased to the maxima of 50–60 and 10 wt.%, respectively, and subsequently decreased as a function of time. The stearic acid propyl ester was formed from the partial hydrogenolysis of glycerides at the beginning of the reaction, which was further hydrogenolyzed to stearic acid and propane at Ni sites as the reaction proceeded. Stearic acid was the dominant intermediate (selectivity > 70 wt.%), which verifies that fatty acid hydrogenation is the rate-determining step. Only small concentrations of octadecanol were detected during the reaction (< 2 wt.% for the impregnated sample, and < 1 wt% for the other three), demonstrating that the dehydration rate is much faster than the rates of triglyceride hydrogenolysis and fatty acid hydrogenation.

After a reaction time of 2 h, the impregnated Ni/HBEA sample only achieved 26 wt% yield of total liquid hydrocarbons, including 13.6 wt.% C_{18} and 4.6 wt.% C_{17} hydrocarbons, as well as other hydrocarbons of C_{14}–C_{24}, leaving 33 wt.% stearic acid still unconverted. Whereas by comparison, the other three catalysts realized a high total liquid alkanes yield of 79 wt.% within 2 h, which is very close to the theoretical maximum hydrocarbon yield (84 wt.%). The initial rates of total liquid alkane formation reached 4.0, 4.6, 3.6 g_{oil} g_{cat}^{-1} h^{-1} over Ni/HBEA catalysts prepared by ion exchange/precipitation, DP, and Ni NP methods, respectively (see Table 2-3). Such a rate sequence is in line with the order of Ni particle size shown from the TEM images (2.6, 2.5, and 3.9 nm). The impregnated Ni/HBEA sample only attained an alkane formation rate of 0.6 g_{oil} g_{cat}^{-1} h^{-1}, which is 6–8 times lower than those observed for the other three catalysts. The higher rates are attributed to the much smaller and highly-dispersed Ni nanoparticles, which promotes several several individual steps in the overall hydrodeoxygenation reaction including hydrogenation of double bonds, hydrogenolysis of triglyceride, decarbonylation of aldehyde, as well as the hydrogenation of fatty acids catalyzed by Ni sites. Among these steps, the remarkable enhancement on fatty acid reduction (the rate-determining step) with the optimized Ni particles is clearly visible. TOFs (normalized by accessible surface Ni atoms) for hydrodeoxygenation of crude microalgae oil attained 92, 244, 232, 185 mol_{oil} $mol_{Surf\ Ni\ atom}^{-1}$ h^{-1} over Ni/HBEA catalysts prepared by impregnation, ion-exchange/precipitation, DP, and Ni NPs methods (see Table 2-3), respectively. It has been demonstrated that the hydrogenation of stearic acid to stearic aldehyde is not

sensitive to the Ni particle size (Table 2-2). However, the TOF for the overall alkane formation from microalgae oil with the impregnated Ni catalyst (92 h^{-1}) was 2–3 times lower than those with the other three Ni catalysts (185–244 h^{-1}). This is related to the fact that alkane production from microalgae oil passes through a series of individual reactions including hydrogenation, hydrogenolysis, decarbonylation, as well as dehydration in a cascade, among which the initial primary step of C–O bond hydrogenolysis of ester has been found to be structure sensitive.[36] Therefore, the larger impregnated Ni particles (25 nm) would be expected to result in a much lower TOF for the overall cascade hydrodeoxygenation reaction compared with the other three catalysts (3 nm particle diameter).

Table 2-3. Data of hydrodeoxygenation of microalgae oil over Ni/HBEA catalysts prepared by four methods.[a]

Method	Initial rate [b]	TOF [c]	Yield of liquid products (wt.%)				
			n-C$_{18}$	*Iso*-C$_{18}$	*n*-C$_{17}$	Other HC [d]	Total
Impreg.	0.6	92	9.7	3.9	4.6	5.1	26
Ion Ex./Pre.	4.0	244	42	3.0	26	8.0	79
DP	4.6	232	43	2.7	25	7.5	79
Ni NP	3.6	185	40	2.4	27	8.2	79

[a] The reaction conditions are identical to that listed in Figure 2-8, reaction time: 2 h.

[b] Initial rates for total liquid alkane formation base on the weight of catalyst, unit: g_{oil} g_{cat}^{-1} h^{-1}.

[c] Initial rates for total liquid alkane formation base on the surface Ni atoms of catalysts, assuming the average molecular weight of oil is 240 g mol^{-1}, unit: mol_{oil} $mol_{Surf\ Ni\ atom}^{-1}$ h^{-1}.

[d] HC: hydrocarbons.

2.4. Conclusions

Ni nanoparticles supported onto and/or into HBEA zeolite prepared by four techniques, namely impregnation, ion exchange/precipitation, DP, and Ni NP methods were investigated for the hydrodeoxygenation of stearic acid and crude microalgae oil. In the catalytic tests on stearic acid conversion, Ni/HBEA catalysts prepared by DP and Ni NP methods maintained very high activities even after four runs of reaction due to the presence of more accessible, uniformly dispersed, and sintering-resistant Ni nanoparticles, confirmed by TEM, IR of adsorbed CO, and TPR-H_2 measurements. In a comparison, catalysts prepared by using ion exchange/precipitation methods achieved high initial reaction rate in its fresh sample, but showed a dramatic particle-size increase accompanied with a loss in activity during the recycling test. The impregnated Ni/HBEA sample steadily showed the lowest activity in the first and recycling runs. This indicates that the small-sized metal particles control the initial catalytic activity, and the good size uniformity ensures high catalyst stability for the longer utilization. It also highlights the importance of the narrow size-distribution of the particles, as it can minimize the growth of larger particles at the expense of smaller ones through the Ostwald ripening mechanism.

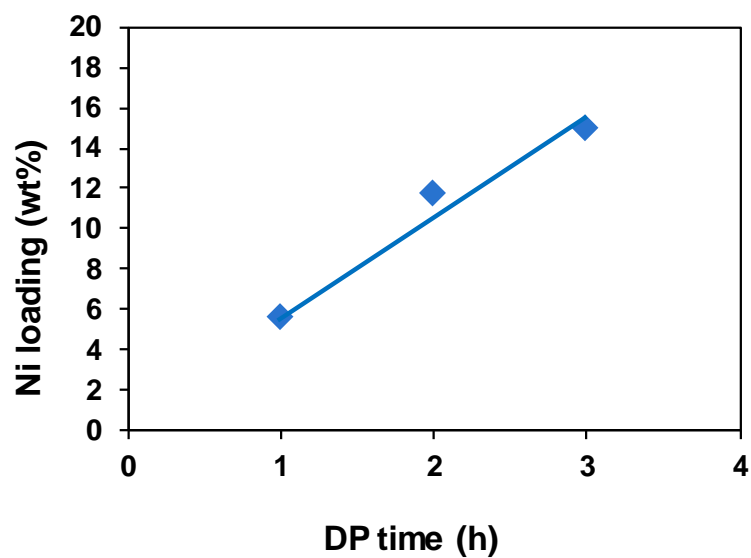## 2.5. Acknowledgements

2.6. Appendix

Figure 2A-1. Changes of Ni loading as a function of the DP time.
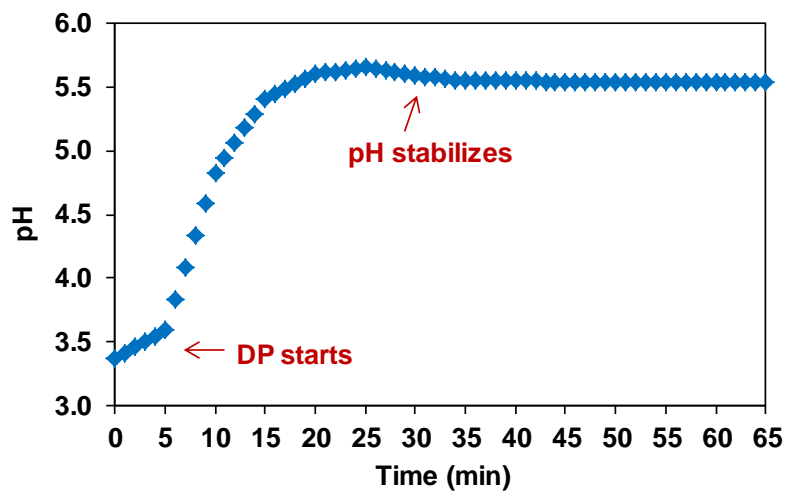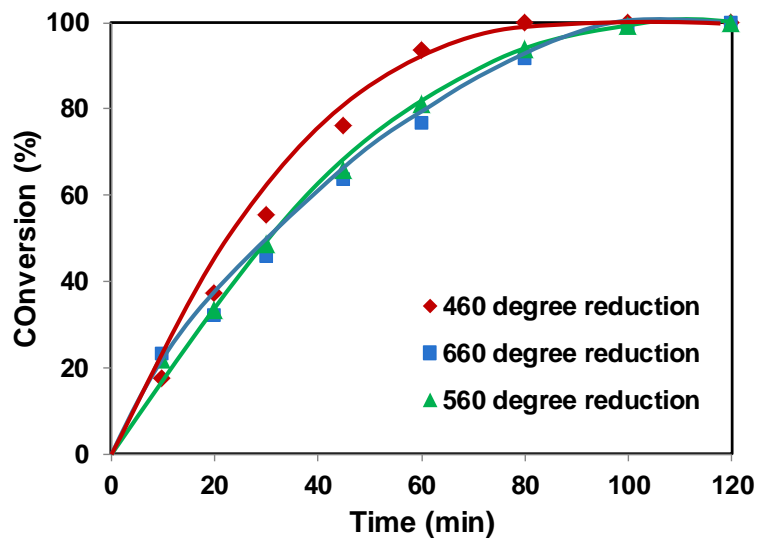

Figure 2A-2. Evolution of pH values during first hour of DP process.
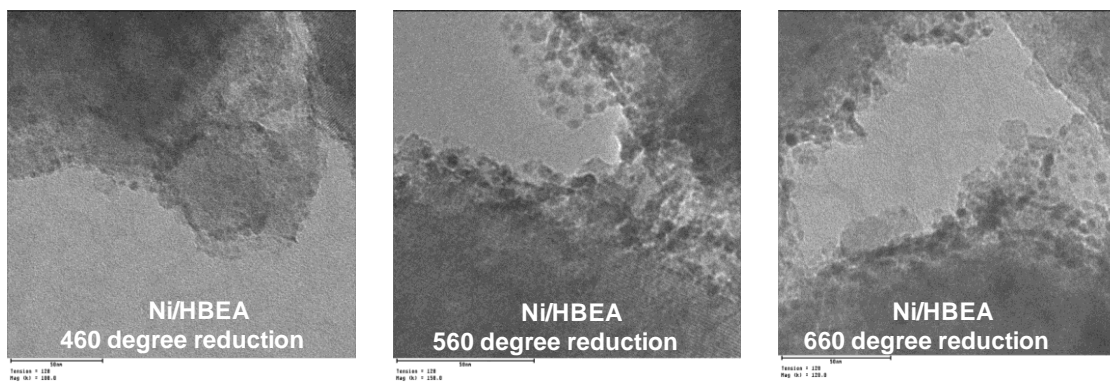
(a)

(b)

Figure 2A-3. Influence of reduction temperatures a) HDO of stearic as a function of time over Ni/HBEA reduced at different temperatures; b) TEM images of catalysts treated at different reducing temperatures.

Table 2A-1. Physicochemical properties of parent HBEA and Ni/HBEA treated at different reducing temperatures.

Reduction Temp. (°C)	Pore volume ($cm^3 g^{-1}$)			BET surface area ($m^2 g^{-1}$)		
	Micro	Meso	Total	Micro	Meso	Total
Parent HBEA	0.20	0.17	0.37	489	126	615
460	0.14	0.24	0.38	331	177	508
560	0.15	0.29	0.43	355	197	552
660	0.14	0.30	0.44	343	219	562

Table 2A-2. Concentrations of acid sites calculated from NH_3-TPD and IR of adsorbed pyridine.

Method	TPD ($\mu mol \ g^{-1}$)	IR of adsorbed pyridine ($\mu mol \ g^{-1}$)		
	Acid site	Brønsted acid site	Lewis acid site	Total
Parent HBEA	217	119	62	181
Impregnation	244	111	84	195
Ion Exchange/ Precipitation	313	36	189	225
DP	279	36	161	197
Ni NPs	334	100	140	240

2.7. References

[1] G. W. Huber, S. Iborra, A. Corma, *Chem. Rev*. **2006,** *106,* 4044.

[2] a) P. M. Schenk, S. R. Thomas-Hall, E. Stephens, U. C. Marx, J. H. Mussgnug, C. Posten, O. Kruse, B. Hankamer, *Bioenerg. Res.* **2008,** *1,* 20; b) T. M. Mata, A. A. Martins, N. S. Caetano, *Renewable Sustainable Energy Rev.* **2010,** *14,* 217.

[3] Y. Chisti, *Biofuels* **2010,** *3,* 233.

[4] a) B. Peng, Y. Yao, C. Zhao, *Angew. Chem. Int. Ed.* **2012,** *51,* 2072; b) B. Peng, X. Yuan, C. Zhao, J. A. Lercher, *J. Am. Chem. Soc.* **2012,** *134,* 9400; c) B. Peng, C. Zhao, S. Kasakov, S. Foraita, J. A. Lercher, *Eur. J. Chem.* **2013,** *19,* 4732.

[5] L. M. Velichkina, A. N. Pestryakov, A. V. Vosmerikov, I. V. Tuzovskaya, N. E. Bogdanchikova, M. Avalos, M. Farias, H. Tiznado, *Petroleum Chemistry* **2008,** *48,* 355.

[6] R. Nares, J. Ramírez, A. Gutiérrez–Alejandre, C. Louis, T. Klimova, *J. Phys. Chem. B* **2002**, *106,* 13287.

[7] M. A. Cauqui, J. M. Rodriguez-Izquierdo, *J. Non-Cryst. Solids* **1992,** *147,* 724.

[8] a) J. W. Geus, Dutch Pat. Appl. 6705,259, 1967; 6813,236, 1968; b) L. A. M. Hermans, J. W. Geus in *Preparation of Catalysts II* (Eds.: B. Delmon, P. Grange, P. A. Jacobs, G. Poncelet), Elsevier, Amsterdam, **1979,** p. 113.

[9] a) P. Burattin, M. Che, C. Louis, *J. Phys. Chem. B* **1997,** *101,* 7060; b) P. Burattin, M. Che, C. Louis, *J. Phys. Chem. B* **1998,** *102,* 2722.

[10] M. Han, Q. Liu, J. He, Y. Song, Z. Xu, J. Zhu, *J. Adv. Mater.* **2007,** *19,* 1096.

[11] a) H. Bönnemann, W. Brijoux, R. Brinkmann, T. Joussen, *Angew. Chem.* **1990,** *102,* 324; *Angew. Chem. Int. Ed. Engl.* **1990,** *29,* 273; b) Y. Hou, S. J. Gao, *J. Mater. Chem.* **2003,** *13,* 1510.

[12] S. Carenco, C. Boissière, L. Nicole, C. Sanchez, P. Le Floch, N. Mézailles, *Chem. Mater.*, **2010**, *22,* 1340.

[13] a) J. S. Bradley, B. Tesche, W. Busser, M. Maase, M. T. Reetz, *J. Am. Chem. Soc.* **2000,** 122, 4631; b) N. Cordente, M. Respaud, F. Senocq, M.-J. Casanove, C. Amiens, B. Chaudret, *Nano Lett.* **2001,** *1,* 565; c) M. R. Knecht, J. C. Garcia-Martinez, R. M. Crooks, *Chem. Mater.* **2006,** *18,* 5039.

[14] Ö. Metin, V. Mazumder, S. Özkar, S. Sun, *J. Am. Chem. Soc.* **2010**, *132,* 1468.

[15] a) A. Gil, A. Días, L. M. Gandía, M. Montes, *Appl. Catal. A* **1994**, *109*, 167; b) J. van de Loosdrecht, A. M. van de Kraan, A. J. van Dillen, J.W. Geus, *J. Catal.* **1997**, *170*, 217; c) M. Che, Z. Cheng, C. Louis, *J. Am. Chem. Soc.* **1995**, *117*, 2008.

[16] B. Mile, D. Stirling, M. A. Zammitt, A. Lovell, M. Webb, *J. Catal.* **1988,** *114,* 217.

[17] E. Marceau, M. Che, J. Čejka, A. Zukal, *ChemCatChem* **2010,** *2,* 413.

[18] a) A.–H. Lu, E. L. Salabas, F. Schüth, *Angew. Chem. Int. Ed.* **2007,** *46,* 1222; b) Y. Hou, S. Gao, *J. Mater. Chem.* **2003,** *13,* 1510; c) D. Chen, J. Li, C. Shi, X. Du, N. Zhao, J. Sheng, S. Liu, *Chem. Mater.* **2007,** *19,* 3399.

[19] K. Hadjiivanov, M. Mihaylov, D. Klissurski, P. Stefanov, N. Abadjieva, E. Vassileva, L. Mintchev, *J. Catal.* **1999,** *185,* 314.

[20] a) A. G. Sault, C. H. F. Peden, E. P. Boespflug, *J. Phys. Chem.* **1994,** *98,* 1652.

[21] L. Bonneviot, F. Cai, M. Che, M. Kermarec, O. Legendre, C. Lepetit, D. Olivier, *J. Phys. Chem.* **1987,** *91,* 5912.

[22] P. H. Kasai, R. J. Bishop Jr., D. McLeod Jr., *J. Phys. Chem.* **1978,** *82,* 279.

[23] K. G. Ione, V. N. Romannikov, A. A. Davydov, L. B. Orlova, *J. Catal.* **1979,** *57,* 126.

[24] J. Leglise, A. Janin, J. C. Lavalley, D. Cornet, *J. Catal.* **1988,** *114,* 388.

[25] K. Hadjiivanov, H. Knczinger, M. Mihaylov, *J. Phys. Chem. B* **2002,** *106,* 2618.

[26] a) T. C. Sheng, B. Rebenstorf, *Langmuir* **1991,** *7,* 2659; b) C. L. Angell, P. C. Schaffer, *J. Phys. Chem.* **1966,** *70,* 1413.

[27] J. B. Peri, *J. Catal.* **1984,** *86,* 84.

[28] M. Kermarec, D. Olivier, M. Richard, M. Che, F. Bozon-Verduraz, *J. Phys. Chem.* **1982,** *86,* 2818.

[29] E. Garbowski, J. C. Vedrine, *Chem. Phys. Lett.* **1977,** *48,* 551.

[30] M. Mihaylov, K. Hadjiivanov, *Langmuir* **2002,** *18,* 4376.

[31] C. Louis, Z. Cheng, M. Che, *J. Phy. Chem.* **1993,** *97,* 5703.

[32] a) M. Mihaylov, K. Hadjiivanov, H. Knczinger, *Catal. Lett.* **2001,** *76,* 59; b) S. Derrouiche, D. Bianchi, *Appl. Catal. A* **2006,** *313,* 208.

[33] D. G. Blackmond, E. I. Ko, *J. Catal.* **1985,** *96,* 210.

[34] a) B. I. Mosqueda-Jim_nez, A. Jentys, K. Seshan, J. A. Lercher, *J. Catal.* **2003,** *218,* 348; b) D. L. Hoang, H. Berndt, H. Miessner, E. Schreier, J. Volter, H. Lieske, *Appl. Catal. A* **1994,** *114,* 295.

[35] a) S. T. Gentry, S. F. Kendra, M. W. Bezpalko, *J. Phys. Chem. C* **2011,** *115,* 12736; b) P. Dagtepe, V. Chikan, *J. Phys. Chem. C* **2010,** *114,* 16263 – 16269.

[36] a) J. He, C. Zhao, J. A. Lercher, *J. Am. Chem. Soc.* **2012,** *134,* 20768; b) B. Coq, F. Figueras, Coord. *Chem. Rev.* **1998,** 178 , 1753.

Chapter 3

Dehydration of Octadecanol over H-BEA: A Combined Experimental and Computational Study

Liquid phase dehydration of 1-octdecanol, which is intermediately formed during the hydrodeoxygenation of microalgae oil, has been explored in a combined experimental and computational study. The alkyl chain of C_{18} alcohol interacts with acid sites during diffusion inside the zeolite pores, resulting in an inefficient utilization of the Brønsted acid sites for samples with high acid site concentrations. The parallel intra- and inter-molecular dehydration pathways having different activation energies pass through alternative reaction intermediates. Formation of surface-bound alkoxide species is the rate-limiting step during intramolecular dehydration, whereas intermolecular dehydration proceeds via a bulky dimer intermediate. Octadecene is the primary dehydration product over H-BEA at 533 K. Despite of the main contribution of Brønsted acid sites towards both dehydration pathways, Lewis acid sites are also active in the formation of dioctadecyl ether. The intramolecular dehydration to octadecene and cleavage of the intermediately formed ether, however, require strong BAS.

3.1. Introduction

Fatty alcohols, especially those with chain length of C_{12} and higher, are important base materials for the synthesis of detergents and surfactants.[1,2] In our recent contributions,[3,4] 1-octadecanol has been identified as an important intermediate during the conversion of microalgae oil on dual functional catalysts with Ni nanoparticles supported on zeolite BEA. Hydrodeoxygenation of microalgae oil has been proposed to proceed primarily through Ni catalyzed hydrogenation of the double bonds in the alkyl chain, followed by hydrogenolysis of the saturated triglyceride forming fatty acid. The subsequent hydrogenation of the carboxylic group of fatty acid leads to production of the corresponding aldehyde, mainly octadecanal, which is in turn hydrogenated by Ni to 1-octadecanol. In the presence of acidic zeolites, octadecanol is dehydrated to the corresponding C_{18} alkene, which is rapidly hydrogenated, leading to octadecane. While it is readily deduced that the series of hydrogenation steps are catalyzed by Ni particles at the external surface, the dehydration of the long chain alcohol on zeolite acid sites is less understood.

Dehydration of alcohols has been investigated over a wide spectrum of solid catalysts including metal oxides, sulfides, mineral salts, ion exchange resins, as well as molecular sieves in both vapor and liquid phase.[5] With exception of methanol, the dehydration of an aliphatic alcohol proceeds via two pathways, i.e., the intermolecular dehydration to ethers and the intramolecular dehydration to alkenes.[6] Ether formation is favored by lower reaction temperatures whereas alkene is the preferred product at higher temperatures.[7]

Zeolite BEA comprises of a three-dimensional system defined by 12-membered ring channels. It consists of two intersecting channels with one having a cross-section of 7.6×6.4 Å running in x direction, and connects to the other through perpendicular openings of 5.6×6.6 Å in y direction.[8,9] H-BEA was found to be a better acid component in comparison with H-ZSM-5 during the conversion of microalgae oil, because it hardly cracked alkanes or alkenes under the reaction conditions applied.[4] The superior performance of zeolite BEA was attributed to its moderate acidity and relatively large pore openings.[4] Brønsted acid sites are located generally inside the micropores of a

zeolite structure, but sites at the pore entrance exist. When 1-otadecanol is considered as reactant, its interaction with the acid sites within the micropores of H-BEA may lead to transport limitations, hence it is important to understand the catalytic conversion of 1-octadecanol on both internal and external BAS/LAS sites.

First principles based theoretical modeling plays an important role in aiding the fundamental understanding of zeolite catalyzed reactions.[10,11] In this regard, density functional theory (DFT) calculations were widely used to study the interactions of various alcohols with zeolites and reaction pathways over BAS sites.[12-19] In the present work, dehydration of octadecanol (C_{18}-OH) on H-BEA in the liquid phase is explored in a combined experimental and theoretical approach. The impact of acid sites location on the overall activity as well as the possible contributions of LAS to the intermolecular dehydration was probed experimentally. The parallel dehydration pathways over H-BEA were studied using DFT calculations. The roles of steric constraints imposed by the uniform microporous structure of BEA on pathway selectivity were also discussed.

3.2. Experimental and theoretical methods

3.2.1. Chemicals

All chemicals were obtained from commercial suppliers and used as received. Octadecylamine (Aldrich, $\geq$ 99.0%), hexane (Sigma–Aldrich, $\geq$ 97.0%, CHROMASOLV®), 1-octadecanol (Fluka, $\geq$ 99.5%, Selectophore™), dodecane (Sigma–Aldrich, $\geq$ 99%, ReagentPlus®), quinoline (Aldrich, 98%, reagent grade), 4-methylquinoline (Aldrich, $\geq$ 99%), 2,4-dimethylquinoline (TCI Deutschland GmbH, > 95.0%), benzo[f]quinoline (TCI Deutschland GmbH, > 98.0%). NH$_4$-BEA with framework Si/Al ratios of 19 and H-BEA with Si/Al = 180 were purchased from Zeolyst international, H-BEA with Si/Al = 75 were obtained from Clariant. All three zeolites were calcined in air at 823 K for 6 h before usage.

3.2.2. Preparation of poisoned zeolites

2×10^{-3} mol of poison, i.e., octadecylamine, quinoline, 4-methylquinoline, 2,4-dimethylquinoline and benzo[f]quinoline, was dissolved in 100 mL hexane, and 5 g of parent H-BEA zeolite (Si/Al = 75) was suspended in the prepared solution. The suspension was then heated to 343 K and maintained at this temperature for 24 h under constant stirring. After cooling to ambient temperature, the treated zeolite was vacuum filtered and washed three times with hexane. This sample was dried at 533 K overnight to eliminate physisorbed poison molecules. Excess amounts of octadecylamine, quinoline, and its derivatives were applied, which were two times higher than the concentration of BAS present in the parent zeolite probed by infrared (IR) spectra of adsorbed pyridine.

3.2.3. Catalyst characterization

The IR spectra of adsorbed CO at low temperature were recorded on a Vertex 70 spectrometer, Bruker Optics, at a resolution of 4 cm^{-1}. The catalyst sample was prepared as a self-supporting wafer and activated at in vacuum ($p = 10^{-6}$ mbar) for 2 h at 533 K with a heating rate of 5 K/min. After pretreatment, the system was cooled to 123 K, and a spectrum of the activated sample was recorded. CO was adsorbed with an equilibrium pressure of 1 mbar, followed by outgassing to remove physisorbed CO. The IR spectra were recorded until changes in the spectra were not observed. To enhance the thermal conductivity 10 mbar He was introduced. All spectra during CO adsorption were recorded at 123 K. For a direct comparison of the CO surface coverage, the spectra were normalized by the weight of the respective wafer.

The IR spectra of adsorbed pyridine (Py-IR) were recorded with a Thermo Nicolet 5700 spectrometer at a resolution of 4 cm^{-1}. The catalyst wafer was activated in vacuum ($p = 10^{-7}$ mbar) at 533 K for 2 h (heating rate = 5 K/min). After cooling to 423 K, the sample was equilibrated with 0.1 mbar of pyridine for 30 min, followed by outgassing for 1 h. Then the IR spectra of chemisorbed pyridine were recorded. For quantification, molar integral extinction coefficients of 0.73 cm/μmol and 0.96 cm/μmol were used for the characteristic vibration bands of pyridinium ions and pyridine bound to Lewis acid

sites respectively. These were determined from a standard sample with known acid site concentrations.

Temperature programmed desorption (TPD) of NH_3 was performed in a 6–fold parallel reactor system. The H-BEA zeolites with varied Si/Al ratios were activated in He at 773 K with a heating rate of 5 K/min for 1 h. NH_3 was adsorbed with a partial pressure of 1 mbar at 373 K. Subsequently, the samples were purged with He (30 mL/min) for 2 h to remove physisorbed molecules. For the temperature programmed desorption measurement, the samples were heated up in flowing He from 373 to 1033 K with a temperature increment of 10 K/min to desorb ammonia. The desorbed species ($m/z^+ = 16$ signal) were monitored by mass spectrometry (Balzers QME 200). For acid site quantification, a reference (HZSM-5, Si/Al = 45 from Clariant) with known acidity was used to calibrate the signal.

The BET specific surface area and the pore volume were determined by N_2 adsorption–desorption isotherms measured at 77 K using a PMI automatic sorptometer. The sample was activated in vacuum at 473 K for 2 h before the measurements. The specific surface areas were calculated by applying the Brunauer–Emmett–Teller (BET) theory, and the *t*-plot method was used to determine the pore volumes.

3.2.4. Catalytic measurements

The kinetic study of liquid phase dehydration of 1-octadecanol was carried out as follows: 5.0 g C_{18}-OH, 0.025 g (or 0.05 g in the experiments of poison studies) catalyst, and 100 mL dodecane were charged into a batch autoclave (Parr Instrument, 300 mL), and stirred at a speed of 680 rpm. The reactor was purged with 10 bar N_2 at ambient temperature, and then heated up to 533 K at which the reaction started. The liquid products were sampled in situ, and analyzed by a Shimadzu GC–MS equipped with a FID detector and a HP–5 capillary column. Conversion = (weight of converted reactant/weight of the starting reactant) $\times$ 100%. Yield of liquid products (C%) = (C atoms in liquid products/C atoms in the starting reactant) $\times$100%.

3.2.5. Computational details

First principles density functional theory calculations were used to study the dehydration and etherification of C_{18} alcohol ($C_{18}H_{37}OH$, stearyl alcohol, 1-octadecanol) inside and outside H-BEA zeolite using the cp2k package.[20,21] A periodic three-dimension all siliceous BEA structure of $Si_{96}O_{192}$ with experimental lattice parameters of $12.6614 \times 25.3228 \times 26.4061$ Å^3 was used in this work.[22] The unit cell of the H-BEA with Si/Al=15 ratio then was built by replacing six Si atoms with six Al atoms. This resulting negative charges were compensated by adding four H atoms at the oxygen atoms which are close neighbors of Al atoms on the zeolite frame, yielding the active Brønsted acidic sites, i.e., Si-O(H)-Al-O of the H-BEA zeolite. The GGA-PBE functional and the pseudopotentials of Geodecker, Teter, and Hutter were used in the calculations. The cutoff energy of the auxiliary plane wave basis was set as 360 Ry. The BFGS algorithm with SCF convergence criteria of 1.0×10^{-8} au was used in geometrical optimizations. To compensate the long-range van der Waals (vdW) interaction between the adsorbate and the zeolite, the DFT-D3 scheme[23] with an empirical damped potential term was added into the energies obtained from exchange-correlation functional in our calculations. Transition states for protonation, configurational transformation and dehydration steps in the H-BEA pore were located using the CI-NEB method[24,25] with seven images between initial and final state. Test calculations showed that the energy change was negligible (< 0.01 eV) when the maximum force convergence criteria of 0.001 hartree/bohr was used. The identified transition states were further confirmed by the vibrational analysis. Only one imaginary frequency was found for the transition state.

The adsorption energy $E_{A,ads}$ of C_{18} alcohol in the largest pore of H-BEA is calculated as follows

$$E_{C_{18},ads} = E_{C_{18}+H-BEA} - E_{H-BEA} - E_{C_{18}}$$

where $E_{C_{18}+HBEA}$ is the total energy of the C_{18} alcohol adsorbed in the pore of H-BEA; E_{H-BEA} is the total energy of the H-BEA; and $E_{C_{18}}$ is the total energy of the C_{18} alcohol molecule in vacuum.

For the zeolite acid-catalyzed reaction, the confinement and steric hindrance strongly affect the stabilities of reaction intermediates and transition states.[26-30] To account for important entropic contribution and zero-point energy (ZPE) corrections, in addition to the reaction enthalpy (ΔH), we also calculated Gibbs free energy (ΔG) along reaction pathways using standard thermodynamic method.[31]

$$\Delta G = \Delta H - T\Delta S \tag{1}$$

$$\Delta H = \Delta U_{trans} + \Delta U_{rot} + \Delta U_{vib} + \Delta(ZPE) + \Delta H_{elec} \tag{2}$$

$$\Delta S = \Delta S_{trans} + \Delta S_{rot} + \Delta S_{vib} \tag{3}$$

where the translational, rotational, and vibrational contributions to the entropy and enthalpy were given below. The electronic term (ΔH_{elec}) was directly derived from DFT calculations. The calculated activation barrier ($\Delta H^{\pm}$) and activation free energy barriers ($\Delta G^{\pm}$) then were obtained by

$$\Delta H^{\pm} = \Delta U_{trans}^{\pm} + \Delta U_{rot}^{\pm} + \Delta U_{vib}^{\pm} + \Delta(ZPE)^{\pm} + (E_{elec}^{TS} - E_{elec}^{IS}) \tag{4}$$

$$\Delta G^{\pm} = \Delta H^{\pm} - T\Delta S^{\pm} \tag{5}$$

where E_{elec}^{TS} and E_{elec}^{IS} were the electronic energy difference between the transition state (TS) and initial state (IS) of each elementary reaction step.

3.3. Results and discussion

3.3.1. Interaction of 1-octadecanol with H-BEA

As even very bulky bases, such as 2,6-di-tert-butyl-pyridine are able to access the pores of HBEA[32], octadecylamine (C_{18}-NH_2) was chosen to probe the acid sites which are potentially active in the conversion of C18-OH, because its size and structure is resembles that of 1-octadecanol.

The IR spectrum of the C_{18}-NH_2 exposed sample showed a complete disappearance of bands at 3605 cm^{-1} associated with bridging hydroxyl group (Figure 3-1a), indicating that all BAS were interacting with the base. Coordinatively bound amine showed a characteristic -NH_2 deformation band at 1604 cm^{-1}, while the band at 3255 cm^{-1} was

assigned to N-H stretching corresponding to protonated amine.[33] This suggests that the probe molecules interacted with both Brønsted and Lewis acid sites (LAS). Strong bands of C-H stretching at 2956 2924 and 2854 cm^{-1} as well as C-H bending vibrations at 1468, 1457 cm^{-1} are attributed to the long alkyl chain of C_{18}-OH, which has entered the zeolite pores.[34]
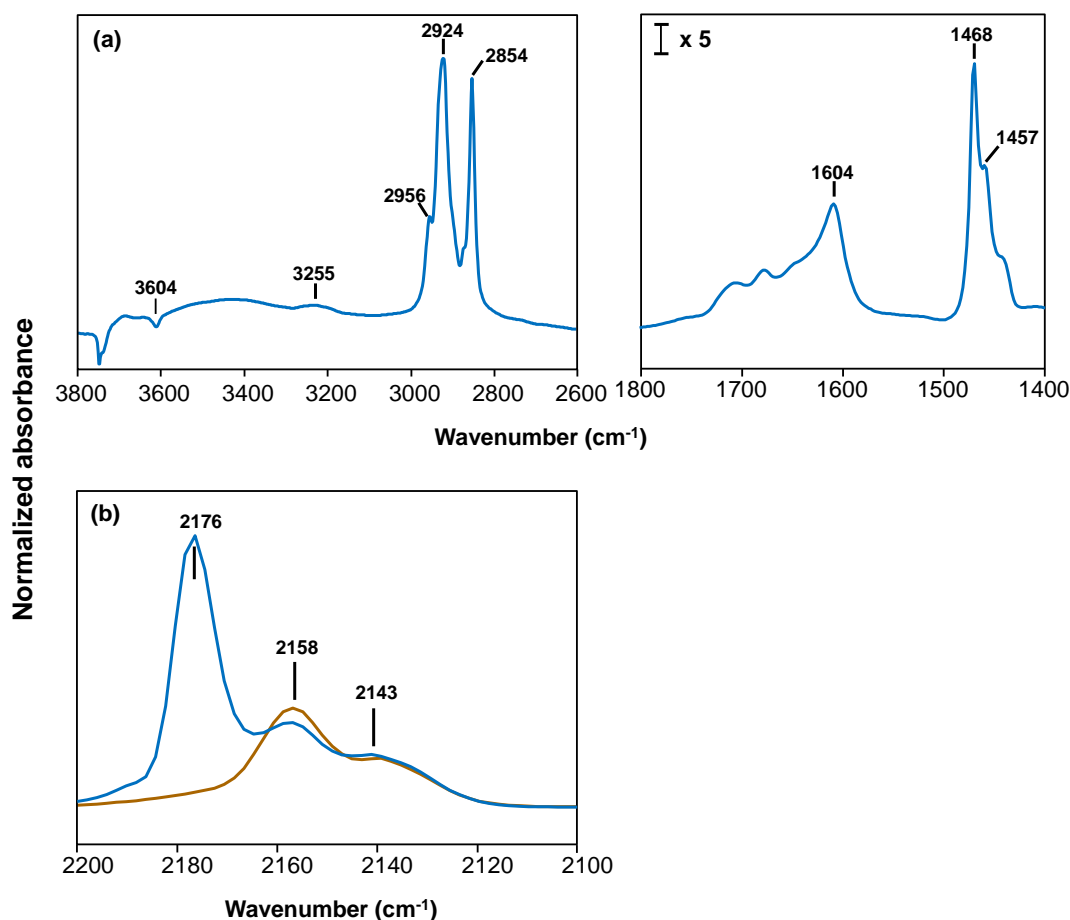

Figure 3-1. (a): Differential spectrum of C_{18}-NH$_2$ exposed sample after activation in vacuum at 533 K for two hours. (b): IR spectra of adsorbed CO at 1 mbar of equilibrium pressure and 123K; —— parent H-BEA (Si/Al=75) —— after C_{18}-NH$_2$ exposure.

Upon adsorption of CO on parent H-BEA at low temperature, three bands at 2176, 2157 and 2140 cm^{-1} (Figure 3-1b) appeared. The first two bands were attributed to CO interacting with SiOHAl and SiOH groups, respectively, the third to physisorbed CO.[35]

The band at 2176 cm^{-1} assigned to CO interacting with BAS was absent after exposre to C$_{18}$-NH$_2$, indicating octadecylamine interacts with all BAS.

With pyridine as probe for the remaining acidity of the amine-treated zeolite, small concentrations of accessible BAS and LAS were detected (Figure 3-2, Table 3-1). It is speculated that this small concentration is related to pyridine interacting with those acid sites, which were originally covered with the alkyl chain of C$_{18}$-NH$_2$. We cannot rule out, however, that pyridine is able to replace a small fraction of C$_{18}$-NH$_2$.
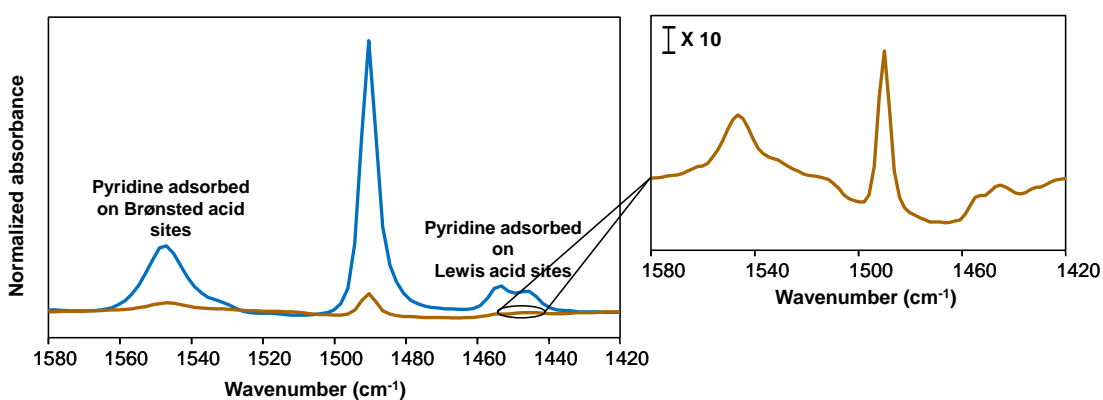
Figure 3-2. IR spectra of adsorbed pyridine at 0.1 mbar of equilibrium pressure and 423 K.

— parent H-BEA (Si/Al=75) — after C$_{18}$-NH$_2$ treatment.

Table 3-1. Acid characterization of parent H-BEA and sample after C$_{18}$-NH$_2$ treatment measured by IR spectra of adsorbed pyridine.

H-BEA (Si/Al=75)	Py-IR probed acid sites (μmol·g^{-1})		
	Brønsted	Lewis	Total
parent	164	37	201
C$_{18}$-NH$_2$	21	4.4	26

To explore the catalytic consequences of the acid sites concentration further, a series of H-BEA zeolites with varying Si/Al ratios were investigated for the dehydration of 1-octadecanol (Figure 3-3a). The particle sizes and the physicochemical properties of the

three samples were comparable (Table 3A-1 and Figure 3A-1 in Appendix), ruling out strong effects induced by differences in diffusion.
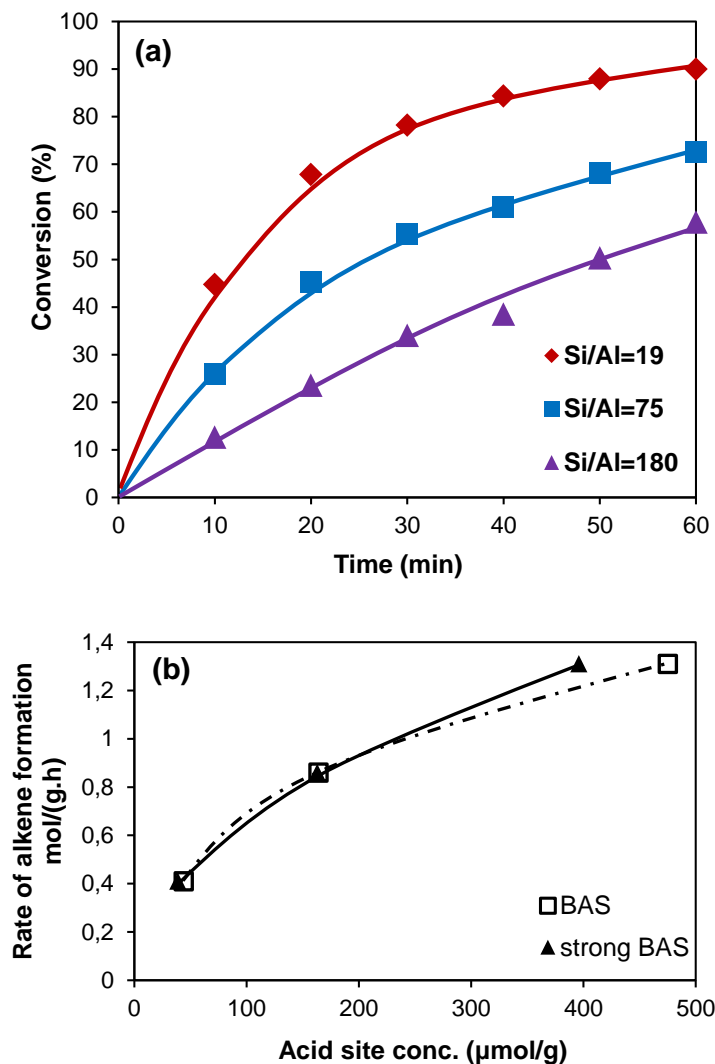

Figure 3-3. (a) Intramolecular dehydration of 1-octadecanol over H-BEAs with varied Si/Al ratios as a function of reaction time. Reaction conditions: 5g C$_{18}$-OH, 0.025g H-BEA, 100mL dodecane, at 533 K, 10 bar N$_2$ (ambient temperature), stirring at 680 rpm; (b) Relations of intramolecular dehydration with concentrations of Brønsted acid sites in H-BEAs with varied Si/Al ratios.

Though it has been reported that Brønsted acid sites are the primary active sites for zeolite catalyzed alcohol dehydration,[36] one could note that the initial rate of intramolecular dehydration of 1-octadecanol was not be directly proportional to the

concentrations of BAS (Figure 3-3b, Table 3-2). This suggests either that the acid strength of the BAS varies drastically between the materials or only a fraction of the zeolite particles is actually effective during the reaction. According to the theory of Next Nearest Neighbors (NNN), the strength of BAS is inversely related to the number of NNN, which is constant and equal to 0 for Si/Al ratios higher than 11.[37] Therefore, the relative strength of Brønsted acid sites is not considered a plausible explanation for the different TOFs observed for the three samples with varied Si/Al ratios. An estimate of the catalyst efficiency (Table 3-2) suggests that the latter postulation is correct (see details in Appendix), and the apparent TOF of H-BEA-19 represents the lower limit of a true TOF.

Table 3-2. Dehydration activities of H-BEAs with varied Si/Al ratios and their Brønsted acidities probed by IR spectra of adsorbed pyridine.

Si/Al ratio	Rate $(mol \cdot g^{-1} \cdot h^{-1})$	BAS $(\mu mol \cdot g^{-1})$	TOF_{BAS} (h^{-1})	Strong BAS $(\mu mol \cdot g^{-1})$	$TOF_{Strong\ BAS}$ (h^{-1})	η
19	1.31	475	2754	396	3304	0.43
75	0.86	164	5215	163	5247	0.74
180	0.41	44	9219	39	10401	0.93

While the decreasing efficiency could be related to the higher concentration of BAS, it should be mentioned for completeness that differences in the distribution of acid sites could also influence the activity and utilization of BAS in H-BEA. We can rule out that accessibility of the zeolite acid sites was limited, because C_{18}-NH_2 was able to access all BAS (Figure 3-1). While the complex interaction of the long alkyl chain of 1-octadecanol with BAS also lead to differences in the efficiency of the three catalysts.

Theoretical modeling also supports this explanation. The AIMD simulations show that a relatively high energy was required for 1-octadecanol to diffuse into the pore structure of H-BEA although neither the alkyl chain nor the alcohol group should face the steric constraints. The methylene segments on its long alkyl chain of C_{18} alcohol is highly prone to interact with the Brønsted acid sites during the diffusion process (Figure 3A-2).

3.3.2. Parallel dehydration pathways of 1-octadecanol

Except for octadecene as the major product derived from intramolecular dehydration, substantial concentrations of ether from intermolecular dehydration were observed, indicating the existence of a bimolecular pathway. The apparent activation energies for intra- and inter-molecular dehydration over H-BEA (Si/Al=75) were 166 and 92 kJ·mol^{-1}, respectively (Figure 3-4).
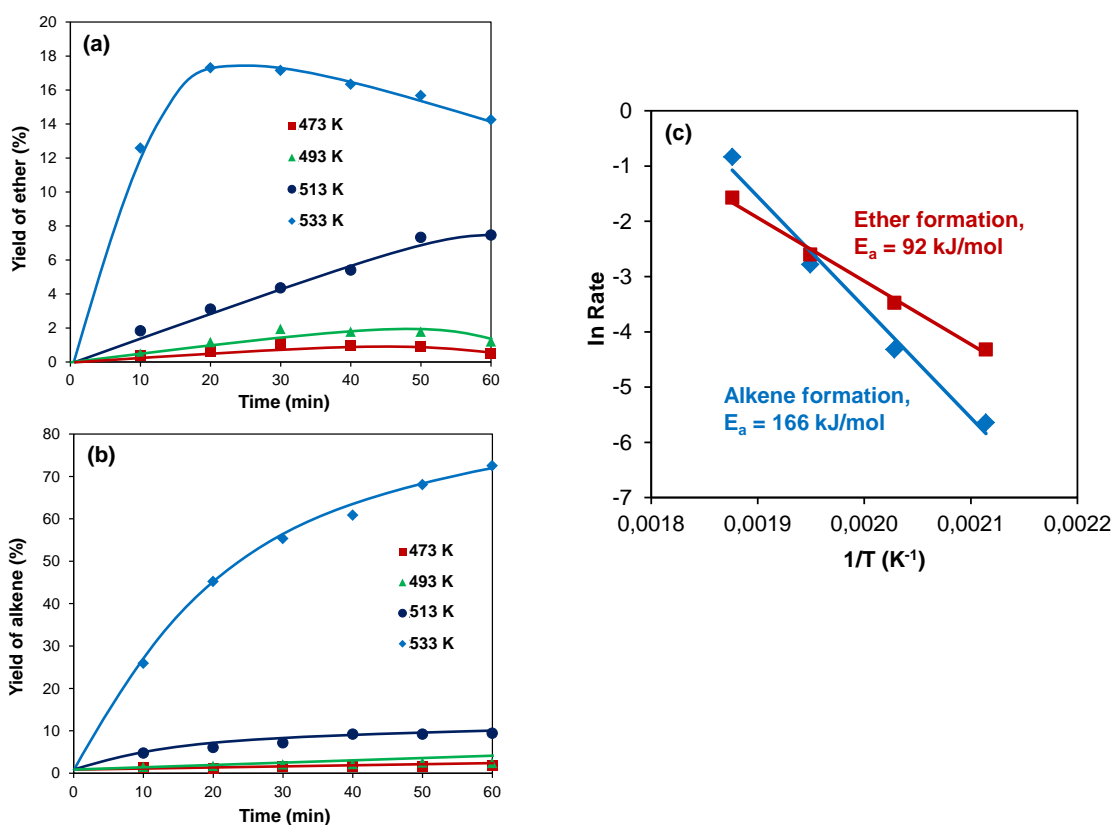

Figure 3-4. Dehydration of 1-octadecanol over H-BEA (Si/Al=75) at Temp. from 473-533 K as a function of reaction time; (a) yield of ether, (b) yield of alkene, (c) Arrhenius plots for intra- and inter-molecular dehydration. Reaction conditions: 5g C_{18}-OH, 0.025g H-BEA, 100mL dodecane, 10 bar N_2 (ambient temperature), stirring at 680 rpm.

The proposed mechanisms for intra- and intermolecular dehydration of 1- octadecanol over H-BEA zeolite were illustrated in Scheme 3-1. Following the similar pathway

proposed by Kondo *et al.*,[38] the intramolecular dehydration starts with the adsorption of 1-octadecanol on BAS (step 1 in Scheme 3-1a), subsequent decomposition of the alcohol monomer leads to the formation of a surface-bound octadecoxide intermediate and water via C-O bond cleavage accompanied by re-hybridization of the α-carbon (step 2 in Scheme 3-1a). Desorption of the octadecoxide intermediate produces octadecene as intramolecular dehydration product and regenerates the BAS site (step 3 in Scheme 3-1a).
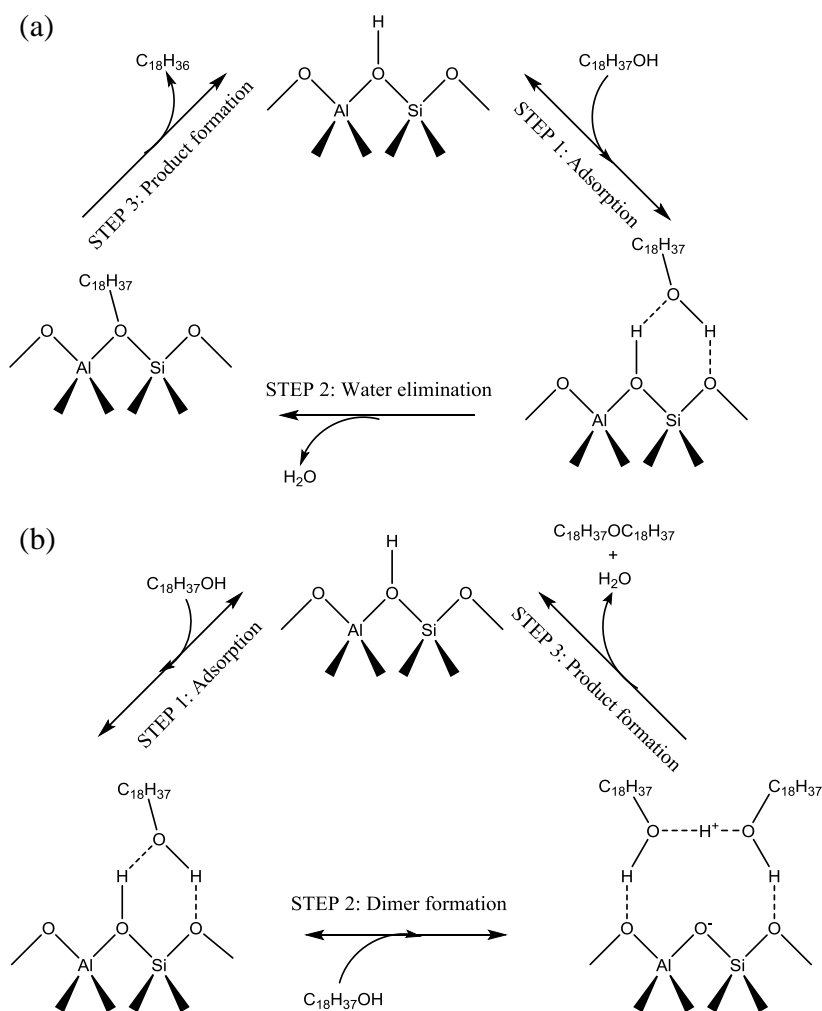
Scheme 3-1. Proposed intramolecular and intermolecular dehydration mechanisms for 1-octadecanol (a) octadecene and (b) dioctadecyl ether over H-BEA zeolite.

The proposed pathway The proposed pathway is confirmed by the DFT calculated energy profile over BAS inside the pore of the H-BEA zeolite shown in Figure 3-5. 1-

Octadecanol firstly adsorbs on the BAS with the binding energy of −265 kJ·mol⁻¹. The adsorbed monomer then dehydrates to the surface bound octadecoxy group and water via C-O bond scission. Finally, one H atom of the reaction intermediate directly transfers back to the zeolite forming a new BAS and produces the dehydration product octadecene ($C_{18}H_{36}$). Our calculation results show that the C-O bond scission step is the rate-limiting step in the catalytic cycle. The calculated apparent activation barrier for the intramolecular dehydration route is 161 kJ·mol⁻¹, which is in excellent agreement with the measured activation barrier of 166 kJ·mol⁻¹ since the reaction order for this pathway is zero (Figure 3A-3). The optimized structures of steady states (ST) and transition states (TS) are given in Figure 3-6.
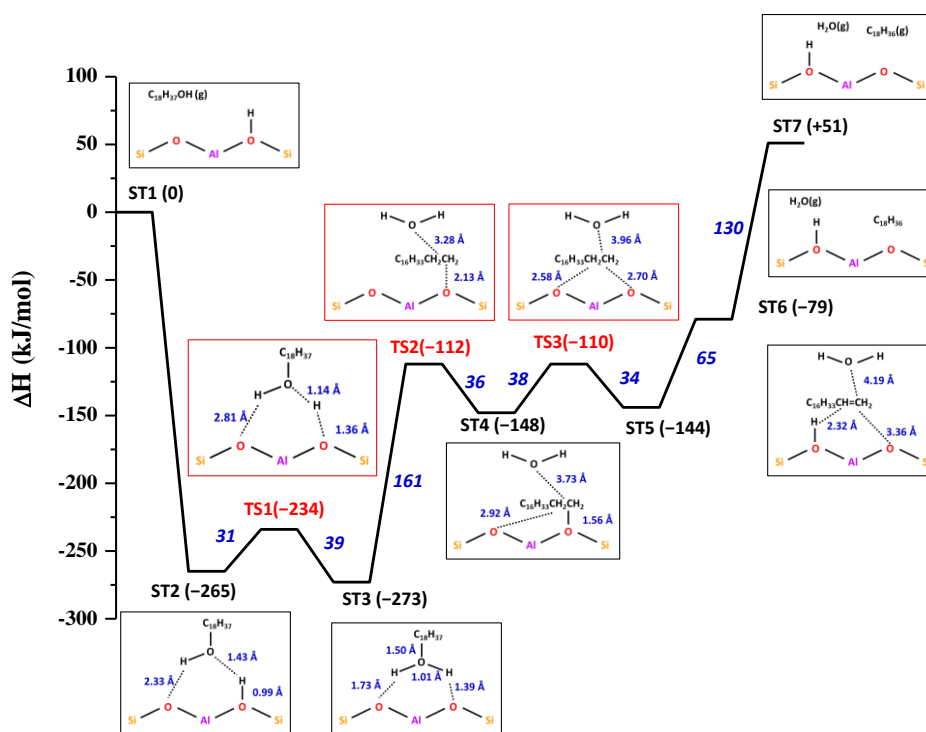

Figure 3-5. DFT calculated energy profile of dehydration of 1-octadecanol over BAS of H-BEA (Si/Al=15).

(a) $C_{18}H_{37}OH$

(b) $C_{18}H_{37}OH_2$

(c) $C_{18}H_{37} + OH_2$

(d) $C_{18}H_{36} + OH_2$

(e) TS: $C_{18}H_{37}OH....H$

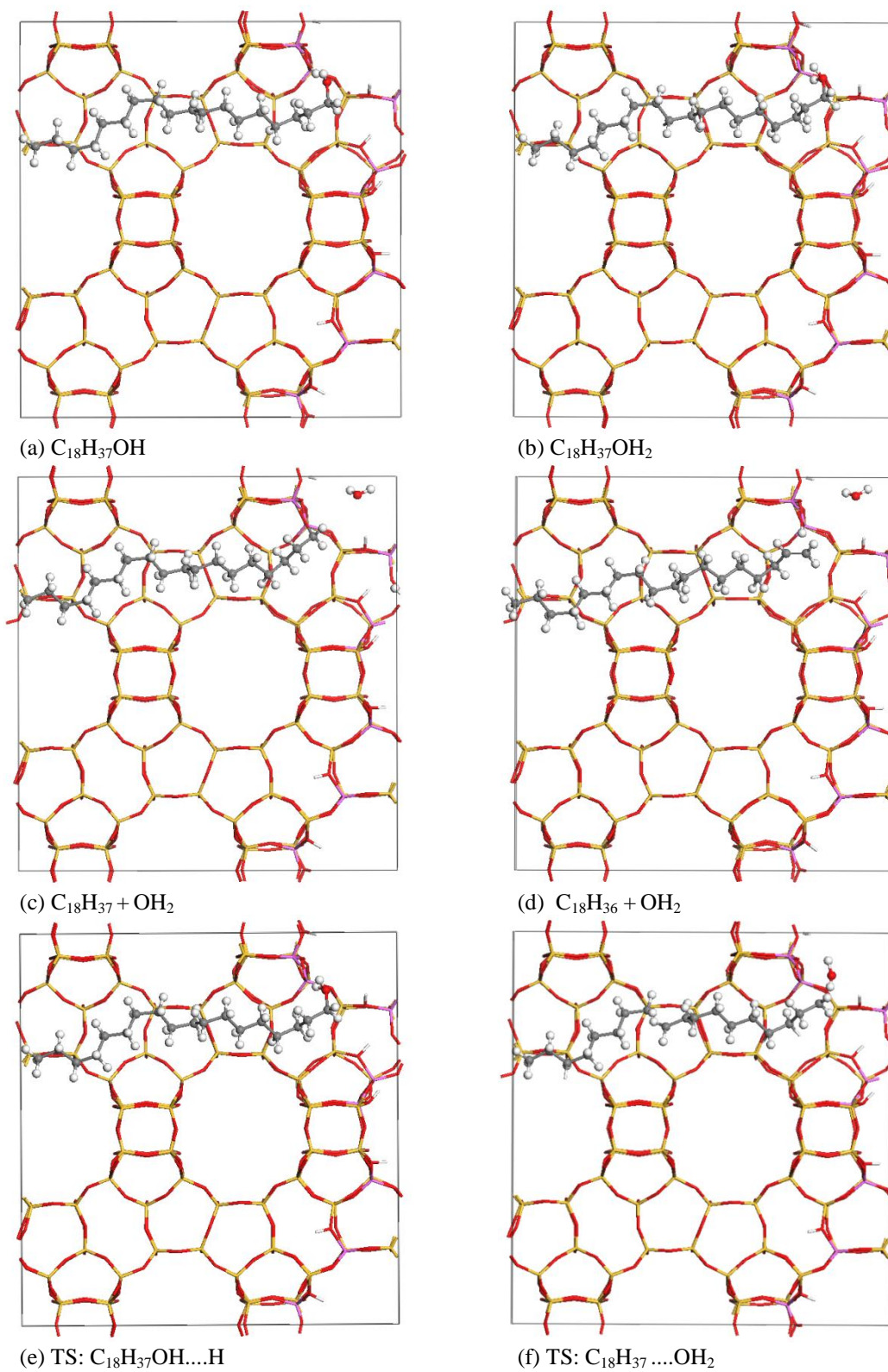(f) TS: $C_{18}H_{37} ....OH_2$

Figure 3-6. Optimized structures of C_{18} alcohol dehydration inside the
H-BEA (Si/Al=15) pore.

To account for the important role of entropy in the zeolite pores, the Gibbs free energy profile of 1-octadecanol to octadecene on BAS at 533 K was calculated (Figure 3-7). It is apparent that the Gibbs free energy profile is similar to the enthalpy profile (Figure 3-5). While the transition state of the rate determined step is entropically stabilized (ΔS=23 J·mol^{-1}·K^{-1}), the apparent Gibbs free energy activation barrier for intra-molecular dehydration in the H-BEA pore is lowered to 142 kJ·mol^{-1}.
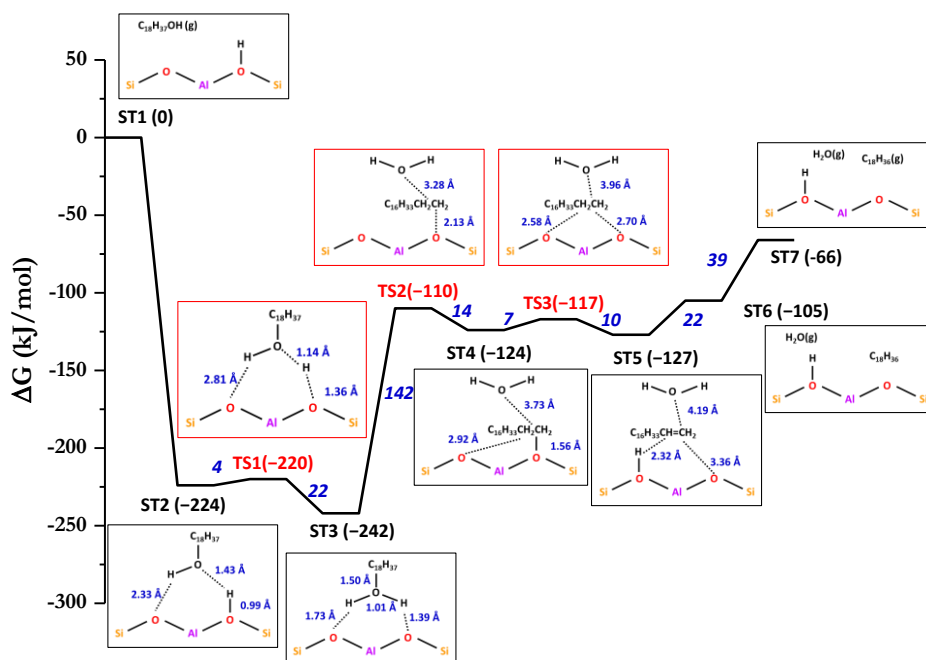

Figure 3-7. DFT calculated Gibbs free energy profile of dehydration of 1-octadecanol over BAS of H-BEA (Si/Al=15).

We also investigated the intramolecular dehydration at the pore-mouth BAS. As shown in Figure 3-8, the general trend for the intramolecular dehydration in- and at the pore mouths is very similar. Note that compared the strong adsorption of 1-octadecanol at the internal BAS site, the adsorption of 1-octadecanol is much weaker at the pore-mouth BAS, so coverage effects may influence the relative contributions of sites for catalysis. However, the intramolecular dehydration leading to octadecene seems to be overall independent of the location of acid sites. The apparent energy barriers for the rate-limiting step, i.e., surface octadecoxide formation, inside and outside zeolite pores are very close, with 161 kJ·mol^{-1} for inside BAS and 149 kJ·mol^{-1} for the pore-mouth BAS,

which are in reasonable agreement with our measured barrier of 166 kJ·mol⁻¹.
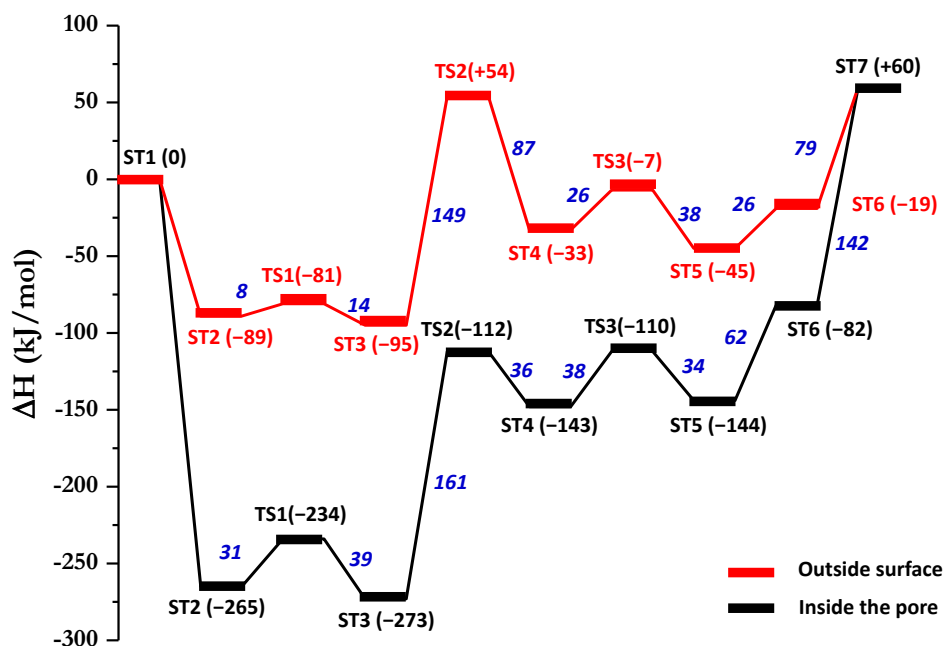

Figure 3-8. Comparison of 1-octadecanol dehydration over BAS inside and outside the H-BEA (Si/Al=15).

In comparison, the intermolecular dehydration of 1-octadecanol to dioctadecyl ether has a lower apparent activation energy. A previous DFT study[39] for the conversion of methanol to dimethyl ether (DEE) suggested that the dehydration mechanism involving dimer formation would lower the activation barrier of 70 kJ·mol⁻¹ comparing to the mechanism involving a surface methoxide. In the dimer involved mechanism shown in Scheme 3-1b, after the first 1-octadecanol molecule is adsorbed on a BAS site (step 1 in Scheme 3-1b), it interacts with another physisorbed 1-octadecanol molecule to form a dimer (step 2 in Scheme 3-1b) instead of decomposing into a surface-bound octadecoxide intermediate. The final step involves the formation of dioctadecyl ether and water via simultaneous C-O and C-H bond scission of the adsorbed dimer (step 3 in Scheme 3-1b).
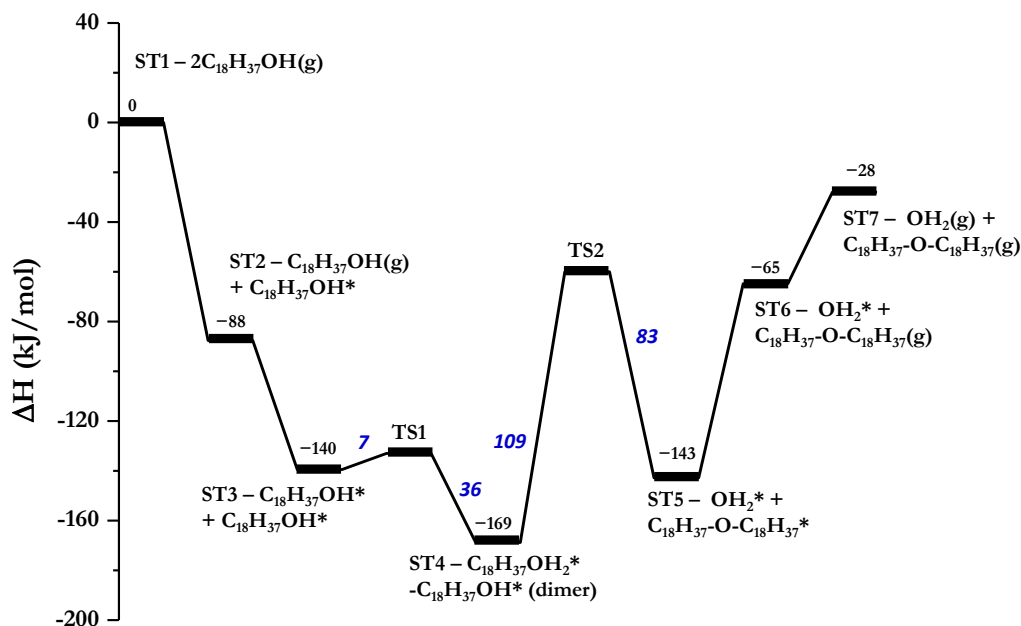
Figure 3-9. Dioctadecyl ether formation over external BAS of the H-BEA (Si/Al=15) zeolite.

Figure 3-9 shows the DFT calculated energy profile for the intermolecular dehydration of 1-octadecanol on BAS at the pore mouth of H-BEA. The formation of the dimer complex is thermodynamically favorable and kinetically facile. Once the two adsorbed 1-octadecanol molecules forms the dimer complex (ST4) shown in Figure 3-10, it will proceed through a SN2 mechanism, in which both C-O and O-H bonds are simultaneously cleaved forming dioctadecyl ether. The calculated activation barrier is 106 kJ·mol^{-1}, which is modestly higher than the measured activation barrier of 92 kJ·mol^{-1}. Note that the lower apparent is the result of a near first order dependence in 1-octadecanol for ether formation (Figure 3A-3). This lowers the true energy barrier by a relative low heat of adsorption of 1-octadecanol at the outer surface of the zeolite.
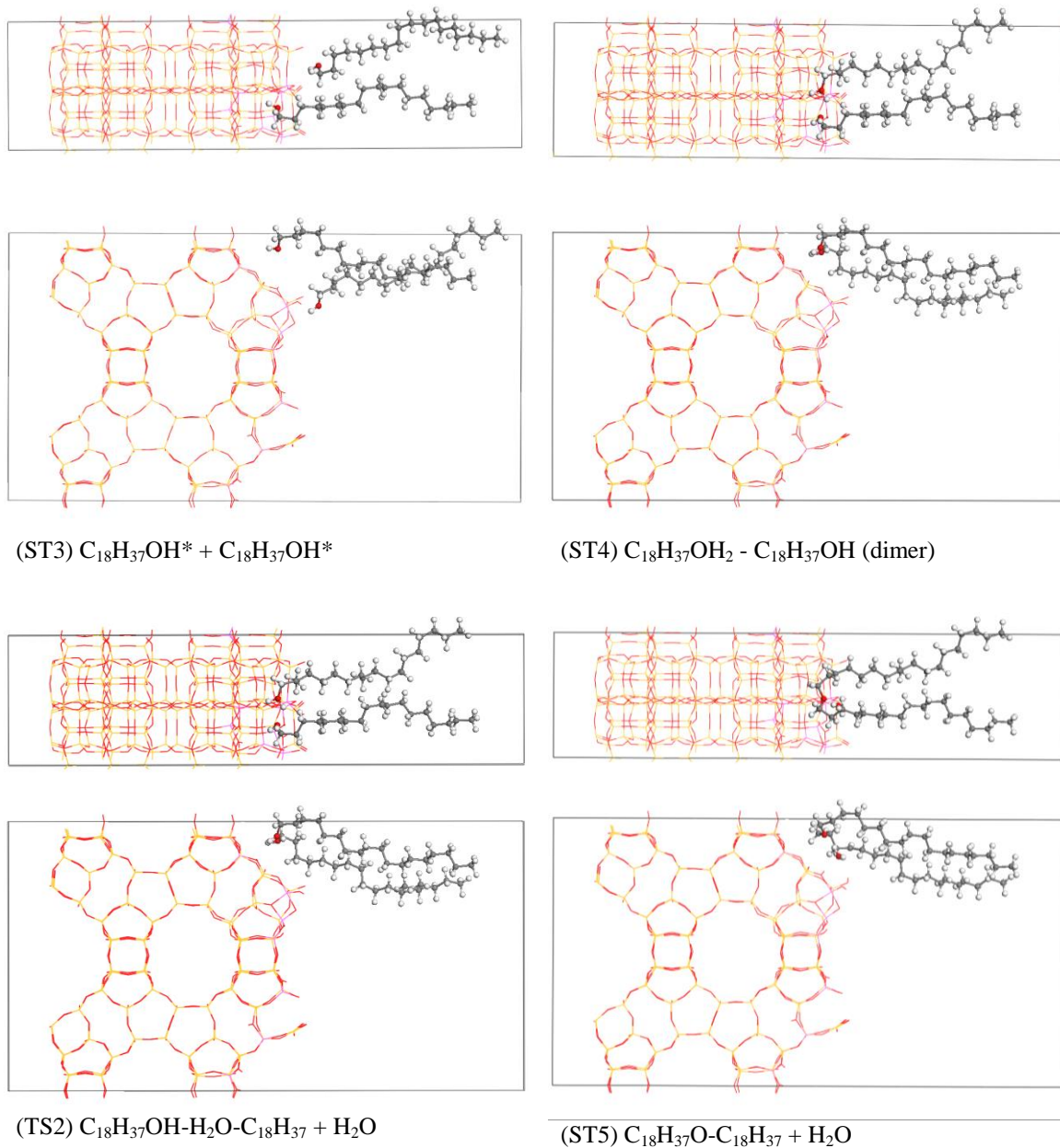
(ST3) $C_{18}H_{37}OH^* + C_{18}H_{37}OH^*$

(ST4) $C_{18}H_{37}OH_2 - C_{18}H_{37}OH$ (dimer)

(TS2) $C_{18}H_{37}OH-H_2O-C_{18}H_{37} + H_2O$

(ST5) $C_{18}H_{37}O-C_{18}H_{37} + H_2O$

Figure 3-10. Optimized structures of 1-octadecanol dehydration at the BAS at the pore-mouth area of the H-BEA (Si/Al=15) zeolite.

While the intramolecular dehydration requires lower activation energy barrier, it can only occur at the pore mouth area of H-BEA surface, because it requires a large transition state to accommodate both alcohols. The proposed dimer intermediate (Scheme 3-1b) is concluded to be too large to be accommodated in the 12-membered ring channel of the H-BEA zeolite. Hence, intermolecular dehydration leading to dioctadecyl ether could

only be related to the external acidity, i.e., BAS at the pore mouth or possibly Lewis acid sites at external surface of the zeolite crystals.

In agreement with the differences in the apparent activation energies, the intermolecular dehydration pathway was more pronounced at low reaction temperatures (Figure 3-4). It should be also noted that at higher temperatures the ether formed initially was converted to octadecene at longer reaction time. This indicates that the ether C-O bond was readily cleaved, presumably on BAS. This reaction sequence was more clearly observed at higher catalyst/reactant ratios (Figure 3-12c).

In conclusion, intramolecular dehydration of 1-octadecanol towards octadecene involves the formation of surface-alkoxide intermediates, which have a higher energy barrier in comparison to the pathway involving a dimer for intermolecular dehydration forming dioctadecyl ether. The latter, however, poses more stringent spatial restrictions, and, hence, is concluded to take place mainly on Brønsted acid sites at the pore mouth of H-BEA. Octadecene formation, on the other hand, is less dependent on the locations of BAS. The intramolecular dehydration is the major pathway observed at higher reaction temperature, *e.g.*, 533K. Alkenes are formed either directly from intramolecular dehydration or by sequential reactions via cleavage of the intermediate dioctadecyl ether.

3.3.3.   1-Octadecanol dehydration over poisoned zeolites

In order to understand the individual role of BAS and LAS, parent H-BEA-75 zeolite was modified by adsorption of quinoline and its derivatives with varying molecular dimensions and proton affinities. The DFT optimized molecular structures of adsorbed quinoline (Q), 4-methylquinoline (MQ), 2,4-dimethylquinoline (DMQ) and benzoquinoline (BQ) over the BAS site are shown in Figure 3A-4. After poisoning, the micropore volumes of the parent H-BEA decreased, indicating that all the four poisons have entered and occupied a sizable portion of the zeolite pores (Table 3A-3).

The IR spectra of the parent and modified zeolites at the hydroxyl group (–OH) stretching region are presented in Figure 3-11. Two pronounced bands were observed at 3735 and 3606 cm^{-1} in the spectrum of parent H-BEA, attributed to internal silanol and bridging hydroxyl groups respectively.[40] After the modification by quinoline and its

derivatives, the band characteristic of the SiOHAl groups disappeared, suggesting the poisons quantitatively interacted with all BAS. The intensity of the SiOH band decreased to some extent after base adsorption, accompanied by the appearance of a broad band at 3650 cm^{-1}, attributed to hydrogen bonding of the base to silanol groups.
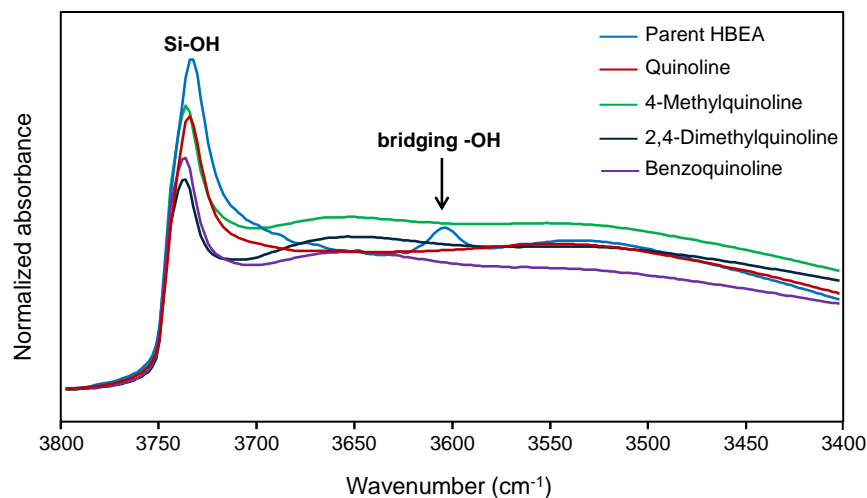

Figure 3-11. IR spectra at the hydroxyl region of the parent and poisoned H-BEA (Si/Al=75) with quinoline and its derivatives.

When using these poisoned zeolites for 1-octadecanol dehydration, the catalyzed rates of conversion were significantly lower than with the parent material (Figure 3-12a). Among the poisons explored, benzoquinoline treated sample preserved the highest dehydration activity. In detail, the intramolecular dehydration activity forming octadecene, which was the predominant pathway over the parent H-BEA (yielding over 90 C% after two hours), was largely suppressed on poisoned zeolites (Figure 3-12b). This was attributed to the marked decrease of BAS as evidenced by the IR spectra of the modified samples (Figure 3-11). On the other hand, the activity for the intermolecular dehydration to ether was largely retained (Figure 3-12c). The benzoquinoline-poisoned sample showed the highest activity for ether formation, reaching a yield of over 10 C% after two hours reaction. In contrast to the parent H-BEA, further conversion of dioctadecyl ether was not observed in all poisoned samples under the reaction conditions explored (Figure 3-12c), which is attributed to the blockage of Brønsted acid sites.
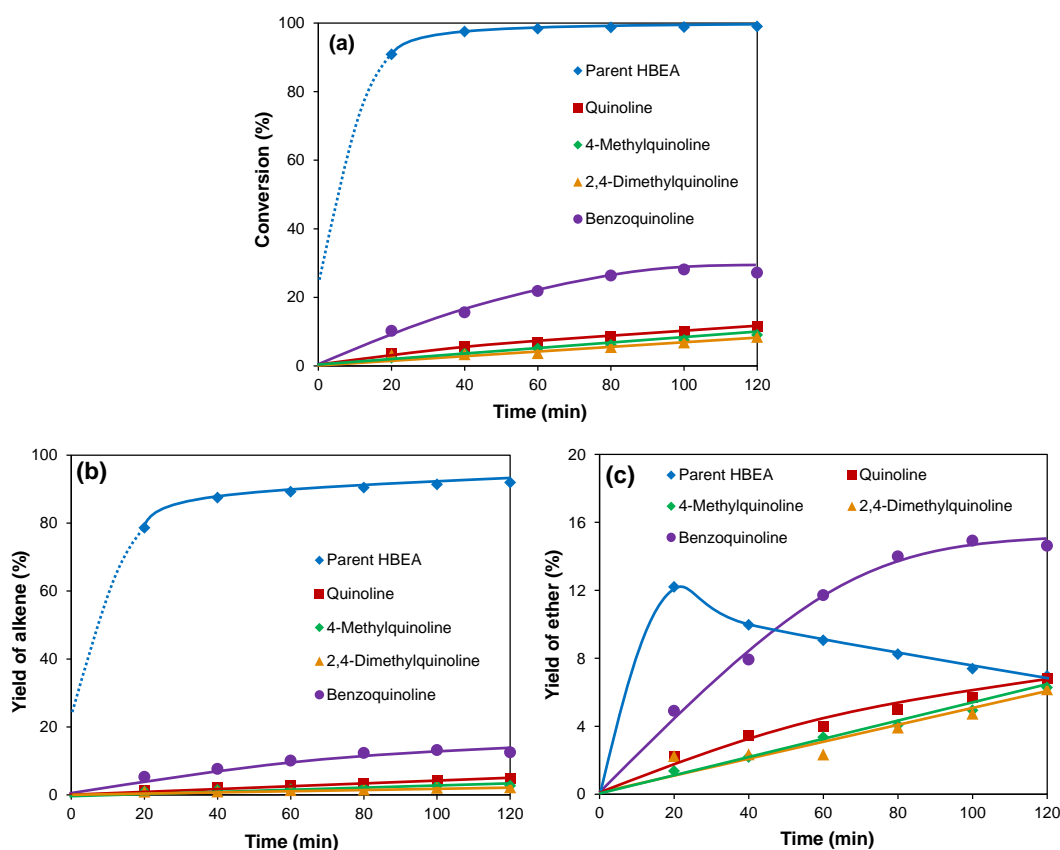
Figure 3-12. Dehydration of 1-octadecanol over parent and poisoned H-BEA (Si/Al=75);

(a) conversion, (b) yield of alkene, (c) yield of ether as a function of reaction time.

(b) Reaction conditions: 5g C18-OH, 0.05g H-BEA, 100mL dodecane, at 533 K,

(c) 10 bar N_2 (ambient temperature), stirring at 680 rpm.

To understand the residual dehydration activities of the modified zeolites, their residual acidities were probed by pyridine. Quinoline and its derivatives blocked all BAS irreversibly, which was also confirmed by DFT calculations. As shown in Table 3-3, the protonation of the four poison molecules are highly exothermic (−144 ∼ −193 kJ·mol^{-1}) and their reaction enthalpy is much higher than that of 1-octadecanol. This implies that in the presence of poison molecules, 1-octadecanol cannot access BAS.

Table 3-3. DFT calculated proton affinity ($A + H^+ \rightarrow AH^+$) of 1-octadecanol, quinoline and its derivatives in H-BEA (Si/Al=15).

Molecules	Vacuum (kJ·mol^{-1})	H-BEA (kJ·mol^{-1})
1-octadecanol	1241	-10
Quinoline	1003	-187
4-Methylquinoline	1020	-193
2,4-Dimethylquinoline	1038	-147
Benzoquinoline	1022	-144

On the other hand, a small concentration of LAS bound pyridine was detected. This corresponds to low concentrations of Lewis acid sites in the poisoned samples, which appeared to be proportional to their residual dehydration activities (Table 3-4). Indeed, if plotting the initial rates of 1-octadecanol dehydration against the remaining Lewis acidity probed, almost linear correlations were obtained for inter- and intra-molecular dehydration (Figure 3A-5).

Table 3-4. DFT calculated proton affinity ($A + H^+ \rightarrow AH^+$) of 1-octadecanol, quinoline and its derivatives in H-BEA (Si/Al=15).

H-BEA (Si/Al=75)	Lewis acid sites (μmol·g^{-1})	Rate of alkene formation (mmol g^{-1}·h^{-1})	Rate of ether formation (mmol g^{-1}·h^{-1})
Quinoline	5.1	7.8	25
4-Methylquinoline	2.8	3.6	15
2,4-Dimethylquinoline	2.5	2.4	11
Benzoquinoline	8.4	26	54

To further To further understand the dehydration activity over LAS sites, a separate kinetic test using commercial γ-Al$_2$O$_3$ was performed. The γ-Al$_2$O$_3$ was active for the dehydration of 1-octadecanol in liquid phase (Figure 3A-6). Similar to the poisoned zeolites, γ-Al$_2$O$_3$ mainly catalyzed ether formation, reaching a yield of above 10 C% after

two hours. The intramolecular dehydration activity to C_{18} alkene was much lower under selected reaction conditions (533 K). The fact that LAS is catalytically active for ether formation is not surprising. It has been reported that dehydration of alcohols toward the corresponding ether readily occurs over oxide catalysts, particularly Al_2O_3,[41,42] whereas the intramolecular pathway producing alkene requires a higher activation energy.[43] Therefore, with γ-Al_2O_3 as catalyst, ether is generally considered as the kinetically favored product at low reaction temperatures especially below 533 K, at which intermolecular dehydration is observed to be the sole pathway.[43,44] In the present case, the acidity of the remaining LAS probed by pyridine would be strong enough to catalyze intermolecular dehydration. The possible reaction pathway is simulated by AIMD calculations (see details in Appendix).

Therefore, we conclude that Brønsted acid sites at the pore mouth are the main active sites for 1-octadecanol dehydration. The kinetic data from poisoned zeolites suggest that having the BAS blocked, intermolecular dehydration forming dioctadecyl ether is hypothesized to take place over the remaining weak LAS at the external surface of zeolites. It is assumed that in the absence of poisons, the intramolecular pathway dominates on BAS at pore mouths, due to the high reactivity of the alkoxonium ion.

3.4. Conclusions

1-octdecanol dehydration on H-BEA has been studied with combined experimental and computational methods as an example for the elimination reactions of long-chain alcohols. The nature and stabilities of surface intermediates in parallel dehydration pathways are discussed, and the impacts of the locations of Brønsted and Lewis acidic sites are emphasized. The high reactivity of H-BEA and the strong interactions of the long alkyl chain with the pores of the zeolite caused inefficient utilization of BAS in samples with high concentrations of acid sites.

A dimer involved mechanism is proposed for dioctadecyl ether formation in which a lower apparent activation energy is required compared to intramolecular dehydration (producing octadecene) which proceeds via surface-bound alkoxide species. DFT calculations suggest the energy barriers for the rate-limiting step of alkene formation to

be nearly independent of the acid site locations. At 533 K, octadecene was the primary dehydration product on parent H-BEA, with dioctadecyl ether also being further converted to the alkene. The sterically demanding formation of dioctadecyl ether is concluded to take place mainly on BAS and LAS at the pore mouth or the external surface, respectively, because the bulky dimer intermediate proposed is restricted from the 12-membered ring channel of H-BEA.

Poisoning experiments with quinoline (and derivatives) show that despite of the main contribution of BAS towards dehydration, weak LAS suffice to catalyze the intermolecular dehydration of 1-octdecanol, while intramolecular dehydration to octadecene and cleavage of dioctadecyl ether require the function of stronger BAS.
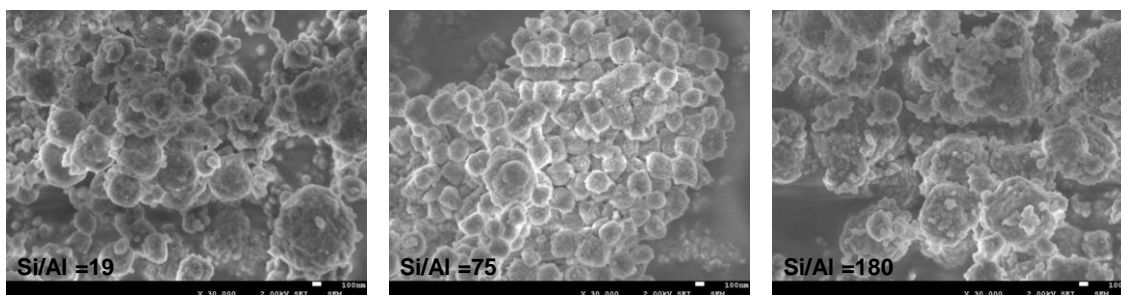
3.5. Acknowledgments

3.6. Appendix

Figure 3A-1. SEM images of H-BEAs with varied Si/Al ratios.

Table 3A-1. Physicochemical properties of H-BEAs with varied Si/Al ratios.

Si/Al ratio	BET surface area ($m^2 \cdot g^{-1}$)			Pore volume ($cm^3 \cdot g^{-1}$)		
	Micro	Meso	Total	Micro	Meso	Total
19	492	139	631	0.22	0.15	0.37
75	502	122	624	0.20	0.17	0.37
180	382	168	550	0.16	0.21	0.37

(a) Diffusion of 1-octadecanol inside the pore of HBEA-15

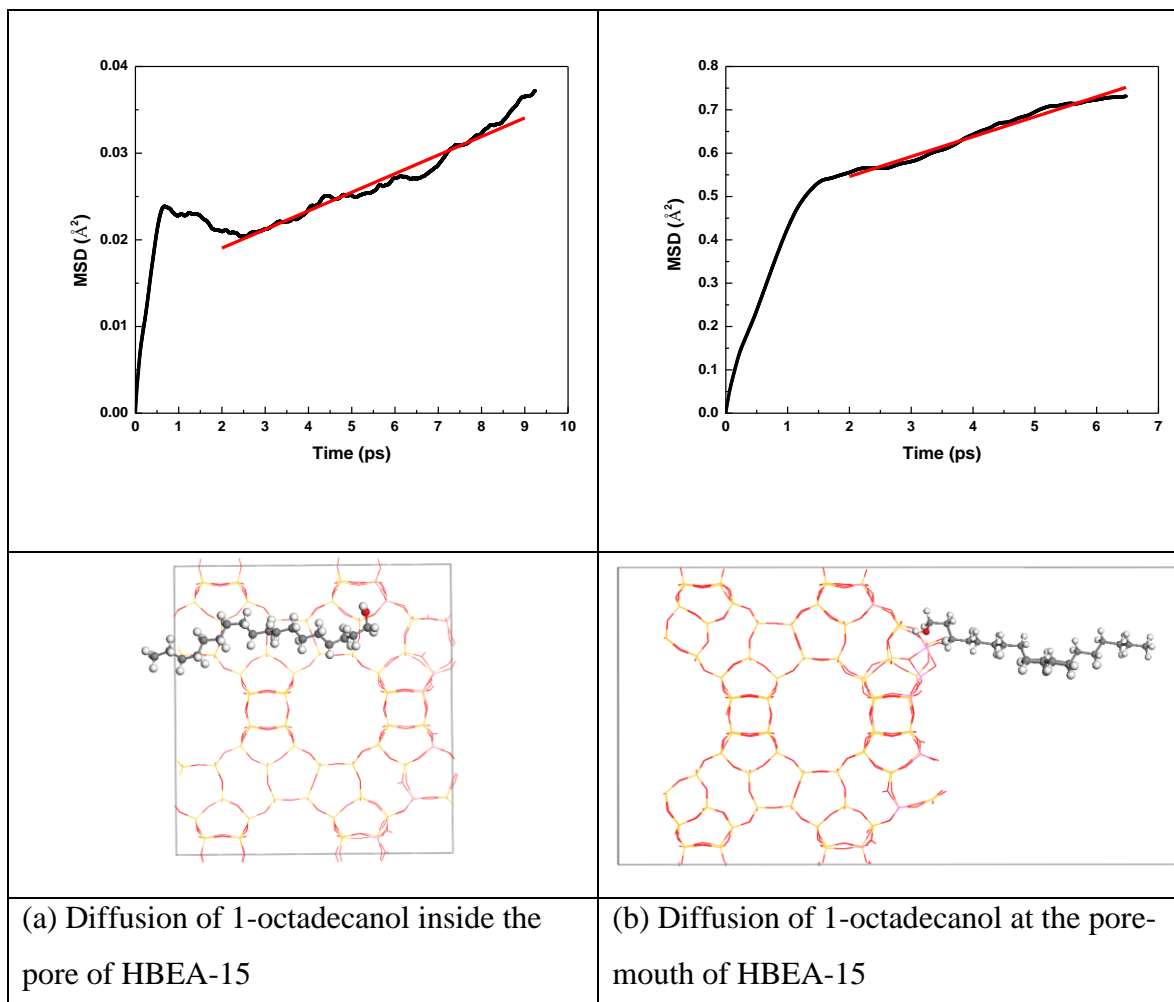(b) Diffusion of 1-octadecanol at the pore-mouth of HBEA-15

Figure 3A-2. Diffusion of 1-octadecanol inside and at the pore mouth.

Estimation of catalyst efficiency for intramolecular dehydration of 1-octadecanol

$$r = k_s \times S_v \times c^n$$

$$\Phi = R \times \sqrt{\frac{k_s \times S_v \times c^{n-1}}{D_e}}$$

$$\eta = \frac{3}{\Phi^2} \times (\Phi \coth \Phi - 1)$$

where the reaction order *n* with respect to 1-octadecanol for alkene formation was measured to be 0;

the average crystal size determined from XRD diffraction pattern for H-BEA with Si/Al=19, 75, 180 were 34, 18 and 11 nm respectively;

An estimation of diffusion coefficient obtained from theoretical calculation was $D = 2.2 \times 10^{-12}\ m^2/s$, and the effective diffusion coefficient $D_e \approx \frac{D}{10} = 2.2 \times 10^{-13}\ m^2/s$;

The values of Thiele modulus as well as catalyst efficiency for the three H-BEA samples are compiled in Table S2.

Table 3A-2. Thiele modulus and catalyst efficiency of H-BEAs with varied Si/Al ratios.

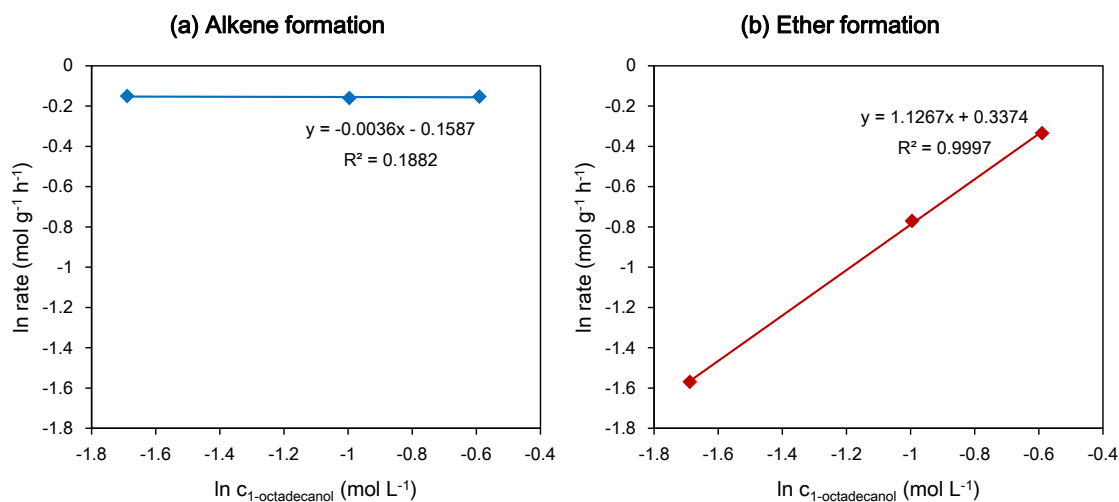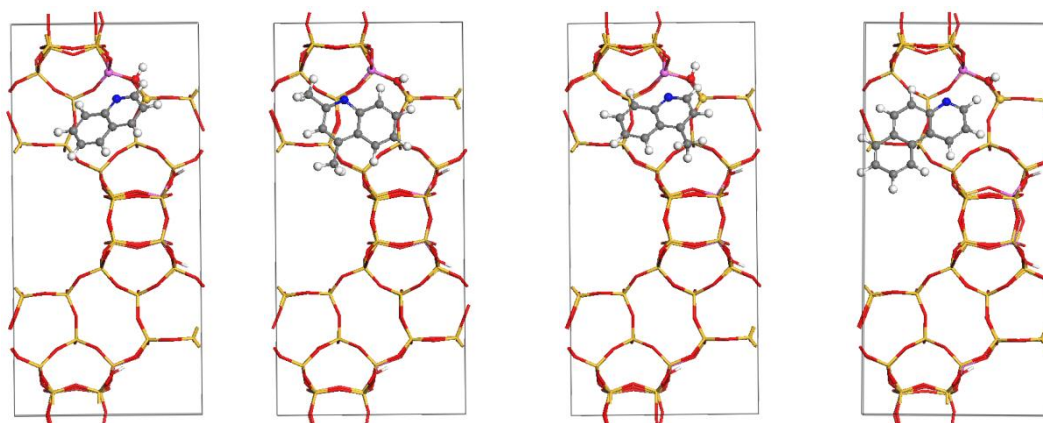| Si/Al ratio	Φ	η
19	5.75	0.43
75	2.51	0.74
180	1.07	0.93

Figure 3A-3. Reaction order with respect to 1-octadecanol for (a) intramolecular and (b) intermolecular dehydration pathways over H-BEA (Si/Al=75). Reaction conditions: 0.025g H-BEA, 100mL dodecane, 10 bar N2 (ambient temperature), stirring at 680 rpm.

| Quinoline | 4-Methylquinoline | 2,4-Dimethylquinoline | Benzoquinoline |

E_{ad} = -25 kJ·mol^{-1} E_{ad} = -36 kJ·mol^{-1} E_{ad} = -25 kJ·mol^{-1} E_{ad} = -67 kJ·mol^{-1}

Figure 3A-4. The optimized structures of adsorbed quinoline and its derivatives inside H-BEA (Si/Al=15) zeolite.

Table 3A-3. Physicochemical properties of parent and poisoned H-BEA (Si/Al=75) with quinoline and its derivatives.[a]

H-BEA (Si/Al=75)	BET surface area (m^2·g^{-1})			Pore volume (cm^3·g^{-1})		
	Micro	Meso	Total	Micro	Meso	Total
Parent	469	188	657	0.17	0.10	0.27
Quinoline	347	211	558	0.13	0.10	0.23
4-Methylquinoline	313	184	497	0.12	0.11	0.23
2,4-Dimethylquinoline	270	194	464	0.10	0.13	0.23
Benzoquinoline	285	208	493	0.10	0.13	0.23

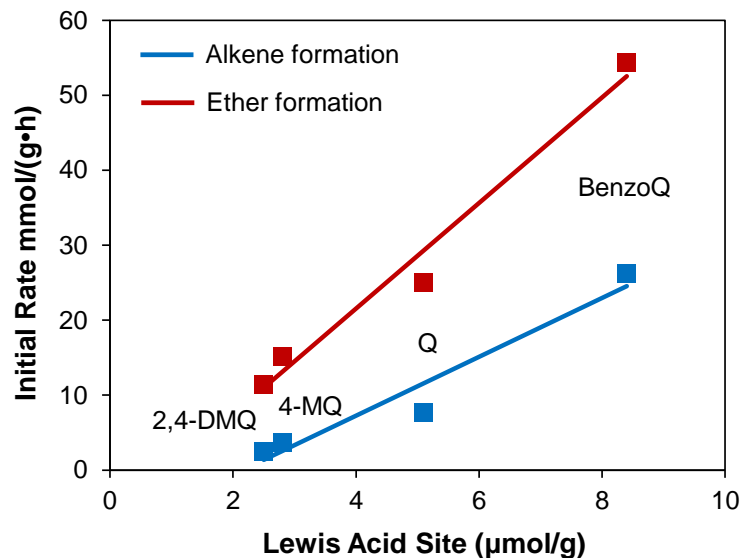[a] samples were activated at 473 K before measurements.

Figure 3A-5. Relation of residual activities with concentrations of remaining Lewis acid sites in the poisoned H-BEA zeolites.

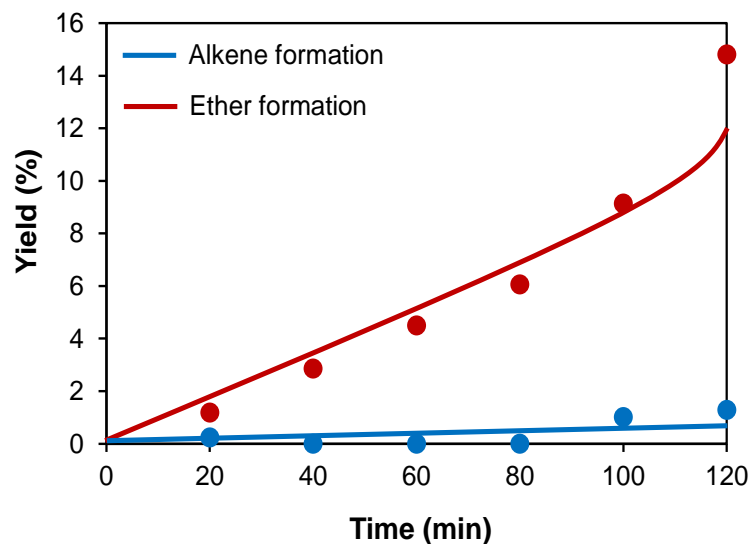**Figure 3A-6.** Dehydration of 1-octadecanol over commercial γ–Al_2O_3 as a function of reaction time. Reaction conditions: 5g C_{18}-OH, 0.05g γ–Al_2O_3, 100mL dodecane, at 533 K, 10 bar N_2 (ambient temperature), stirring at 680 rpm.

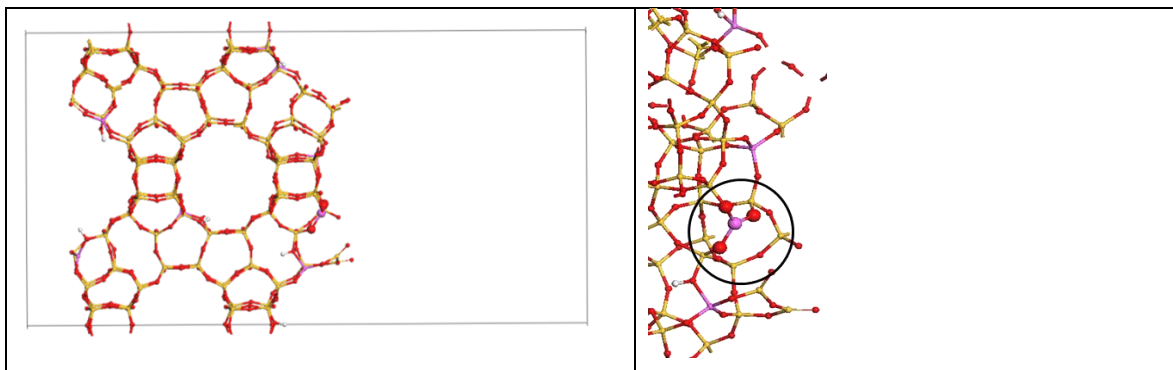**AIMD simulations of inter-molecular dehydration of 1-octadecanol over LAS**

Figure 3A-7. The HBEA zeolite simulation system with external surface containing LAS represented by Si-O-Al^{3+}-O-Si.

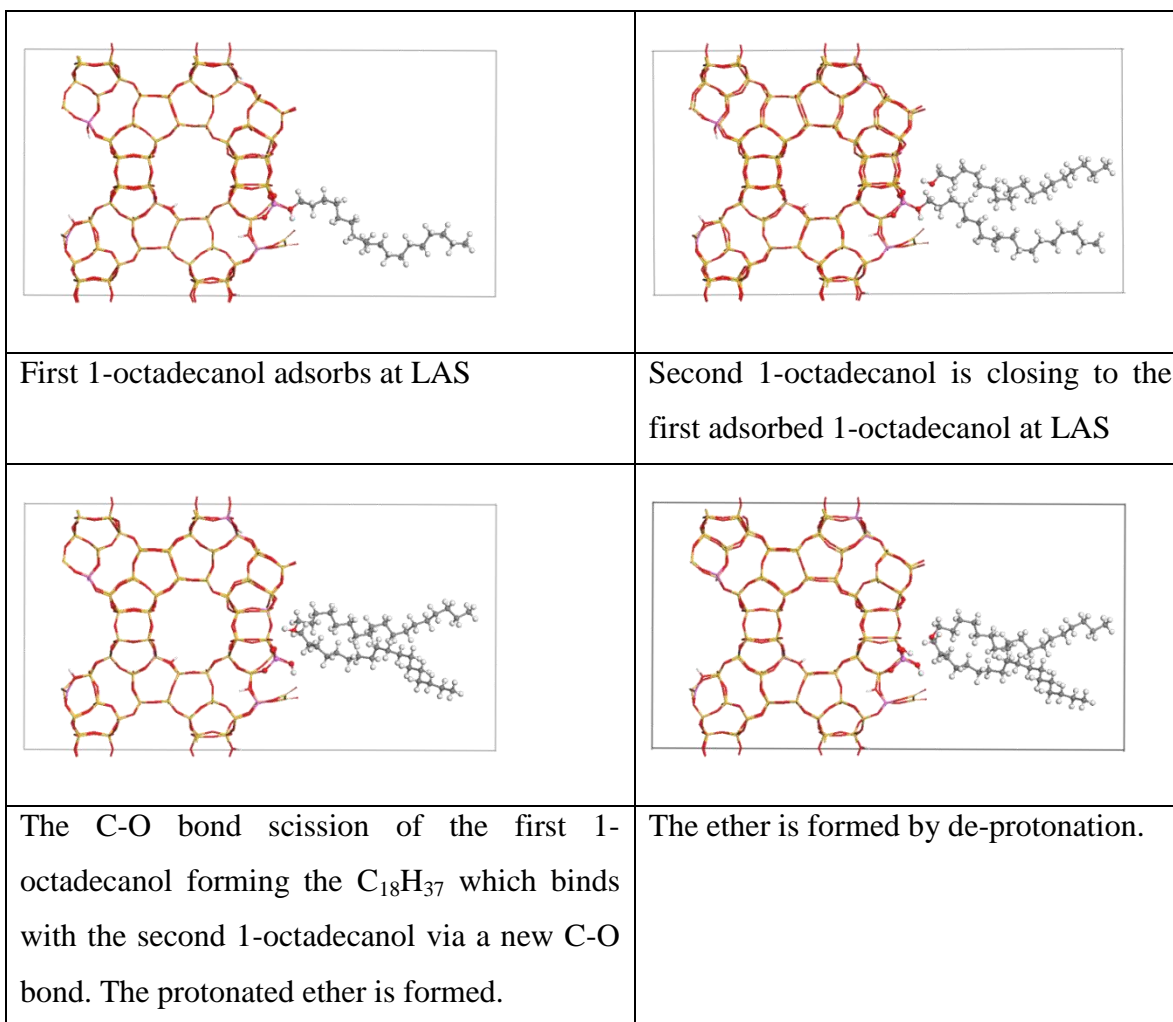|	
First 1-octadecanol adsorbs at LAS	Second 1-octadecanol is closing to the first adsorbed 1-octadecanol at LAS
The C-O bond scission of the first 1-octadecanol forming the C$_{18}$H$_{37}$ which binds with the second 1-octadecanol via a new C-O bond. The protonated ether is formed.	The ether is formed by de-protonation.

Figure 3A-8. Dioctadecyl ether formation over external LAS of HBEA-15 zeolite.

3.7. References

[1] U.R. Kreutzer, J. Am. Oil Chem. Soc. 1984, 61, 343.

[2] K. Noweck, W. Grafahrend, Fatty Alcohols. in *Ullmann's Encyclopedia of Industrial Chemistry,* Wiley-VCH, Weinheim, Germany, **2012,** Vol. 14, p. 117-141.

[3] W. Song, C. Zhao, J. A. Lercher, *Chem. Eur. J.* **2013,** *19,* 9833.

[4] B. Peng, Y. Yao, C. Zhao, J. A. Lercher, *Angew. Chem. Int. Ed.* **2012,** *51,* 2072.

[5] H. Knözinger, The dehydration of alcohols. in *The Chemistry of The Hydroxyl Group* (Ed.: Patai, S.), Wiley-Interscience, London, New York, Sydney, Toronto, **1971,** Chapter 12, pp 642-718 and references therein.

[6] T. Kito-Borsa, S. W. Cowley, *Prepr. Pap.-Am. Chem. Soc., Div. Fuel Chem.* **2004,** *49(2),* 856-859 and reference therein.

[7] C. Park, M. A. Keane, *J. Mol. Catal. A: Chem.* **2001,** *166,* 303-322 and references therein.

[8] M. M. J. Treacy, J. M. Newsam, *Nature* **1988,** *332,* 249.

[9] J. B. Higgins, R. B. LaPierre, J. L. Schlenker, A. C. Rohrman, J. .D. Wood, G. T. Kerr, W. J. Rohrbaugh, *Zeolites* **1988,** *8,* 446.

[10] C. Tuma, T. Kerber, J. Sauer, *Angew. Chem. Int. Ed.* **2010,** *49,* 4678.

[11] R. A. Vansanten, G. J. Kramer, *Chemical Reviews* **1995,** *95,* 637.

[12] S. Svelle, C. Tuma, X. Rozanska, T. Kerber, J. Sauer, *J. Am. Chem. Soc.* **2009,** *131,* 816.

[13] S. R. Blaszkowski, R. A. vanSanten, *J. Am. Chem. Soc.* **1996,** *118,* 5152.

[14] J. Macht, R. T. Carr, E. Iglesia, *J. Am. Chem. Soc.* **2009,** *131,* 6554.

[15] S. Svelle, F. Joensen, J. Nerlov, U. Olsbye, K.-P. Lillerud, S. Kolboe, M. Bjorgen, *J. Am. Chem. Soc.* **2006,** *128,* 14770.

[16] V. Van Speybroeck, J. Van der Mynsbrugge, M. Vandichel, K. Hemelsoet, D. Lesthaeghe, A. Ghysels, G. B. Marin, M. Waroquier, *J. Am. Chem. Soc.* **2011,** *133,* 888.

[17] P. A. Zapata, J. Faria, M. P. Ruiz, R. E. Jentoft, D. E. Resasco, *J. Am. Chem. Soc.* **2012,** *134,* 8570.

[18] A. Vjunov, M. Y. Hu, J. Feng, D. M. Camaioni, D. Mei, J. Z. Hu, C. Zhao, J. A. Lercher, *Angew. Chem. Int. Ed.* **2014,** *53,* 479.

[19] A. Vjunov, J. L. Fulton, T. Huthwelker, S. Pin, D. Mei, G. K. Schenter, N. Govind, D. M. Camaioni, J. Z. Hu, J. A. Lercher, *J. Am. Chem. Soc.* **2014,** *136,* 8296.

[20] G. Lippert, J. Hutter, M. Parrinello, *Mol. Phys.* **1997,** *92*, 477.

[21] J. VandeVondele, M. Krack, F. Mohamed, M. Parrinello, T. Chassaing, J. Hutter, *Comput. Phys. Commun.* **2005,** *167*, 103.

[22] J. M. Newsam, M. M. J. Treacy, W. T. Koetsier, C. B. Degruyter, *Proceedings of the Royal Society of London Series a-Mathematical Physical and Engineering Sciences* **1988,** *420.*

[23] S. Grimme, J. Antony, S. Ehrlich, H. Krieg, *J. Chem. Phys.* **2010,** *132*, 154104.

[24] G. Henkelman, B. P. Uberuaga, H. Jonsson, *J. Chem. Phys.* **2000,** *113*, 9901.

[25] G. Mills, H. Jonsson, G. K. Schenter, *Surf. Sci.* **1995,** *324*, 305.

[26] A. Bhan, R. Gounder, J. Macht, E. Iglesia, *J. Catal.* **2008,** *253*, 221.

[27] R. Gounder, E. Iglesia, *J. Am. Chem. Soc.* **2009,** *131*, 1958.

[28] R. Gounder, E. Iglesia, *Acc. Chem. Res.* **2012,** *45*, 229.

[29] A. J. Jones, E. Iglesia, *Angew. Chem. Int. Ed.* **2014,** *53*, 12177.

[30] A. J. Jones, S. I. Zones, E. Iglesia, *J. Phys. Chem. C* **2014,** *118*, 17787.

[31] G. Psofogiannakis, A. St-Amant, M. Ternan, *J. Phys. Chem. B* **2006,** *110*, 24593.

[32] A. Corma, V. Fornés, L. Forni, F. Márquez, J. Martíınez-Triguero, D. Moscotti, *J. Catal.* **1998,** *179,* 451.

[33] J. A. Lercher, C. Gründling, G. Eder-Mirth, *Catal. Today* **1996,** *27,* 353.

[34] A. L. García-Ponce, L. Moreno-Real, A. Jiménez López, *J. Solid State Chem* **1990,** *87,* 20.

[35] S. Mintova, V. Valtchev, T. Onfroy, C. Marichal, H. Knözinger, T. Bein, *Micropor. Mesopor. Mater.* **2006,** *90,* 237.

[36] C. P. Bezoukhanova, Y.A. Kalvachev, *Cat. Rev. - Sci. Eng.* **1994,** *36,* 125.

[37] W. K. Hall, B.E. Spiewak, R. D. Cortright, J. A. Dumesic, H. Knözinger, H. Pfeifer, V. B. Kazansky, and G.C. Bond. Characterization of Solid Catalysts. in *Handbook of Heterogeneous Catalysis* (Eds.: G. Ertl, H. Knözinger, J. Weitkamp), Wiley-VCH, Weinheim, Germany, **1997,** Vol. 2, Chapter 3, pp. 427-770.

[38] J. N. Kondo, K. Ito, E. Yoda, F. Wakabayashi, K. Domen, *J. Phys. Chem. B* **2005,** *109,* 10969.

[39] S. R. Blaszkowski, R. A. van Santen, *J. Am. Chem. Soc.* **1996,** *118,* 5152.

[40] V. V. Ordomsky, V. Y. Murzin, Y. V. Monakhova, Y. V. Zubavichus, E. E. Knyazeva, N. S. Nesterenko, I. I. Ivanova, *Micropor. Mesopor. Mater.* **2007,** *105,* 101.

[41] H. Pines, J. Manassen. *Adv. Catal.* **1966,** *16,* 49.

[42] H. Knozinger, *Angew. Chem., Int. Ed.* **1968,** *7,* 791.

[43] J.H. de Boer, R. B. Fahim, B. G. Linsen, W. J. Visseren, W. F. N. M. de Vleesschuwer, *J. Catal.* **1967,** *7,* 163.

[44] B. Shi, B. H. Davis, *J. Catal.* **1995,** *157,* 359.

Chapter 4

Synergistic Effects of Ni and Acid Sites for Hydrogenation and C–O Bond Cleavage of Substituted Phenols

The cleavage of C-O bonds in phenol, catechol, and guaiacol has been explored with mono- and dual- functional catalysts containing Ni and/or HZSM-5 in aqueous phase. The aromatic ring of phenol is hydrogenated in the first step, and the C−O bond of the resulting cyclohexanol is dehydrated in sequence. The initial turnover frequency (TOF) of phenol hydrodeoxygenation increases in parallel with the acid site concentration irrespective of the concentration of accessible surface Ni atoms. For catechol and guaiacol conversion, Ni catalyzes hydrogenolysis of the C−O bonds in addition to arene hydrogenation. For catechol, the hydrogenation of the aromatic ring and the hydrogenolysis of phenolic –OH group occur in parallel with a ratio of 8:1. The saturated cyclohexane-1,2-diol can be further dehydrated over HZSM-5 or hydrogenolyzed on Ni to complete hydrodeoxygenation. Guaiacol undergoes primarily hydrogenolysis (75%) to phenol via demethoxylation, and the hydrogenation route accounts for only 25%. This is attributed to the steric effects arising from the adjacent sp^3 hybrid O−CH$_3$ group. 2-Methoxycyclohexanol (from guaiacol hydrogenation) reacts further either via hydrogenolysis by Ni to cyclohexanol or via acid catalyzed demethoxylation and rearrangement steps followed by subsequent hydrogenation of the intermediately formed olefins. On Ni/HZSM-5, the hydrodeoxygenation activities are much higher for the phenolic monomers than for their respective saturated analogues, pointing to the importance of sp^2 orbitals. The presence of proximal acid sites increases the activities of Ni in the presence of H$_2$ by a synergistic action.

4.1. Introduction

Lignin is an abundant biopolymer composed of substituted C_9 propyl-phenol units, which are randomly cross-linked by C−C and C−O bonds.[1] Bio-oil derived from liquefaction or pyrolysis of lignin is seen as a promising source for second-generation bio-derived energy carriers.[2] However, the direct application of bio-oil is limited by its poor volatility, high viscosity, as well as its low stability caused by high contents of oxo-functionalized compounds.[3] In this context, hydrodeoxygenation (HDO) is considered as the most effective method for converting oxygen-rich lignin derived bio-oil to clean oxygen-free hydrocarbon fuels.[4]

Lignin derived bio-oil comprises of a wide variety of C_{aryl}−OH, C_{aryl}−OCH$_3$, and C_{alkyl}−OR as well as C=O bonds. Cleavage of the C=O double bond requires stepwise hydrogenation and dehydration, whereas the former three types of C−O single bonds can be directly cleaved by metal-catalyzed hydrogenolysis. Alternatively, acid sites also catalyze cleavage of C_{aryl}−OR and C_{alkyl}−OR bonds through hydrolysis. The formed C_{alkyl}−OH bond can be eliminated via dehydration. Removing oxygen in C_{aryl}−OH bond, however, involves cascade reactions of hydrogenation and dehydration. The bond dissociation energies of C_{aryl}−O bonds are around 80-100 kJ·mol^{-1} higher than those of C_{alkyl}−O bonds;[4,5] while on the other hand, the steric constraints of cleaving C_{alkyl}−O bonds are much higher than for C_{aryl}−O bonds. Thus, it is highly important to understand the integrated steps of hydrogenolysis, hydrogenation, hydrolysis, and dehydration, to efficiently cleave the various C-O bonds in phenol derivatives.

In the past, sulfide-based hydrotreating catalysts have been employed for the hydrodeoxygenation of functionalized phenols.[6] For instance, in the gas phase guaiacol was reported to be first converted via hydrogenolysis of the methoxy group to catechol and methane, followed by hydrogenolysis of the hydroxyl group of catechol to phenol, which in turn was deoxygenated by hydrogenolysis and hydrogenation forming benzene, cyclohexene, and cyclohexane.[7] Severe coke formation was observed during the conversion of both guaiacol and catechol with Al_2O_3 supported NiMo- or CoMo-sulfides.[7a, 8] By comparison, using dual functional catalysts with metal/acid sites such as Pd/C and H_3PO_4, guaiacol was primarily hydrogenated to 2-methoxycyclohexanol in the

aqueous phase, which was in turn hydrolyzed producing cyclohexane-1,2-diol followed by consecutive acid catalyzed dehydration and metal catalyzed hydrogenation leading to cyclohexane formation.[9] Carbonaceous deposits were negligible for such aqueous-phase catalytic process.

Recently, we have reported that Ni supported on zeolite HZSM-5 catalyzes quantitative hydrodeoxygenation of the *n*-hexane-soluble fraction of pyrolysis oil to C_5-C_9 hydrocarbons under mild conditions (523 K, 5 MPa H_2) in water.[10] In this contribution, the synergistic roles of metal and acid sites of Ni/HZSM-5 in aqueous phase are explored, including the integrated hydrogenation and hydrogenolysis over Ni sites, as well as dehydration and rearrangements with acid sites of HZSM-5. The kinetics of the conversions of phenolic monomers and of their respective saturated cyclic alcohols are described and discussed, in order to elucidate the difference of opening aliphatic and aromatic C−O bonds in phenols and alcohols. The positive influence of proximal acid sites on the Ni activities is also highlighted.

4.2. Experimental section

4.2.1. Chemicals

All chemicals were obtained from commercial suppliers and used as received. Phenol (Sigma–Aldrich, 99%), 1,2-hydroxylbenzene (Sigma–Aldrich, ≥ 99%), *cis*-cyclohexane-1,2-diol (Aldrich, 99%), 2-methoxyphenol (Sigma–Aldrich, oxidation indicator), (1S,2S)-(+)-2-methoxycyclohexanol (Alfa Aesar, 99%), ethyl acetate (Sigma–Aldrich, 99.9%), Ni(II) nitrate hexahydrate (Sigma–Aldrich, ≥ 98.5%), urea (Sigma–Aldrich, BioReagent). NH$_4$-ZSM-5 with framework Si/Al ratios of 11.5 and 25 were purchased from Zeolyst international, and HZSM-5 with Si/Al = 90 were obtained from Clariant. All three zeolites were calcined in air at 823 K for 6 h before usage.

4.2.2. Preparation and Ni/HZSM-5 catalysts

The deposition–precipitation (DP) method was applied to prepare the Ni based catalysts, according to procedures reported in the literature.[11] In a typical synthesis, 250 mL aqueous solution of $Ni(NO_3)_2$ (0.14 M) was prepared and divided into two parts. 210 mL of it was made suspension with 2 g parent HZSM-5 zeolite, and urea was dissolved in the rest 40 mL of the solution. The zeolite suspension was heated up to 343 K at which the urea solution was added dropwise, and then the mixture was brought up to 363 K to start the DP process. After 2 hours, the suspension was cooled to ambient temperature, vacuum filtered, and then the solid was washed three times with double distilled water. The obtained samples were dried at 383 K in air overnight. The catalyst precursors were calcined at 673 K for 4 h in air with a heating rate of 1 K·min^{-1} (flow rate: 100 mL·min^{-1}), and then reduced in pure hydrogen at 733 K for 5 h with a heating rate of 1 K·min^{-1} (hydrogen flow: 150 mL·min^{-1}). Preparation of Ni/SiO$_2$ catalyst followed similar procedures as described for Ni/HZSM-5, but with a DP duration of three hours.

4.2.3. Catalyst characterization

Elemental analysis of Ni contents in the catalyst samples were measured by atomic absorption spectroscopy (AAS) on a UNICAM 939 AA–Spectrometer. Prior to measurement, the sample was dissolved in a mixture of hydrofluoric acid (48%) and nitro-hydrochloric acid at its boiling point.

The BET specific surface area and pore volume were determined by N$_2$ adsorption–desorption isotherms measured at 77 K using a PMI automatic sorptometer. The catalyst was activated in vacuum at 473 K for 2 h before the measurements. The specific surface areas were calculated by applying the Brunauer-Emmett-Teller (BET) theory, and the *t*-plot method was used to determine the pore volumes.[12]

Temperature programmed desorption (TPD) of NH$_3$ was performed in a 6–fold parallel reactor system. About 50 mg of each catalyst was loaded into individual reactors and activated in He at 773 K for 1 h (heating rate: 5 K·min^{-1}). NH$_3$ was adsorbed with a partial pressure of 1 mbar at 373 K, and subsequently, the samples were purged with He

(30 mL·min^{-1}) for 2 h to remove physisorbed molecules. For the measurement of temperature programmed desorption, the catalyst samples were heated up in flowing He from 373 to 1033 K with a temperature increment of 10 K·min^{-1} to desorb ammonia. The desorbed species (m/z^+ = 16 signal) were monitored by mass spectrometry (Balzers QME 200). For acid sites quantification, a reference (HZSM-5, Si/Al = 45 from Clariant) with known acidity was used to calibrate the signal.

The infrared spectra of adsorbed pyridine (Py-IR) were recorded with a Thermo Nicolet 5700 spectrometer at a resolution of 4 cm^{-1}. The sample was prepared as a self–supporting wafer and activated in vacuum ($p = 10^{-7}$ mbar) at 723 K for 1 h (heating rate = 10 K·min^{-1}). After cooing to 423 K, the sample was equilibrated with 0.1 mbar of pyridine for 30 min, followed by outgassing for 1 h, and the IR spectra of chemisorbed pyridine were recorded subsequently. For quantification, molar integral extinction coefficients of 0.73 cm·µmol^{-1} and 0.96 cm·µmol^{-1} were used for the characteristic vibration bands of pyridinium ion and pyridine bound to Lewis acid sites, respectively.

Transmission electron microscopy (TEM) images were taken by a JEM–2010 Jeol transmission microscope operating at 120 kV. The catalyst sample was first suspended in ethanol by ultrasonication, and a drop of the suspension was deposited onto a carbon–coated Cu grid. More than 300 particles were counted to determine the average particle size.

The crystal structures of the catalyst powder were analyzed by X-ray diffraction (XRD) using a Philips X'Pert Pro System, with Cu-Kα radiation operating at 45 kV/40 mA. The sample was measured with a scanning rate of 0.017^{o}·s^{-1} in the range from 5 to 70° (2θ). The metal particle size was calculated from diffraction of Ni(111) by Scherrer equation.

The IR spectra of the adsorbed CO were recorded on a Bruker Vertex 70 spectrometer at a resolution of 4 cm^{-1} with 128 scans. The catalyst wafer was first reduced in situ in H$_2$ (1 bar) at 723 K for 1 h (heating rate = 10 K·min^{-1}), and then the system was evacuated for 1 h (p = 10^{-6} mbar). CO was adsorbed with an equilibrium pressure of 0.5 mbar at 313 K, followed by outgassing to remove the physically adsorbed CO. The IR spectra were recorded every five minutes until no changes in the spectra were observed. In order to directly compare the surface coverage of adsorbed CO, each spectrum reported was

normalized by the weight of the respective wafer. The IR spectra of the adsorbed phenol were measured with similar activation and adsorption procedures as described above, only that an equilibrium pressure of 0.05 mbar phenol was applied.

For measuring H_2 chemisorption, the Ni based catalyst was activated in vacuum at 588 K for 1 h and then cooled to ambient temperature. The H_2 adsorption isotherms accounting for both chemisorption and physisorption were measured in the pressure ranging from 1 to 0.4 bar. Afterwards, the system was evacuated for 1 h to remove physisorbed H_2. The concentration of chemisorbed hydrogen on the metal was determined by extrapolating the isotherm to zero H_2 pressure. The Ni dispersion was deduced by assuming an average H/Ni ratio of 1.

4.2.4. Catalytic measurements

The kinetic study of the aqueous-phase hydrodeoxygenation (HDO) of phenol was carried out as follows: 1.0 g reactant, 0.02 g Ni based catalyst, and 100 mL distilled water were charged into a batch autoclave (Parr Instrument, 300 mL), and stirred at the speed of 700 rpm. The reactor was purged with 30 bar H_2 at ambient temperature, and then heated up to 473 K at which the reaction started. Since in situ sampling was difficult to carry out for the biphasic reaction, the conversion/selectivity as a function of reaction time reported herein was obtained from the analysis of separate batch reactions with varied length of reaction time.

For HDO of catechol and guaiacol, 0.05 g of the catalyst was applied. With the saturated alcohol reactants, i.e., cyclohexane-1,2-diol and 2-methoxycyclohexanol, a reactant to catalyst ratio of 0.2 g/0.04 g was adapted due to their relatively low activities.

After each batch reaction, ethyl acetate was applied to extract the products in organic phase. Both aqueous-phase and organic-phase products were analyzed by a Shimadzu gas-chromatography mas-spectroscopy (GC–MS) equipped with a Flame ionization detector (FID) and a HP–5 capillary column. Conversion = (weight of converted reactant/weight of the starting reactant) × 100%. Yield of liquid products (C%) = (C atoms in liquid products / C atoms in the starting reactant) × 100%. Selectivity (C%) = (C atoms of each product / C atoms in all the liquid products) × 100%.

4.3. Results and Discussion

4.3.1. Catalysts characterization

The main physicochemical properties of the parent HZSM-5 and the Ni/HZSM-5 samples are compiled in Table 4-1. The Ni contents of the three Ni/HZSM-5 were comparable at 20 wt.% determined by AAS. N_2 adsorption–desorption isotherms were nearly identical for the three HZSM-5, with the same micropore volumes of $0.17\,cm^3 \cdot g^{-1}$, whereas for HZSM-5 with Si/Al of 11.5, the mesoporous surface area was notably lower than the other two samples, i.e., $28\,m^2 \cdot g^{-1}$ as compared to 57 and $77\,m^2 \cdot g^{-1}$. Upon addition of Ni, the volume of micropores decreased (0.17 to $0.12\,cm^3 \cdot g^{-1}$), indicating that a part of the Ni particles was located in the micropores.

Table 4-1. Physicochemical properties of parent HZSM-5 and Ni/HZSM-5 samples.

Catalyst	Si/Al ratio	BET surface area ($m^2 \cdot g^{-1}$)			Pore volume ($cm^3 \cdot g^{-1}$)		
		Micro	Meso	Total	Micro	Meso	Total
HZSM-5	11.5	386	28	414	0.17	0.04	0.21
	25	381	57	438	0.17	0.08	0.25
	90	362	77	439	0.17	0.09	0.26
Ni/HZSM-5 (20 wt.%)	11.5	261	30	291	0.12	0.05	0.17
	25	267	78	345	0.12	0.15	0.27
	90	232	114	346	0.11	0.15	0.26

The acidic properties of the catalysts and parent zeolites were probed by TPD of NH_3 and by the IR spectra of adsorbed pyridine (Py-IR) (Table 4-2). The two techniques showed excellent agreement in terms of total acid site concentrations (discrepancy $< 5\%$). For Ni/HZSM-5 and the parent HZSM-5, the concentration of Brønsted acid sites decreased as expected with increasing framework Si/Al ratio, i.e., 0.93, 0.44, and $0.14\,mmol \cdot g^{-1}$ for HZSM-5 11.5, 25, and 90, respectively. After deposition of Ni (II) salts, the concentrations of Brønsted acid sites decreased significantly to 0.38, 0.16, and

$0.08 \, mmol \cdot g^{-1}$. This is attributed to the hetero-condensation of the zeolite acidic hydroxyl groups with Ni(II) hydrooxoaqua complexes during the DP process.[13] In contrast, higher concentrations of Lewis acid sites were observed with Ni/HZSM-5 (0.39, 0.18, $0.11 \, mmol \cdot g^{-1}$) compared to parent HZSM-5 (0.15, 0.09, $0.01 \, mmol \cdot g^{-1}$) as the Si/Al ratio increased. These additional Lewis acid sites stem from the incompletely/un-reduced Ni cations, as confirmed for Ni/HBEA prepared by the DP method.[14]

Table 4-2. Acid characterization of parent HZSM-5 and Ni/HZSM-5 measured by TPD of NH_3 and IR spectra of adsorbed pyridine.

Catalyst	Si/Al ratio	Acid sites determined Py-IR $(mmol \cdot g^{-1})$			TPD-NH_3 $(mmol \cdot g^{-1})$
		Brønsted	Lewis	Total	
HZSM-5	11.5	0.93	0.15	1.07	1.07
	25	0.44	0.09	0.53	0.52
	90	0.14	0.01	0.15	0.14
Ni/HZSM-5 (20 wt.%)	11.5	0.38	0.39	0.77	0.79
	25	0.16	0.18	0.34	0.37
	90	0.08	0.11	0.19	0.17

XRD, TEM, and IR spectra of adsorbed CO were applied to characterize the size, morphology, and accessible fraction of Ni atoms in Ni/HZSM-5 catalysts (Figure 4-1). Based on the peak at the diffraction angle (2θ) of 44 ° (Figure 4-1a), $d_{Ni(111)}$ were calculated according to Scherrer equation to be 14, 5.2, and 6.5 nm (Table 4-3) for the supports with Si/Al ratios of 11.5, 25, 90, respectively. Two pronounced bands of adsorbed CO after evacuation appeared at $2040–2045 \, cm^{-1}$ and $1910–1970 \, cm^{-1}$ in the IR spectra (Figure 4-1b). The former is assigned to linearly adsorbed CO on Ni^0, the latter corresponds to two or three fold bridged adsorption of CO on Ni^0.[15] The integral area under these two bands is proportional to the concentration of accessible Ni^0 sites. Ni/HZSM-5 11.5 showed the smallest intensity of adsorbed CO, indicating that this sample had the lowest concentration of accessible Ni atoms. Hence, we conclude that the largest metal particles were formed on Ni/HZSM-5 11.5, in accordance with the results obtained from XRD diffractograms (see Table 4-3). This trend was also confirmed by

TEM images (Figure 4-1c), in which Ni/HZSM-5 11.5 showed the largest Ni particles with an average diameter of 11 nm, while the other two Ni/HZSM-5 samples displayed much smaller particles (5.6 and 5.8 nm).
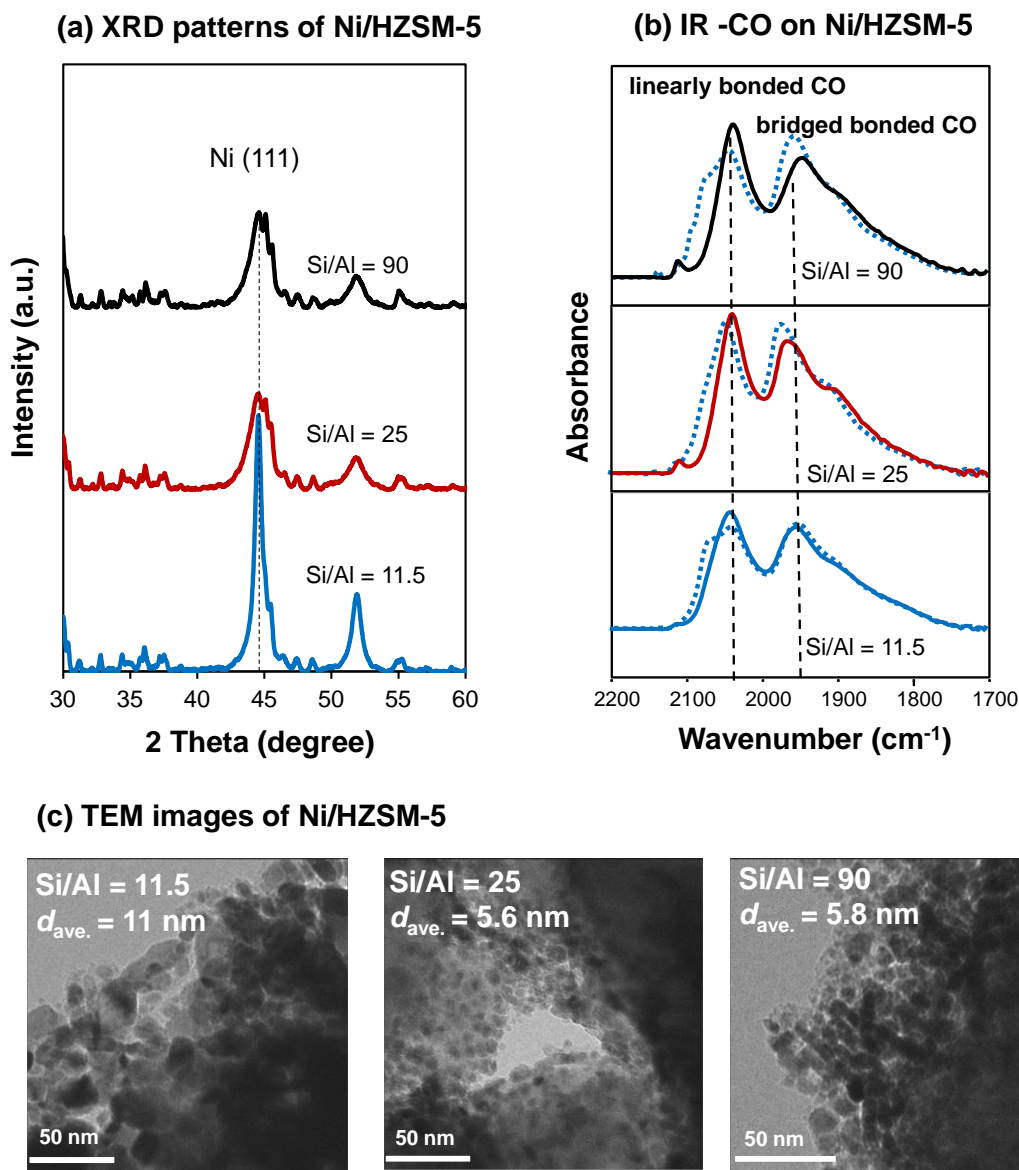

(a) XRD patterns of Ni/HZSM-5

(b) IR -CO on Ni/HZSM-5

(c) TEM images of Ni/HZSM-5

Figure 4-1. Characterization of Ni/HZSM-5 with three Si/Al ratios by (a) XRD patterns, (b) IR spectra of adsorbed CO, with dotted lines: at 0.5 mbar of CO equilibrium pressure, and solid lines: after evacuation, (c) TEM images.

Table 4-3. Ni size characterization of three Ni/HZSM-5 measured by TEM, XRD, and H_2 chemisorption.

Si/Al ratio	d_{TEM} (nm)	$d_{XRD\,Ni\,(111)}$ (nm)	$D_{H_2\,chem.}$ (%)
11.5	11 ± 3.4	14	3.6
25	5.6 ± 1.9	5.2	7.2
90	5.8 ± 2.2	6.5	9.6

Since all three Ni/HZSM-5 catalysts were prepared by the same deposition-precipitation method and the resulting Ni contents were nearly identical, the observed differences in the Ni particle sizes are tentatively related to differences during the preparation procedure induced by the zeolite properties. As pH values of the three zeolite suspensions were measured to be comparable (4.2 - 4.5), variations in the aqueous phase environment during Ni(II) deposition can be excluded. Burattin *et al.* explored key parameters controlling the size of supported metal particles prepared by the deposition-precipitation method,[16] including the nature of deposited Ni(II) phase as well as the strength and extent of metal-support interface. It was shown that the interface is manifested as a brucitic layer of octahedral Ni(II) bonding to the support surface, which provides anchoring sites for the overlying metal particles.[16b] In the present case, the nature of the deposited Ni(II) phase in these catalysts is considered to be identical for all three samples due to the similar HZSM-5 supports and DP conditions. However, the lowest mesoporous area of HZSM-5 with the framework Si/Al ratio of 11.5 (Table 4-1) was speculated to lead to a less extended Ni-support interface, as observed in the literature for low surface area SiO_2.[16a] In consequence, a relatively inhomogeneous Ni(II) phase was formed, leading to less uniformly distributed Ni nanoparticles. This trend agrees well with the observed drastic difference of Ni particle size and dispersion in the resultant catalyst samples.

In this contribution, Ni supported on neutral SiO_2 with a similar metal loading (20 wt.%) as the zeolite supported ones was also investigated as a reference catalyst. The results of various characterizations of Ni/SiO_2 are compiled in Figure 4-2 and Table 4-4. N_2 sorption isotherm showed a specific surface area of 211 $m^2 \cdot g^{-1}$ and a pore volume of

$0.52 \, cm^3 \cdot g^{-1}$. In particular, its mesoporous surface area ($194 \, m^2 \cdot g^{-1}$) was much larger than those of the three Ni/HZSM-5 catalysts (Table 4-1). The Ni particle size of Ni/SiO$_2$ was around 2.6 nm determined by XRD and TEM techniques (Figure 4-2), and the metal dispersion was 20% analyzed by H$_2$ chemisorption. The much smaller Ni particles present in the SiO$_2$ supported catalyst again could be related to its large mesoporous surface area as discussed above.
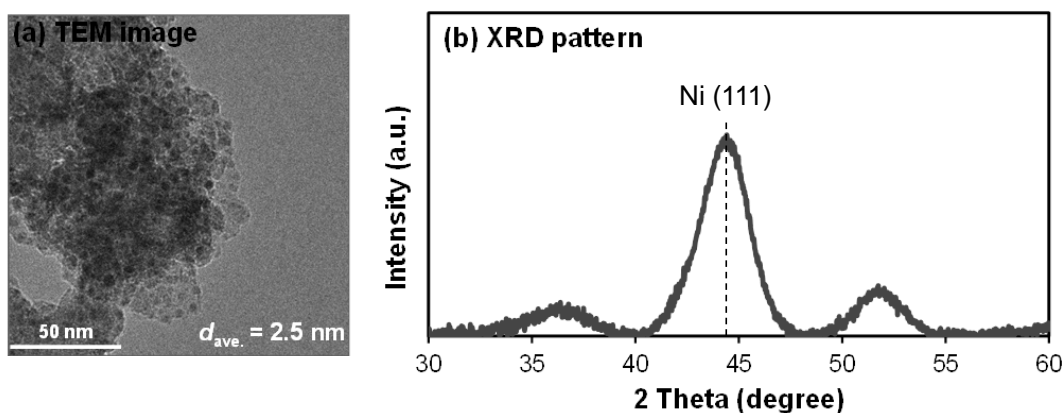

Figure 4-2. (a) TEM image and (b) XRD pattern of Ni/SiO$_2$.

Table 4-4. Characterization of the Ni/SiO$_2$ catalyst.

BET surface area ($m^2 \cdot g^{-1}$)			Pore volume ($cm^3 \cdot g^{-1}$)			d_{TEM} (nm)	$d_{XRD \, Ni \, (111)}$ (nm)	$D_{H_2 \, chem.}$ (%)
Micro-	Meso-	Total	Micro-	Meso-	Total			
17	194	211	0.008	0.511	0.519	2.5 ± 0.5	2.7	20

4.3.2. Hydrodeoxygenation of phenol

In order to explore the roles of acid and metals sites in the bifunctional Ni/HZSM-5 catalysts, kinetics of hydrodeoxygenation of phenol (as the simplest model compound) were performed in the aqueous phase at 473 K (Figure 4-3). The reaction proceeded in the similar pathway as proposed previously (Scheme 4-1).[9,17] Phenol was first hydrogenated by Ni forming cyclohexanone as primary product, which was gradually

converted further to cyclohexanol. In the presence of Brønsted acid sites, cyclohexanol was dehydrated to cyclohexene, which was subsequently hydrogenated to cyclohexane. Therefore, the overall reaction pathway for the cleavage of the aryl C−O bond in phenol requires two catalyst functions, with Ni catalyzing the hydrogenation of the aromatic ring and alkene, and acid sites mediating the dehydration of cyclohexanol.
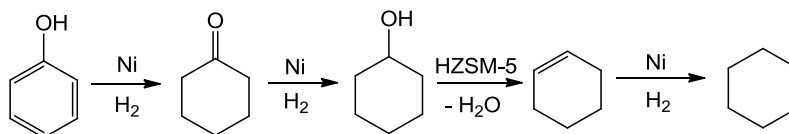
Scheme 4-1. Reaction pathway for phenol hydrodeoxygenation over Ni/HZSM-5 in the aqueous phase.

The rate for phenol hydrogenation on Ni is formally expressed as $r = k\,[Phenol]^a[H]^b$, where a and b denote the reaction order with respect to adsorbed phenol and H. In our case, the initial hydrodeoxygenation rates for the three Ni/HZSM-5 catalysts were comparable at 102, 88, and 84 mmol·g^{-1}·h^{-1} (Figure 4-3a). Considering that the concentration of accessible Ni was very different (Table 4-3), we speculate that concentrations of the adsorbed reactants are important properties determining the relative hydrogenation rates of this series of dual functional catalysts under selected conditions.
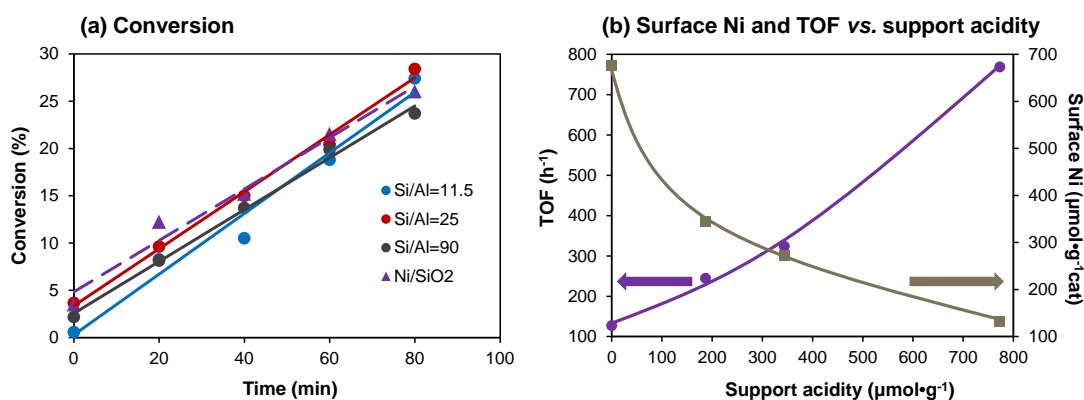
Figure 4-3. Phenol hydrodeoxygenation on Ni based catalysts as a function of reaction time, (a) conversion, and (b) Surface Ni atoms and turnover frequencies as a function of support acidity. Reaction conditions: 1.0 g phenol, 0.02 g catalyst, 473 K, 30 bar H$_2$ (ambient temperature), stirring at 700 rpm.

The concentration of phenol on Ni/HZSM-5 samples was estimated via the IR spectra of adsorbed phenol from gas phase recorded after evacuation at 313 K (Figure 4-4). Two bands at 1597 cm^{-1} and 1495 cm^{-1} are assigned to aromatic ring vibrations typical for phenate species; whereas the shoulder at 1475 cm^{-1} represents the C=C$_{ring}$ vibration characteristic of H-bonded phenols, with contribution from the –OH group.[18] The largest integral intensity was observed for Ni/HZSM-5 11.5 (Figure 4-4), pointing to the highest phenol concentration on this catalyst. It should be noted that in the sole presence of Brønsted acid sites such as macroporous solid acids like Amberlyst or heteropoly acids, phenol hardly adsorbs from the gas phase.[19] This implies that majority of the interaction results from strong dispersion forces upon physisorption of phenol in zeolite pores, as well as via its basic oxygen atom interacting with extra-lattice Al^{3+} cations, i.e., the strong Lewis acid sites of zeolites. The formation of H-bonded phenol originating from phenol interaction with SiOH groups or Brønsted acid sites in the zeolite cannot be fully excluded, as evidenced by the shoulder at ~1475 cm^{-1},[18] but such interactions of aromatic compounds with acid sites hardly contribute to the bonding.[20]
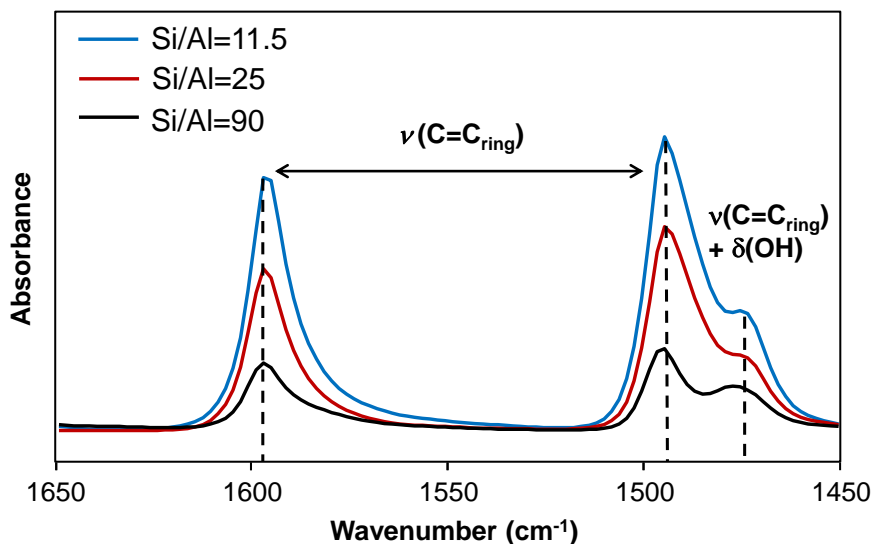
Figure 4-4. IR spectra of adsorbed phenol on Ni/HZSM-5 after evacuation at 313 K.

When intrinsic rates of these series of Ni based catalysts were considered, the turnover frequencies (TOF) followed the order of Ni/HZSM-5 11.5 (769 h^{-1}) > Ni/HZSM-5 25 (324 h^{-1}) > Ni/HZSM-5 90 (244 h^{-1}) > Ni/SiO$_2$ (127 h^{-1}), which was in

agreement with the decreasing Brønsted acid site concentrations of the respective supports (Figure 4-3b). This suggests that apart from catalyzing cyclohexanol dehydration, the presence of support acidity also substantially enhances the rate of the phenol hydrogenation step, i.e., with the increasing acid site concentration, the intrinsic hydrogenation rate increases accordingly.

Generally, the higher activities of noble metal (Pd or Pt) on acidic supports have been attributed in the past to modified adsorption properties and alteration of the metal band structure induced by proximal protons.[21] Though several models have been proposed, the nature of the addressed metal-proton interaction as well as its direct impact on the catalytic activity remains unclear. We would like to involve, therefore, a different explanation. It has been well demonstrated[22] that protonated pendant amine ligands when carefully positioned in organometallic complexes, enhance the rate of hydrogen oxidation or proton reduction by lowering free energy barriers for these catalytic reactions. The present case is speculated to resemble the effect of such molecular (electro)catalysis, in which the Brønsted acid site provides an additional delivery of the proton for the hydrogenation process.

By invoking such a cooperative action, the concentration of active H in the above addressed rate expression would not only be determined by the concentration of hydrogen adsorbed on the Ni particle, but also by the concentration of available protons in vicinity to Ni, hence Ni/HZSM-5 11.5 having the highest concentration of Brønsted acid sites (Table 4-2) would have the highest [H] concentration. On the other hand, the result of phenol adsorption on Ni/HZSM-5 with different framework Si/Al ratio suggests that the higher TOF could also be partially attributed to the enrichment of phenol and the reaction intermediates in the pores of the more acidic zeolite. Considering the reaction orders of *a* and *b* for adsorbed phenol and H were reported to be positive in the gas phase,[23] the enrichments of phenol and hydrogen would both positively influence the hydrogenation activity.

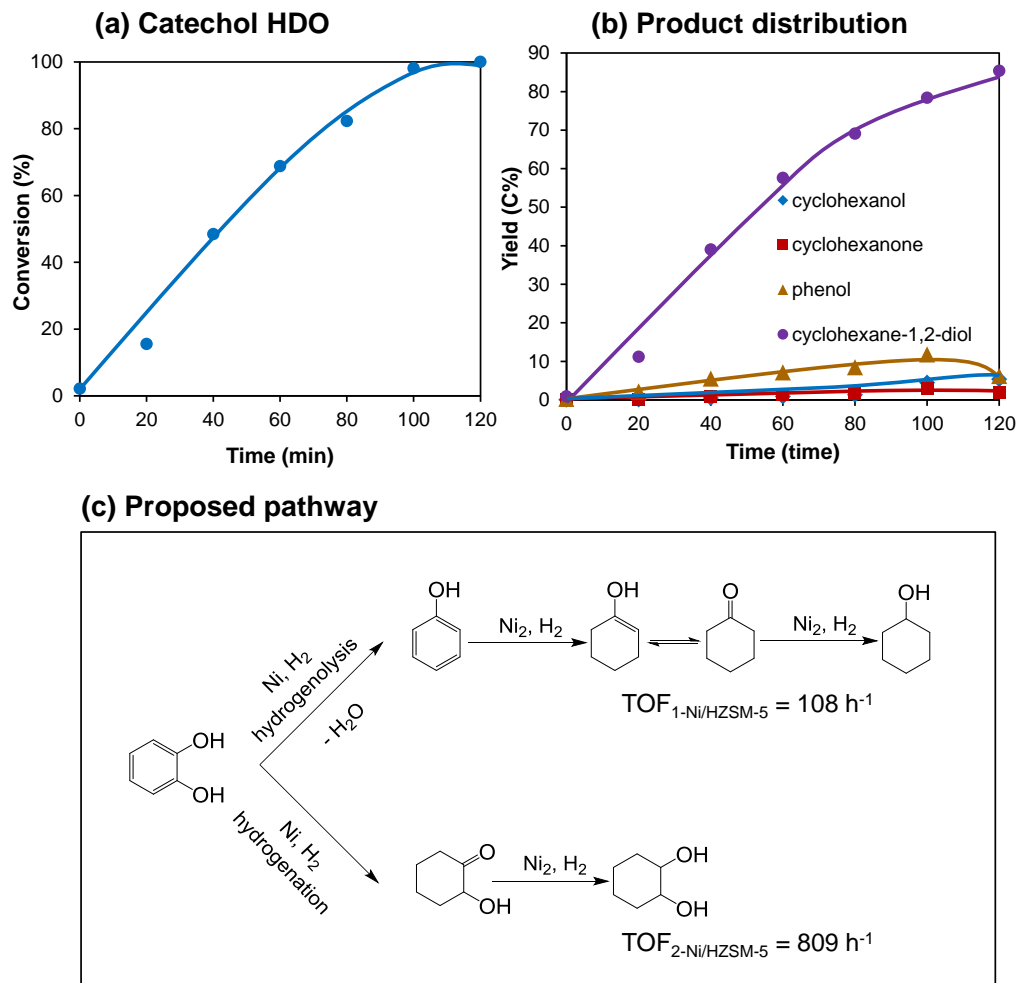### 4.3.3. Hydrodeoxygenation of catechol

Figure 4-5. Catechol hydrodeoxygenation over Ni/HZSM-5, (a) conversion, (b) product distribution, (c) proposed reaction pathway. Reaction conditions: 1.0 g catechol, 0.05 g Ni/HZSM-5, 473 K, 30 bar H_2 (ambient temperature), stirring at 700 rpm.

As Ni/HZSM-5 with the support framework Si/Al=11.5 showed the highest catalytic activity in phenol hydrodeoxygenation, it was chosen to study the kinetics of a stepwise aqueous-phase conversion of substituted phenolic monomers. Catechol, i.e., 1,2-dihydroxybenzene, was converted over this catalyst at 473 K in water (Figure 4-5). In order to explore the complete reaction network, a higher amount of catalyst was applied in comparison with phenol HDO. At the first stage of hydrodeoxygenation, aryl C−O bond hydrogenolysis and aromatic ring hydrogenation occurred in parallel. The latter

reaction dominated, leading primarily to cyclohexane-1,2-diol with around 85% yield after 120 min (Figure 4-5b). 2-Hydoxy cyclohexanone as a partial hydrogenation product of catechol was also observed in trace amounts (yield reached 2.4% at the first 20 minutes of reaction, and gradually consumed afterwards). The TOF for catechol hydrogenation on Ni was 809 $mol_{catechol} \cdot mol_{surf. Ni}^{-1} \cdot h^{-1}$ (accounting for contributions from both cyclohexane-1,2-diol and 2-hydroxy cyclohexanone), which was much lower than the Pd/C catalyzed rate ($\sim$3500 $mol_{catechol} \cdot mol_{surf. Pd}^{-1} \cdot h^{-1}$),[9] in line with the weaker hydrogenation ability generally observed for Ni compared to Pd. On the other hand, substantial concentrations of phenol were detected as the primary product (at $t = 100$ min, yield = 12%), suggesting Ni catalyzed also direct hydrogenolysis of the C_{aryl}–O bond in catechol, as an alternative pathway.[9] The formed phenol could be in turn gradually hydrodeoxygenated as proposed above. By comparison, with Pd/C as catalyst, the rate of aromatic ring hydrogenation was orders of magnitude faster than that of hydrogenolysis. Thus, only the hydrogenation product was observed during catechol conversion on Pd/C.[9,17a] It should be noted that benzene was not detected at any time during the conversion of catechol, and was also absent, when phenol was directly used as the reactant. This infers that C–O bond cleavage of phenol is not favored on Ni in the aqueous phase under the reaction conditions applied, albeit Ni is efficient in gas phase phenol hydrogenolysis.[24]

In summary, the C–O bond of catechol was directly cleaved by hydrogenolysis with a rate that was an eighth of the arene hydrogenation. The saturated diol produced could be further hydrodeoxygenated under more severe conditions. These results indicate that a much lower C–O hydrogenolysis barrier exists for catechol compared to phenol, which is attributed to the weaker C–O bond induced by electron donation from the adjacent –OH substituent[25] or the steric influence of the second *ortho*-substituted hydroxyl group in catechol.
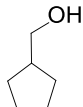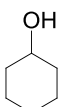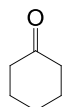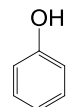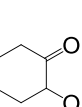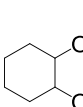
As phenol tends to be adsorbed in a co-planar manner at the acidic surface (Scheme 4-2a),[26] hydrogenation is favored. The steric hindrance from the second –OH group in catechol, or the –OCH$_3$ group in guaiacol, leads preferentially to a non-planar adsorption mode. Consequently, hydrogenolysis is more likely to take place on catechol and guaiacol (Scheme 4-2b).

(a) *Co*-planar adsorption of phenol

(b) *Non*-planar adsorption of catechol or guaiacol

R = H or CH$_3$
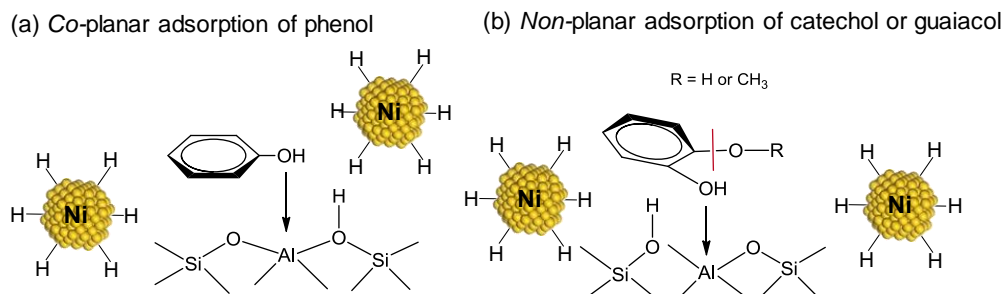
Scheme 4-2. Adsorption of (a) phenol (co-planar mode) and (b) catechol/guaiacol (non-planar mode) on Ni/HZSM-5.

As mono-functional catalyst, HZSM-5 alone was inactive for catechol conversion (Table 4-5). While with the reference Ni/SiO$_2$, TOFs calculated for hydrogenolysis and hydrogenation were only 24 and 155 mol$_{catechol}$·mol$_{surf.Ni}^{-1}$·h^{-1}, respectively (Table 4-5). This shows that hydrogenolysis and hydrogenation on mono-functional Ni/SiO$_2$ are much slower than on bifunctional Ni/HZSM-5, pointing again to the positive influences of support acidity on the Ni catalyzed steps. In analogy to the phenol hydrogenation discussed above, it is speculated that the acidic zeolite also enhances the adsorption of catechol, and provides abundant protons via zeolite Brønsted acid sites which are in close vicinity to the metal.

Table 4-5. Catechol hydrodeoxygenation over HZSM-5 or Ni/SiO$_2$ in separate experiments.[a]

Catalyst	Conv. (%)	Yield after 20 min (C%)						TOF$_1$[b] (h^{-1})	TOF$_2$[c] (h^{-1})
HZSM-5	-	-	-	-	-	-	-	-	-
Ni/SiO$_2$	31	-	0.05	0.20	3.8	0.37	26	24	155

[a] Reaction conditions: 1 g catechol, 0.05 g catalyst, 473 K, 30 bar H$_2$ (ambient temperature), stirring at 700 rpm, 20 min reaction.

[b] TOF$_1$ is defined as mole of catechol converted to hydrogenolysis product per mole of surface Ni site per hour.

[c] TOF$_2$ is defined as mole of catechol converted to hydrogenation products per mole of surface Ni site per hour.

Hydrodeoxygenation of cyclohexane-1,2-diol

Since *cis*-cyclohexane-1,2-diol was observed to be the main product from catechol hydrogenation, it was applied as substrate to further investigate the C−O bond cleavage mechanism over Ni/HZSM-5. To overcome the higher C−O bond dissociation energy of the saturated alcohol, higher temperature (523 K) and catalyst to reactant ratio (1 : 0.2) were employed. Cyclohexane-1,2-diol, the major product from catechol hydrogenation, was applied in the study. 70% cyclohexane-1,2-diol was converted in 2 h at 523 K (Figure 4-6a). Figure 4-6b shows the main products formed during cyclohexane-1,2-diol hydrodeoxygenation, including cyclohexanone, cyclohexanol, and isomerized products of cyclopentylmethanol, and cyclopentanecarbaldehyde.

Cyclohexanol could be formed either via direct hydrogenolysis of the C−O bond catalyzed by Ni or through a combination of acid catalyzed dehydration and Ni catalyzed alkene hydrogenation (Figure 4-6c). Note that in order to calculate the initial TOF for each individual pathway, the concentration of primarily formed cyclohexanone was applied to determine the dehydration TOF$_4$, while TOF$_3$ (hydrogenolysis) was calculated based on the concentration of cyclohexanol, assuming that cyclohexanone hydrogenation is much slower than dehydration of the saturated diol. Consequently, TOF$_3$ was slightly overestimated at 93 mol$_{cyclohexane-1,2-diol}$·mol$_{surf.Ni}^{-1}$·h^{-1}, as the contribution of cyclohexanol from cyclohexanone hydrogenation could not be fully excluded. Apart from cyclohexanone and cyclohexanol, isomerized ketone and alcohol were also produced via acid catalyzed pinacol rearrangement in the presence of the acid catalyst (Figure 4-6c).[27] The dehydration route forming cyclohexanol had a TOF$_4$ of 21 mol$_{cyclohexane-1,2-diol}$·mol$_{BAS}^{-1}$·h^{-1}, and the dehydration/isomerization pathway providing isomerized cyclopentyl methanol also reached a comparable initial TOF$_5$ of 29 mol$_{cyclohexane-1,2-diol}$·mol$_{BAS}^{-1}$·h^{-1} (Figure 4-6c). Note that the C−O bond hydrogenolysis rate of cyclohexane-1,2-diol on Ni/HZSM-5 was lower than that of catechol at 473 K, leaving cyclohexane-1,2-diol almost unconverted under lower temperature (Figure 4-5b). This is related to both steric and electronic effects. The planar benzyl molecule with highly delocalized π orbitals

facilitates higher adsorption constants of aromatic molecules,[28] in comparison with saturated cyclic compounds with less regular chair conformation and sp^3 orbitals.
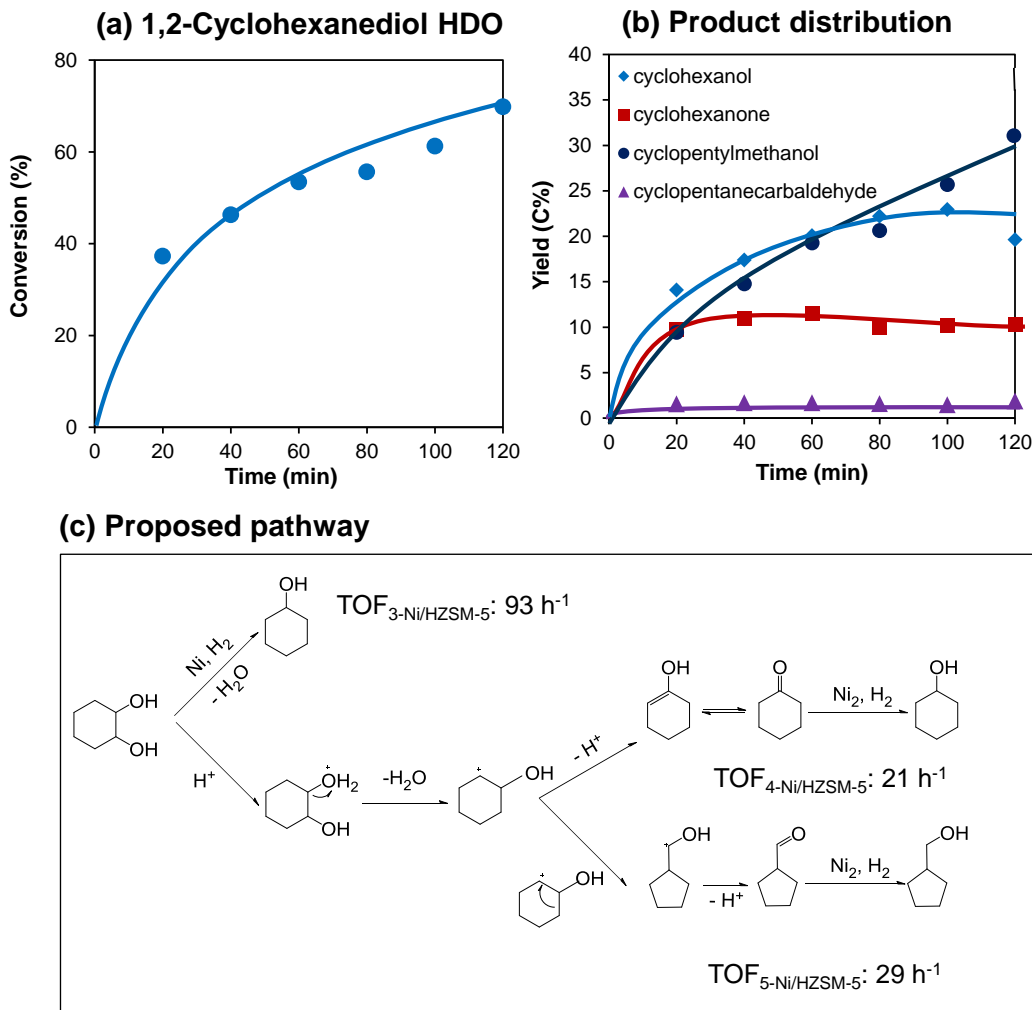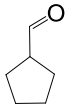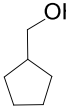
(a) 1,2-Cyclohexanediol HDO

(b) Product distribution
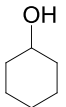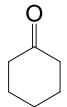
(c) Proposed pathway

Figure 4-6. Cyclohexane-1,2-diol hydrodeoxygenation over Ni/HZSM-5, (a) conversion, (b) product distribution, (c) proposed reaction pathway. Reaction conditions: 0.2 g cyclohexane-1,2-diol, 0.04 g Ni/HZSM-5, 523 K, 30 bar H$_2$ (ambient temperature), stirring at 700 rpm.

With mono-functional Ni/SiO$_2$ or HZSM-5, different product distributions in separate experiments were observed for cyclohexane-1,2-diol HDO (Table 4-6). HZSM-5 led to highly selective dehydration, with direct dehydration of TOF$_4$ at 16 mol$_{cyclohexane-1,2-diol}$·mol$_{BAS}^{-1}$·h^{-1} and dehydration/isomerization of 3.0 mol$_{cyclohexane-1,2-diol}$·mol$_{BAS}^{-1}$·h^{-1}. The isomerization rate on HZSM-5 was one magnitude lower than that on Ni/HZSM-5 (3

versus 29 h^{-1}), suggesting that Ni helps to facilitate the carbocation rearrangement at the acid sites. On the other hand, the hydrogenolysis activity with Ni/SiO$_2$ (11 h^{-1}) was about nine times lower than that of Ni/HZSM-5 (93 h^{-1}), demonstrating again the synergistic effects between Brønsted acid and Ni sites for enhancing the catalytic activity of the metal. Note that some isomers of cyclopentylmethanol and aldehyde were also observed with Ni/SiO$_2$ catalyzed reaction, probably formed due to the presence of the hydronium ions originating from hot liquid water at 523 K (pH = 5.5).[29]

Table 4-6. 1,2-Cyclohexanediol hydrodeoxygenation over mono-functional

HZSM-5 or Ni/SiO$_2$ [a]

Catalyst	Conv. (%)	Yield after 2 h (C%)				TOF$_3$ [b] (h^{-1})	TOF$_4$ [c] (h^{-1})	TOF$_5$ [d] (h^{-1})
HZSM-5	82	12	1.1	0.7	68	-	16	3.0
Ni/SiO$_2$	68	2.7	18	20	27	11	-	-

[a] Reaction conditions: 0.2 g 1,2-cyclohexanediol, 0.04 g catalyst, 523 K, 30 bar H$_2$ (ambient temperature), stirring at 700 rpm, 2 h reaction.

[b] TOF$_3$ is defined as mole of 1,2-cyclohexanediol converted to hydrogenolysis product per mole of surface Ni site per hour.

[c] TOF$_4$ is defined as mole of 1,2-cyclohexanediol converted to dehydration product per mole of Brønsted acid site per hour.

[d] TOF$_5$ is defined as mole of 1,2-cyclohexanediol converted to dehydration-isomerization products per mole of Brønsted acid site per hour.

In summary, at 523 K the C−O bond cleavage of cyclohexane-1,2-diol was concluded to proceed with parallel routes of direct Ni-catalyzed hydrogenolysis and acid-catalyzed dehydration, reaching an initial TOF of approximately one sixth of that observed with catechol，even at elevated temperature.

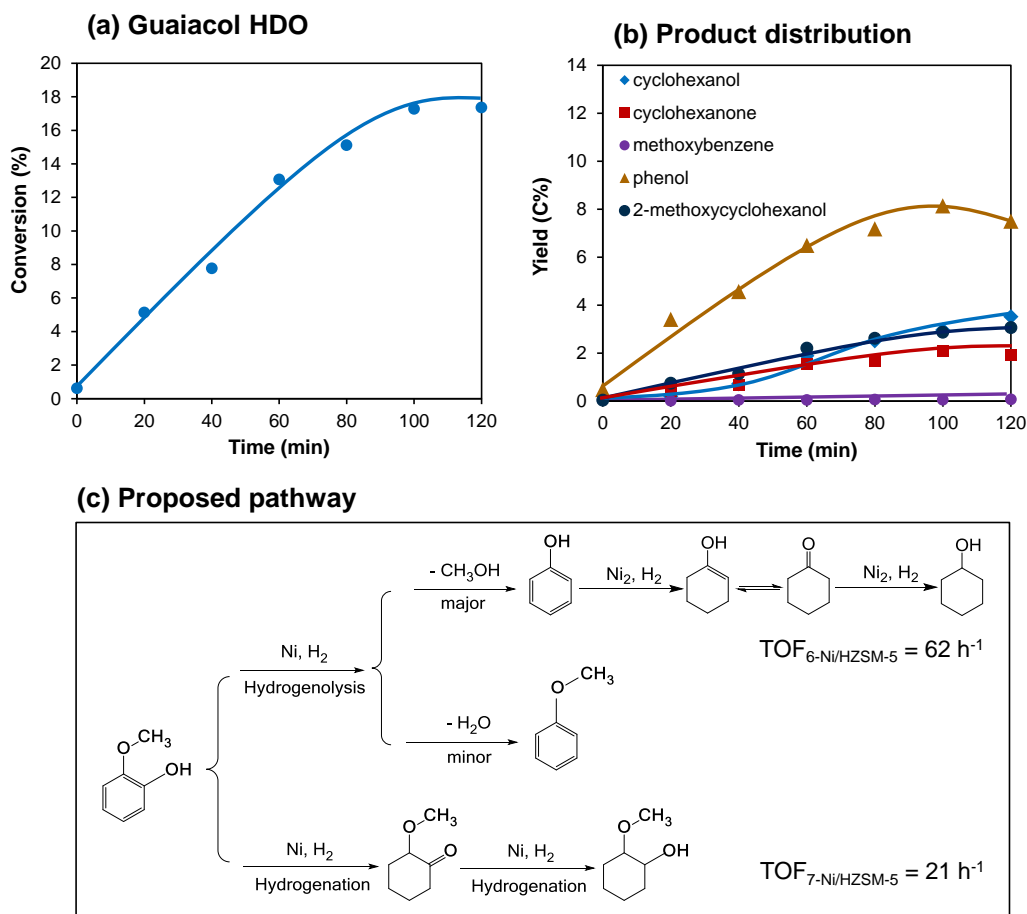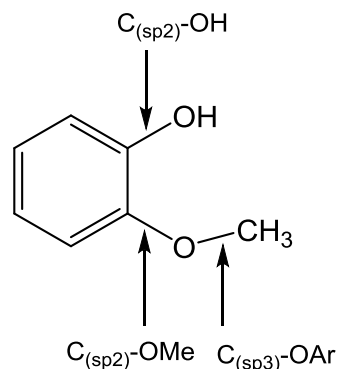### 4.3.4. Hydrodeoxygenation of guaiacol

Figure 4-7. Guaiacol hydrodeoxygenation over Ni/HZSM-5, (a) conversion, (b) product distribution, (c) proposed reaction pathway. Reaction conditions: 1 g guaiacol, 0.05 g Ni/HZSM-5, 473 K, 30 bar H_2 (ambient temperature), stirring at 700 rpm.

Guaiacol, i.e., 2-methoxyphenol with adjacent –OH and –OCH$_3$ group at the aromatic ring, is the most abundant phenolic monomer from lignin depolymerization.[30] Hydrodeoxygenation of guaiacol at 473 K led to the formation of a wide range of products including cyclohexanol, cyclohexanone, aromatics, and methanol (Figure 4-7b). Similarly to catechol, hydrogenation and hydrogenolysis occurred in parallel on Ni/HZSM-5. The TOF of guaiacol hydrogenation only reached 21 mol$_{guaiacol}$·mol$_{surf.Ni}^{-1}$·h^{-1} (Figure 4-7c), which was a magnitude slower than the hydrogenation of catechol or phenol. The steric influence of the *ortho*-substituted sp^3 methoxy group is concluded to make the co-planar adsorption of the aromatic ring more difficult compared to phenol and

catechol, and hence, cause the low hydrogenation activity. This trend was also observed for the Pd catalyzed hydrodeoxygenation of phenolic monomers in the aqueous phase.[9]

The structure of guaiacol contains three types of C-O bonds, i.e., $C_{(sp3)}$−OAr, $C_{(sp2)}$−OMe, and $C_{(sp2)}$−OH (see Figure 4-8), with the respective bond dissociation energy (BDE) of 262 – 276, 409 – 421, and 466 kJ/mol. From the BDE point of view, the energy barrier of $C_{(sp2)}$−OH bond scission is the highest, and this corresponds well with our result in which the yield of methoxybenzene was lower than 0.1% (Figure 4-7b). Demethylation via $C_{(sp3)}$−OAr bond scission is more

Figure 8. Stucture of guaiacol

favorable compared with demethoxylation via cleavage of the $C_{(sp2)}$−OMe bond in terms of bond-strength. For instance, sulfide catalysts usually lead to hydrogenolysis of guaiacol through demethylation forming catechol.[7] Surprisingly, only trace amount of catechol was observed in the present case, while phenol (including cyclohexanone, cyclohexanol, and cyclohexane as subsequent products) was the dominant primary product (at t = 20 min, selectivity = 78 C%). Moreover, the fact that methanol was formed at a yield of around 1/6 of phenol, together with the absence of methane in the gas phase confirmed the dominant pathway of direct demethoxylation via the cleavage of C_{aryl}−OMe bond, and the demethylation route on Ni/HZSM-5 was excluded under the present reaction conditions. The demethoxylation pathway was also observed for guaiacol hydrodeoxygenation at 543-573 K in the gas phase when Co promoted transition metal sulfide[31a] or carbon supported CoMo catalysts[31b] were used. The high preference for demethoxylation over demethylation is speculated to be caused by the steric constraints, i.e., the C_{aryl}−OMe bond approaches Ni surface more easily.
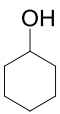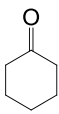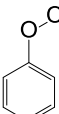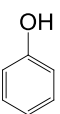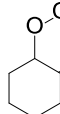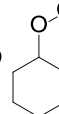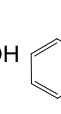
In summary, hydrogenolysis is faster than hydrogenation for guaiacol hydrodeoxygenation, with a ratio of 3:1. This is in contrast to catechol conversion, possibly due to the more pronounced steric impact of sp^3 hybrid Me−OAr orbital than the sp^2 hybrid C_{aryl}−OH orbital.

Employing HZSM-5 alone yielded only 0.8% catechol via guaiacol hydrolysis at 473 K (Table 4-7). This suggests again that hydrolysis of methoxy groups with acid sites

is a negligible pathway for guaiacol conversion under the selected conditions. Thus, Ni is shown to be the active site.

Remarkably also in this case, the mono-functional Ni/SiO$_2$ led to much lower hydrogenation and hydrogenolysis TOFs than Ni/HZSM-5; the latter reached a TOF$_7$ (hydrogenation) of 21 *versus* 6.2 h^{-1} and a TOF$_6$ (hydrogenolysis) of 62 *versus* 14 h^{-1} (Table 4-7), respectively; in perfect agreement with the results of catechol conversion. The presence of support acidity pronouncedly enhances the rates of Ni-catalyzed steps; this implies again that protons might be directly involved in the catalytic processes in a way that has been suggested for the benhanced rate of hydrogen oxidation in organometallic complexes.[22c]

Table 4-7. Guaiacol hydrodeoxygenation over mono-functional HZSM-5 or Ni/SiO$_2$ [a]

Catalyst	Conv. (%)	Yield after 40 min (C%)							TOF$_6$ [b] (h^{-1})	TOF$_7$ [c] (h^{-1})
HZSM-5	0.79	-	-	-	-	-	-	0.79	-	-
Ni/SiO$_2$	13	1.9	1.3	0.04	5.9	0.86	3.0	-	14	6.2

[a] Reaction conditions: 1 g guaiacol, 0.05 g catalyst, 473 K, 30 bar H$_2$ (ambient temperature), stirring at 700 rpm, 40 minute reaction.

[b] TOF$_6$ is defined as mole of guaiacol converted to hydrogenolysis product per mole of surface Ni site per hour.

[c] TOF$_7$ is defined as mole of guaiacol converted to hydrogenation products per mole of surface Ni site per hour.

Hydrodeoxygenation of 2-methoxycyclohexanol

Although both *cis-* and *trans-* forms of 2-methoxycyclohexanol were intermediately formed from guaiacol hydrogenation, the *trans-* conformer dominated and thus it was selected to explore the further hydrodeoxygenation (Figure 4-9a).
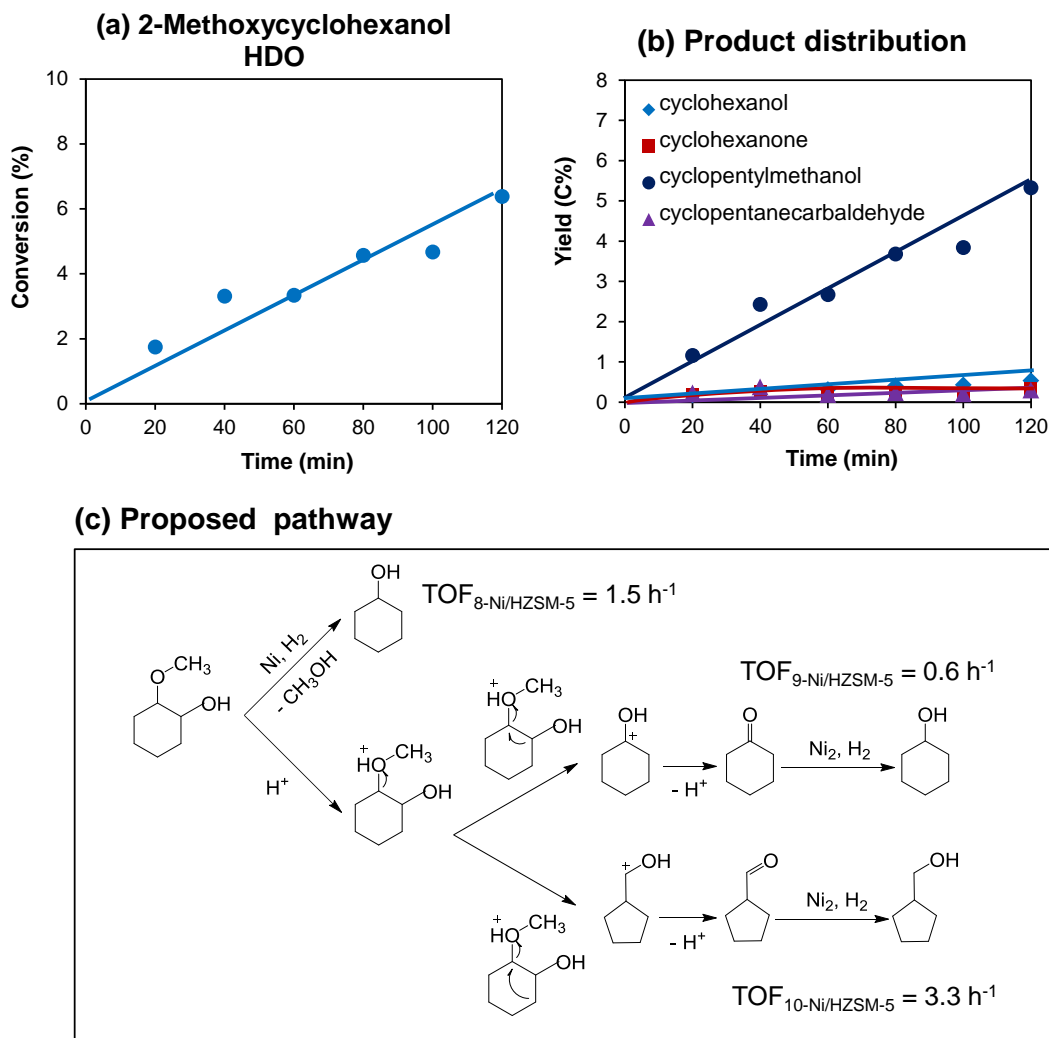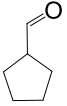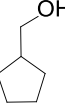
(a) 2-Methoxycyclohexanol HDO

(b) Product distribution

(c) Proposed pathway

$TOF_{8\text{-Ni/HZSM-5}} = 1.5\ h^{-1}$

$TOF_{9\text{-Ni/HZSM-5}} = 0.6\ h^{-1}$

$TOF_{10\text{-Ni/HZSM-5}} = 3.3\ h^{-1}$
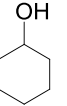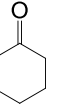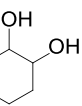
Figure 4-9. 2-Methoxycyclohexanol hydrodeoxygenation over Ni/HZSM-5, (a) conversion, (b) product distribution, (c) proposed reaction pathway. Reaction conditions: 0.2 g 2-methoxycyclohexanol, 0.04 g Ni/HZSM-5, 523 K, 30 bar H_2 (ambient temperature), stirring at 700 rpm.

At 523 K, 2-methoxycyclohexanol was shown to be readily converted to cyclohexanol, cyclohexanone and their isomers over Ni/HZSM-5 (Figure 4-9b) similarly to the reaction of cyclohexane-1,2-diol. However, in the case of 2-methoxycyclohexanol, isomerized cyclopentylmethanol was primarily formed (at t = 2 h, selectivity > 80 C%), unlike the conversion of cyclohexane-1,2-diol, in which direct dehydration (TOF = 21 h^{-1}) and dehydration/isomerization (TOF = 29 h^{-1}) proceeded in parallel pathways with nearly equal contribution. This implies that in spite of the similar final products,

hydrodeoxgenation of 2-methoxycyclohexanol passes through a different transition state compared to the one proposed for cyclohexane-diol (Figure 4-9c). On the other hand, even increasing both temperature and the amount of catalyst, the conversion of 2-methoxycyclohexanol over Ni/HZSM-5 (6.4%) was about three times lower than guaiacol conversion (18%) at 473 K after 2 h. This is probably resulted from the steric and electronic influences of the saturated cyclic ring as discussed for cyclohexane-diol. 2-Methoxycyclohexanol was also much less active than the saturated diol, with an initial rate of conversion of 6.4 h^{-1} compared to 143 h^{-1}. Structural influences of the *ortho*-substituted –OCH$_3$ group should have accounted for the observed low activity.

The kinetics of applying solely HZSM-5 or Ni/SiO$_2$ was investigated with 2-methoxycyclohexanol at 523 K in separate experiment (Table 4-8). HZSM-5 alone catalyzed sequential hydrolysis and dehydration of 2-methoxycyclohexanol, with TOF$_9$ (towards cyclohexanone) of 0.8 h^{-1} and TOF$_{10}$ (towards cyclopentane carbaldehyde) of 3.9 h^{-1}. This shows that the catalytic function of HZSM-5 is quite similar to that of the acid sites in Ni/HZSM-5 for 2-methoxycyclohexanol conversion. Low concentrations of cyclohexane-diol were detected, while this product was absent with Ni/HZSM-5 catalyzed reactions. This is attributed to the absence of the metal-catalyzed hydrogenolysis of cyclohexane-diol, as its consumption rate through hydrogenolysis is relatively fast (TOF = 93 h^{-1}, Figure 4-6c) in comparison to its formation rate via hydrolysis. With the metal function only (Ni/SiO$_2$), the hydrogenolysis activity towards the formation of cyclohexanol (TOF: 0.5 h^{-1}) was slower than that catalyzed by Ni/HZSM-5 (TOF: 1.5 h^{-1}) (Figure 4-9c), confirming again the enhanced activity of Ni in presence of Brønsted acid sites. Some dehydration products were also observed, which were catalyzed by the hydronium ions originated from hot liquid water at 523 K as discussed above.

Table 4-8. 2-Methoxycyclohexanol hydrodeoxygenation over mono-functional HZSM-5 or Ni/SiO$_2$ [a]

Catalyst	Conv. (%)	Yield after 2h (C%)					TOF$_8$ [b] (h^{-1})	TOF$_9$ [c] (h^{-1})	TOF$_{10}$ [d] (h^{-1})
HZSM-5	8.3	7.1	-	-	0.90	0.34	-	0.8	3.9
Ni/SiO$_2$	5.3	0.5	4.0	0.54	0.29	-	0.5	-	-

[a] Reaction conditions: 0.2 g 2-methoxycyclohexanol, 0.04 g catalyst, 523 K, 30 bar H$_2$ (ambient temperature), stirring at 700 rpm, 2 h reaction.

[b] TOF$_8$ is defined as mole of 2-methoxycyclohexanol converted to hydrogenolysis product per mole of surface Ni site per hour.
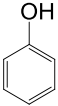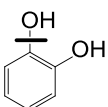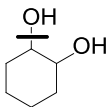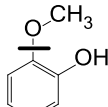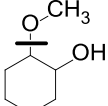
[c] TOF$_9$ is defined as mole of 2-methoxycyclohexanol converted to dehydration product per mole of Brønsted acid site per hour.

[d] TOF$_{10}$ is defined as mole of 2-methoxycyclohexanol converted to dehydration-isomerization products per mole of Brønsted acid site per hour.

4.3.5. Overall hydrodeoxygenation pathways and rates of conversion of phenolic monomers

The activities and reaction pathways for cleaving the C−O bonds in phenol, catechol, and guaiacol over mono- or dual-functional Ni and HZSM-5 were summarized in Table 4-9. Under selected conditions with Ni/HZSM-5, phenol was hydrogenated to cyclohexanol in the first stage, and the C−O bond of cyclohexanol was subsequently cleaved by dehydration, which is similar to Pd/C-H$_3$PO$_4$ catalyzed phenol hydrodeoxygenation.[9] However, with the adjacent –OH or –OCH$_3$ functional group attached to *ortho* position of the phenolic ring, the reaction pathways for converting catechol and guaiacol change.

Table 4-9. C−O bond cleavage pathways for phenolic monomers over Ni and HZSM-5 sites.

Entry	Reactant	C−O Cleavage Pathway	Active Center	TOF (h^{-1})		
				Ni/HZSM-5	HZSM-5	Ni/SiO$_2$
1	OH (phenol)	hydrogenation-dehydration	Ni [a]	769	-	127
2	OH, OH (catechol)	hydrogenation	Ni [a]	809	-	155
		hydrogenolysis	Ni [a]	108	-	24
3	OH, OH (cyclohexane-1,2-diol)	hydrogenolysis	Ni [b]	93	-	11
		dehydration	HZSM-5 [b]	50	19	-
4	O-CH$_3$, OH (guaiacol)	hydrogenation	Ni [a]	21	-	6.2
		hydrogenolysis	Ni [a]	62	-	14
5	O-CH$_3$, OH (2-methoxycyclohexanol)	hydrogenolysis	Ni [b]	1.5	-	0.5
		demethoxylation	HZSM-5 [b]	3.9	4.7	-

[a] Temperature: 473 K.

[b] Temperature: 523 K.

Catechol was hydrogenated to cyclohexane-1,2-diol (major) and hydrogenolyzed to phenol (minor) in parallel routes over Ni/HZSM-5. Subsequently, phenol was hydrodeoxygenated following the conventional hydrogenation-dehydration route, whereas cyclohexane-1,2-diol was further converted through either dehydration or hydrogenolysis to cleave the aliphatic C−O bonds. Guaiacol, however, was hydrogenolyzed via demethoxylation of C$_{aryl}$−OMe bond as the dominant route, forming phenol as the major primary product. The remaining fully hydrogenated 2-methoxycyclohexanol was converted either through cleavage of the C$_{alkyl}$-OMe bond on Ni forming methanol and cyclohexanol, or via acid mediated pathways toward the final formation of cyclohexanol and cyclopentylmethanol. The proposed reaction networks of

catechol and guaiacol differ from the Pd-acid catalyzed reaction pathways, in which the cleavage of the C_{aryl}−O bond starts via full arene hydrogenation on Pd followed by $C_{aliphatic}$−O bond scission through acid catalyzed dehydration or hydrolysis.[9] This indicates that the Pd catalyzed hydrogenation rate is significantly higher than the hydrogenolysis rate, whereas Ni is a better hydrogenolysis catalyst. The proposed mechanism is also different from the sole C−O bond hydrogenolysis pathway by sulfide transition metal catalysts in the gas phase.[7]

Phenolic monomers are generally more active than the corresponding fully hydrogenated intermediates. For example, the hydrogenation and hydrogenolysis rates of catechol were 809 and 108 h^{-1} on Ni/HZSM-5 at 473 K, respectively; while the hydrogenolysis of cyclohexane-diol was only 93 h^{-1} even at elevated temperature of 523 K (Table 4-9, Entries 2-3). Similarly, the hydrogenolysis rate of 2-methoxycyclohexanol was a magnitude lower than that of guaiacol on Ni/HZSM-5 (Table 4-9, entries 4-5). Again, the observed differences in reactivity are attributed to both steric and electronic constraints to cleave the C-O bond at the saturated ring. These results are of great importance to guide the lignin depolymerization and the subsequent upgrading processes, i.e., direct hydrogenolysis of C_{aryl}−OR is much easier than hydrogenolysis of the respective $C_{alphatic}$−OR.

The results summarized in Table 4-9 show clearly that the presence of support acidity has a positive impact on the activities of Ni catalyzed steps. For instance, the TOF of phenol hydrogenation was 769 h^{-1} over Ni/HZSM-5, and 127 h^{-1} for Ni/SiO$_2$. Similarly, the rates of hydrogenation and hydrogenolysis of catechol were 809 and 108 h^{-1} on Ni/HZSM-5, while Ni/SiO$_2$ only achieved TOFs of 155 and 24 h^{-1} under the same conditions. Similarly, rates of guaiacol HDO were much higher with Ni/HZSM-5 than with Ni/SiO$_2$. The acid support is on the one hand enhancing the strength of adsorption of the phenolic monomers. On the other hand, the present case might be a remarkable analogy to the rate enhancements observed for hydrogen oxidation by organometallic complexes, where Brønsted acid sites are speculated to be directly involved in the hydrogenation reaction. It highlights the importance of synergistic effects of proximal metal and acid sites in a bifunctional catalyst where a fraction of Ni being catalytically active is present in the vicinity of the zeolite acid sites.

4.4. Conclusions

The mechanisms for C−O bond cleavage in phenol, catechol, and guaiacol have been investigated in the aqueous phase. Remarkable synergistic effects with Ni supported on and in HZSM-5 pores are described. Phenol is hydrodeoxygenated on Ni/HZSM-5 through primary hydrogenation to cyclohexanol, and the subsequent dehydration of cyclohexanol, followed by cyclohexene hydrogenation, in analogy to the conversions catalyzed by Pd in the presence of aqueous mineral acids. Catechol is converted by parallel hydrogenation (forming cyclohexane-1,2-ol, 89%) and hydrogenolysis (forming phenol, 11%) over Ni/HZSM-5. The C−O bond of cyclohexane-1,2-diol is readily cleaved either by direct hydrogenolysis over Ni (major route), or by further dehydration and pinacol rearrangement on acid sites (minor route). For the hydrodeoxygenation of guaiacol, hydrogenation (25%) and hydrogenolysis (75%) pathways proceed in parallel, producing 2-methoxycyclohexanol and phenol as primary products. 2-methoxycyclohexanol can be in turn either hydrogenolyzed to cyclohexanol (minor route) by Ni, or converted via demethoxylation and rearrangement steps (major route) catalyzed by acid sites.

The catalytic conversions of saturated cyclic alcohols are much slower than those of their respective phenolic monomers, suggesting that the cleavage of C−O bonds attached to the saturated ring is more difficult. This is attributed to the difference in hybridization, which imposes a steric constraint for the active metal center to approach the C-O bonds. The Ni/HZSM-5 for hydrodeoxygenation of phenolic monomers utilizes both Ni and Brønsted acid functions to seamlessly catalyze the cascade reactions, more importantly, the acid sites in the vicinity of metal lead to markedly promoted rates in hydrogenation and hydrogenolysis. The synergistic effect contributes to prominent rate enhancement compared to Ni/SiO$_2$ catalysts. This increase is tentatively attributed to the combination of a higher concentration of the reacting substrate and an additional delivery of hydrogen through protons from the nearby strong Brønsted acid sites.

4.5. Acknowledgements

References

[1]   a) F. S. Chakar, A. Ragauskas, *J. Ind. Crops Prod.*, **2004**, *20*, 131; b) J. Zakzeski, P. C. A. Bruijnincx, A. L. Jongerius, B. M. Weckhuysen, *Chem. Rev.*, **2010**, *110*, 3552.

[2]   M. Stöcker, *Angew. Chem., Int. Ed.*, **2008**, *47*, 9200.

[3]   G. W. Huber, A. Corma, *Angew. Chem., Int. Ed.*, **2007**, *46*, 7184.

[4]   E. Furimsky, *Appl. Catal. A*, **2000**, *199*, 147.

[5]   S. W. Benson, in *Thermochemical Kinetics,* Wiley, New York, 1968.

[6]   a) M. J. Girgis, B. C. Gates, *Ind. Eng. Chem. Res.*, **1991**, *30*, 202; b) H. Topsøe, B. S. Clausen, F. E. Massoth, *Hydrotreating Catalysis Science and Technology*, Springer, Berlin, 1996.

[7]   a) M. Ferrari, A. Centeno, C. Lahousse, R. Maggi, P. Grange, B. Delmon, *Am. Chem. Soc. Div. Petr. Chem. Prepr.*, **1998**, *43*, 94; b) J. B.-son Bredenberg, M. Huuska, P. Toropainen, *J. Catal.*, **1989**, *120*, 401; c) E. Laurent, B. Delmon, *Appl. Catal.*, **1994**, *109*, 97.

[8]   A. Centeno, E. Laurent, B. Delmon, *J. Catal.*, **1995**, *154*, 288.

[9]   C. Zhao, J. He, A. A. Lemonidou, X. Li, J. A. Lercher, *J. Catal.*, **2011**, *280*, 8.

[10] C. Zhao, J. A. Lercher, *Angew. Chem. Int. Ed.*, **2012**, *51*, 5935.

[11] R. Nares, J. Ramírez, A. Gutiérrez–Alejandre, C. Louis, T. Klimova, *J. Phys. Chem. B*, **2002**, *106*, 13287.

[12] a) B. C. Lippens, B. G. Linsen, J. H. d. Boer, *J. Catal.*, **1964**, *3*, 32; b) W. D. Harkins, G. Jura, *J. Am. Chem. Soc.*, **1944**, *66*, 1366.

[13] P. Burattin, M. Che, C. Louis, *J. Phys. Chem. B*, **1998**, *102*, 2722.

[14] a) W. Song, C. Zhao, J. A. Lercher, *Chem. Eur. J.*, **2013,** *19,* 9833; b) C. Zhao, T. Brück, J. A. Lercher, *Green Chem.*, **2013,** *15*, 1720.

[15] a) K. Hadjiivanov, M. Mihaylov, D. Klissurski, P. Stefanov, N. Abadjieva, E. Vassileva, L. Mintchev, *J. Catal.*, **1999**, *185*, 314; b) A. G. Sault, C. H. F. Peden, E. P. Boespflug, *J. Phys. Chem.*, **1994**, *98*, 1652; c) J. Leglise, A. Janin, J. C. Lavalley, D. Cornet, *J. Catal.*, **1988**, *114*, 388; d) L. Bonneviot, F. Cai, M. Che, K. Kermarec,

O. Legendre, C. Lepetit, D. Olivier, *J. Phys. Chem.*, **1987**, *91*, 5912; e) J. B. Peri, *J. Catal.*, **1984**, *86*, 84.

[16] a) P. Burattin, M. Che, C. Louis, *J. Phys. Chem. B*, **1997**, *101*, 7060; b) P. Burattin, M. Che, C. Louis, *J. Phys. Chem. B*, **1999**, *103*, 6171; c) P. Burattin, M. Che, C. Louis, *J. Phys. Chem. B*, **2000**, *104*, 10482.

[17] a) C, Zhao, Y. Kou, A. A. Lemonidou, X. Li, J. A. Lercher, *Angew. Chem. Int. Ed.*, **2009**, *48*, 3987; b) C. Zhao, J. A. Lercher, *ChemcatChem*, **2012**, *4*, 64.

[18] A. Popov, E. Kondratieva, J. M. Goupil, L. Mariey, P. Bazin, J.-P. Gilson, A. Travert, F. Maugé, *J. Phys. Chem. C*, **2010**, *114*, 15661.

[19] C. Zhao, D. M. Camaioni, J. A. Lercher, *J. Catal.*, **2012**, *288*, 92.

[20] A. Jentys, R. R. Mukti, H. Tanaka, J. A. Lercher, *Micropor. Mesopor. Mater.*, **2006**, *90*, 284.

[21] a) G. Larsen, G. L. Haller, *Catal. Lett.*, **1989**, *3*, 103; b) Z. Karpiński, S. N. Gandhi, W. M. H. Sachtler, *J. Catal.*, **1993**, *141*, 337; c) B. L. Mojet, J. T. Miller, D. E. Ramaker, D. C. Koningsberger, *J. Catal.*, **1999**, *186*, 373.

[22] a) M. R. Dubois, D. L. Dubois, *Acc. Chem. Res*. **2009**, *42*, 1974; b) M. O' Hagan, W. J. Shaw, S. Raugei, S. Chen, J. Y. Yang, U. J. Kilgore, D. L. Dubois, R. M. Bullock, *J. Am. Chem. Soc.* **2011,** *133,* 14301; c) M. O'Hagan, M. H. Ho, J. Y. Yang, A. M. Appel, M. Rakowski DuBois, S. Raugei, W. J. Shaw, D. L. DuBois, R. M. Bullock, *J. Am. Chem. Soc.* **2012,** *134,* 19409; d) T. Liu, D. L. DuBois, R. M. Bullock, *Nature Chem.*, **2013**, *5*, 228.

[23] N. Mahata, K. V. Raghavan, V. Vishwanathan, *Catal. Today*, **1999**, *49*, 65.

[24] a) E.-J. Shin, M. A. Keane, *Ind. Eng. Chem. Res.*, **2000**, *39*, 883; b) J. B-son Bredenberg, M. Huuska, J. Räty, M. Korpio, *J. Catal.*, **1982**, *77*, 242.

[25] E.-J. Shin, M. A. Keane, *J. Catal.*, **1998**, *173*, 450.

[26] G. Neri, A. M. Viso, A. Donato, C. Milone, M. Malentacchi, G. Gubitosa, *Appl. Catal. A*, **1994**, *110*, 49.

[27] T. Xu, J. F. Haw, *J. Am. Chem. Soc.*, **1994,** *116,* 7753.

[28] C. Zhao, Y. Yu, A. Jentys, J. A. Lercher, *Appl. Catal. B*, **2013**, *132-133*, 282.

[29] G. C. Akerlof, H. I. Oshry, *J. Am. Chem. Soc.*, **1950**, *72*, 2844.

[30] V. M. Roberts, V. Stein, T. Reiner, A. A. Lemonidou, J. A. Lercher, *Chem. Eur. J.*, **2011**, *17*, 5939.

[31] a) V. N. Bui, D. Laurenti, P. Afanasiev, C. Geantet, *Appl. Catal. B*, **2011**, *101*, 239; b) M. Ferrari, R. Maggi, B. Deomon, P. Grange, *J. Catal.*, **2001**, *198*,

Chapter 5

Aqueous Phase Hydroalkylation and Hydrodeoxygenation of Phenol by Dual Functional Catalysts Comprised of Pd/C and H/La-BEA

Aqueous phase catalytic phenol hydroalkylation and hydrodeoxygenation have been explored using Pd/C combined with zeolite H-BEA and La-BEA catalysts in the presence of H_2. The individual steps of phenol hydrogenation, cyclohexanol dehydration, or alkylation with phenol were individually investigated to gain insight into the relative rates in the cascade reactions of phenol hydroalkylation. The hydroalkylation rate, determined by the concentrations of phenol and cyclohexanol in phenol hydroalkylation, required the hydrogenation rate to be relatively slow. The optimized H^+/Pd ratio was 21, which allowed achieving comparable cyclohexanol formation rates via phenol hydrogenation and consumption rates from alkylation with phenol in phenol hydroalkylation. La-BEA was shown to be more selective for hydroalkylation than H-BEA in combination with Pd/C, because cyclohexanol dehydration was retarded selectively compared to alkylation of phenol. This indicates that dehydration is solely catalyzed by Brønsted acid sites, while alkylation can be achieved in the presence of La^{3+} cations.

5.1. Introduction

Selective transformation of lignocellulosic biomass into hydrocarbons that are suitable to be directly blended into liquid transportation fuels has been identified as one of the important targets in the conversion of bioderived raw materials.[1] In that context bifunctional catalysts containing metal and acid sites have been developed to convert lignin and cellulose derived phenols, aldehydes, alcohols, and furans to C_5-C_9 hydrocarbons.[2–11] However, it would be interesting to be able to selectively produce heavier (diesel range) hydrocarbons from lignocellulosic biomass.

Recently we reported in that context a novel route to aqueous phase hydroalkylation and deoxygenation of lignin derived C_6-C_9 phenolic oil to $C_{12}-C_{18}$ hydrocarbons over Pd/C and zeolite H-BEA catalysts.[7] In the previous work, a detailed study of individual reactions of (substituted) phenol and their potential products (cyclohexanol, cyclohexanone, and cyclohexene) demonstrates that phenol selectively reacts with the in situ generated cyclohexanol or cyclohexene on Brønsted acid sites. The selectivity for phenol hydroalkylation depends on the concentrations of phenol and in situ formed cyclohexanol from phenol hydrogenation, as well as on the ratio of phenol to cyclohexanol determined by the rate of hydrogenation and the extent of reaction.

The presence of La^{3+} cation in zeolites has been reported to have positive effects ranging from stabilizing the zeolite against dealumination, modifying acid strength, and uniquely enhancing hydride transfer reactions, which have been found to be important for alkylation reactions.[12,13] Indeed, partially La^{3+} exchanged BEA and X type zeolites have shown high activity for carbon−carbon coupling reactions such as Friedel−Crafts acylation[14] and alkylation.[15]

In our quest to enhance the selectivity for hydroalkylation we compare, therefore, the catalytic properties of H-BEA and La-BEA in the presence of Pd/C in the aqueous phase. The individual kinetics of the aqueous phase dehydration, alkylation, and hydroalkylation−deoxygenation reactions of phenol are explored. In addition, an extensive characterization on these two zeolites was performed to elucidate the relationship between the catalyst properties and catalytic activities including their deactivation during hydroalkylation−deoxygenation of phenol.

5.2. Experimental section

5.2.1. Chemicals

Zeolite H-BEA (H-form, Si/Al = 75, Clariant), Pd/C (5 wt % loading, Sigma-Aldrich), La(NO_3)$_3$ (Sigma-Aldrich, purity > 99%), phenol (Sigma-Aldrich, 99.5%), cyclohexanone (Sigma-Aldrich, 99%), cyclohexanol (Sigma-Aldrich, 99%), ethyl acetate (Sigma-Aldrich, > 99%), NH_3 (Air Liquide, > 99.999%), N_2 (Air Liquide, > 99.999%), He (Air Liquide, > 99.999%), and H_2 (Air Liquide, > 99.999%).

5.2.2. Ion exchange procedure for preparing La-BEA catalyst

Zeolite H-BEA (H-Form) was ion-exchanged in 200 ml 0.2 M La(NO_3)$_3$ solution at 343 K for 2 h with stirring. Then, the exchanged zeolite was washed five times with 100 ml deionized water , and dried at 393 K for 12 h. Washed La-BEA was calcined in air (flow rate: 100 ml·min^{-1}) at 723 K for 1 h with a heating rate of 2 K·min^{-1}. This ion exchange procedure was repeated three times.

5.2.3. Catalyst characterization

Atomic absorption spectroscopy (AAS) for chemical analysis was obtained on a UNICAM 939 AA-Spectrometer. N_2 adsorption-desorption was carried out at 77 K using PMI automatic BET-Sorptometer. Scanning electron microscopy (SEM) was obtained on a JEOL 500 SEM-microscope. X-ray diffraction (XRD) patterns were recorded with a Philips X`Pert Pro System (Cu K$_\alpha$: 0.1540 nm) operated at 40 kV/40 mA, in the range from 2θ = 5-70 ° with a step size of 0.05 ° per minute. The lanthanum concentration was determined by inductively coupled plasma (ICP) optical emission spectrometry FTMOA81A ICP-OES from Spectro-Analytical Instrument. Calibrating standards with 0, 10, 50, 75, and 100 ppm were prepared with lanthanum standard in a 5% w/w nitric acid solution.

The ^{27}Al and ^{29}Si MAS NMR spectra are recorded on a Bruker AV500 spectrometer. For ^{27}Al MAS NMR measurements, the samples were hydrated for three nights in a desiccator containing a beaker with water. Spectra measured were the sum of 2400 sweeps with a recycle time of 250 ms. The chemical shifts were referenced using an external standard of solid Al(NO$_3$)$_3$ (δ = -0.54 ppm). The ^{29}Si MAS NMR spectra recorded were the sum of at least 10,000 sweeps with a recycle time of 5 s. The excitation pulse had a length of 1.2 μs. The spectra were referenced to tetrakis(trimethylsilyl)silane (δ = -9.843 ppm). All NMR spectra were fitted with Gaussian functions for quantitative deconvolution of overlapping peaks.

Temperature programmed desorption of NH$_3$ (TPD-NH$_3$) was performed under flow conditions with six-channels. First the catalysts were activated in He at 623 K for 1 h using a heating rate of 5 K·min^{-1} from ambient temperature to 623 K. NH$_3$ was then adsorbed from 10 vol.% in the He carrier gas (total flow 30 ml·min^{-1}, p = 30 mbar) at 373 K. The sample was purged with He for 2 h to remove physisorbed NH$_3$. Desorbing NH$_3$ of was monitored by mass spectrometry (MS; Balzers QME 200).

IR spectra of adsorbed pyridine were recorded on a Perkin–Elmer 2000 spectrometer operating at a resolution of 4 cm^{-1}. The catalyst samples were activated in vacuum (p = 10^{-6} mbar) at 673 K for 1 h, then exposed to pyridine (p_{Py} = 10^{-1} mbar) at 423 K for 0.5 h. After evacuating at 423 K for 1 h, the spectra were recorded until the equilibrium had been achieved. IR spectra of adsorbed phenol or cyclohexanol were measured by the same procedure.

The matrix-assisted laser desorption/ionization (MALDI) time-of-flight mass spectra (TOF/MS) were recorded using a Bruker Biflex III MALDI-TOF mass spectrometer equipped with an N$_2$ laser (v = 337 nm) ionization source operating at a pulse rate of 3 Hz. The ions were accelerated with pulsed-ion extraction after a delay of 50 ns at a voltage of 28.5 kV. The microchannel plate detector was operated in reflection mode. The mass spectrometer was calibrated with a polystyrene standard.

5.2.4. Catalytic reactions

Cyclohexanol dehydration, cyclohexanol−phenol alkylation, and phenol hydroalkylation−deoxygenation

Typically, a mixture of phenol (15 g), H2O (80 mL), Pd/C (5 wt.% Pd, 0.040 g), and H-BEA (0.20 g, Si/Al = 75) was loaded into an autoclave (Parr Instrument Co., 300 mL). The reactor with a stirring rate of 680 rpm was flushed with H_2 three times, subsequently the temperature was increased to 473 K, and 6 MPa H_2 was introduced at 473 K. The reactor was sampled after quenching with ice to ambient temperature, and organic products were extracted by ethyl acetate. The organic and aqueous phases were both analyzed by gas chromatography (GC; Shimadzu 2010, flame ionization detector) with a HP-5 capillary column (30 m × 250 μm) and a gas chromatography−mass spectrometry combination (GC−MS; Shimadzu QP 2010S). The carbon balance was better than 93 ± 3%. As this was a twophase reaction, real-time sampling was difficult. The conversion/ selectivity data were measured in separate experiments with varying duration times. The calculations of conversion and selectivity were based on a carbon mole basis, for which the terms are defined as follows: conversion = (starting material loss/initial charge) (100%); selectivity = (C atoms in each product/total C atoms in the products) (100%).

Catalyst recycling test

Catalyst stability was tested by recovering and reusing the catalyst charge as follows. A mixture of phenol (20 g), H-BEA or La-BEA (0.4 g), Pd/C (0.080 g), and H_2O (80 mL) was loaded into the Parr autoclave (300 mL). Reaction was conducted at 473 K and 6 MPa H_2 at a stirring speed of 700 rpm for 0.5 h. The reaction was quenched in ice, and the catalyst was separated from the aqueous phase by centrifugation, washed with acetone and water, dried in air at 383 K overnight, and reused in the next run. The catalyst recoveries were higher than 90 wt.%. Four recycling runs were conducted in the present work.

5.3. Results and discussion

5.3.1. Catalyst characteristics

This work uses as metal catalyst Pd/C and as acid catalysts H-BEA and La-BEA. The characteristics of Pd/C are compiled in the Supporting Information with the information of N_2 sorption, AAS, XRD, SEM, and TEM. Pd/C catalysts had a metal loading of 5 wt. % and BET surface area of $1062\,m^2\,g^{-1}$ with a pore volume of $0.54\,cm^3\,g^{-1}$ and a mean pore diameter of 3.7 nm (Table 5A-1 in the Appendix). The Pd^0 particle size of this catalyst was ca. 2.3 nm, calculated from a TEM image. The characteristics of acidic zeolites of H-BEA and La-BEA are described below.

Characterization of texture and morphology of BEA

Table 5-1. Element compositions, BET surface areas, and pore volumes of H–BEA and La–BEA.

	H–BEA	La–BEA
Element composition		
Si (AAS) (wt.%)	39.9	41.5
Al (AAS) (wt.%)	0.602	0.574
Na (AAS) (wt.%)	0.002	0.002
La (ICP) (wt.%)	-	1.22
Si/Al (mol·mol^{-1})	64	70
BET surface area (m^2·g^{-1})	684	628
Mesopore surface area (m^2·g^{-1})	140	138
Micropore surface area (m^2·g^{-1})	544	490
Pore volume (cm^3·g^{-1})	0.43	0.40
Mesopore volume (cm^3·g^{-1})	0.21	0.20
Micropore volume (cm^3·g^{-1})	0.22	0.20
Mean pore diameter (nm)	3.6	3.6

The results of the physicochemical characterization of H-BEA and La-BEA are compiled in Table 5-1. La-BEA was obtained from the exchange of H-BEA with

La(NO$_3$)$_3$ three times at 343 K, and the La content in La-BEA was 1.22 wt. % measured by ICP. The framework Si/Al ratios of H-BEA and La-BEA were 64 and 70, respectively, which indicates that dealumination occurred during the cation exchange and calcination process. The BET surface areas of H-BEA and La-BEA were comparable at 684 and 628 m^2 g^{-1}, respectively, with pore volumes of 0.43 and 0.40 cm^3 g^{-1} at pore diameters of 3.6 nm.
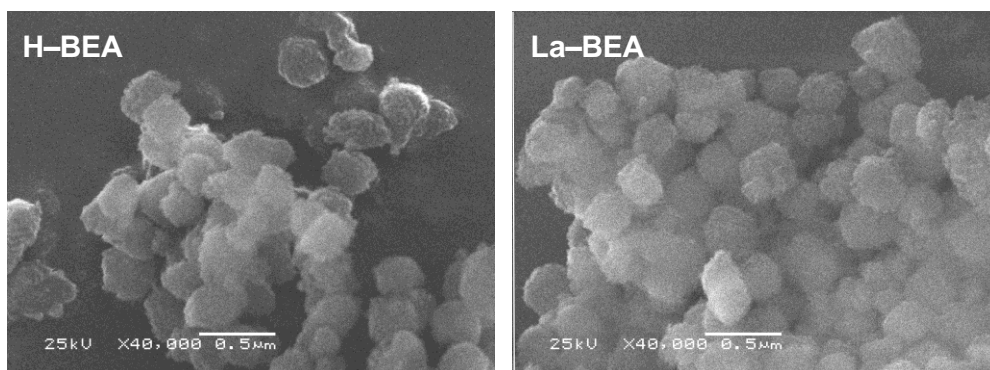

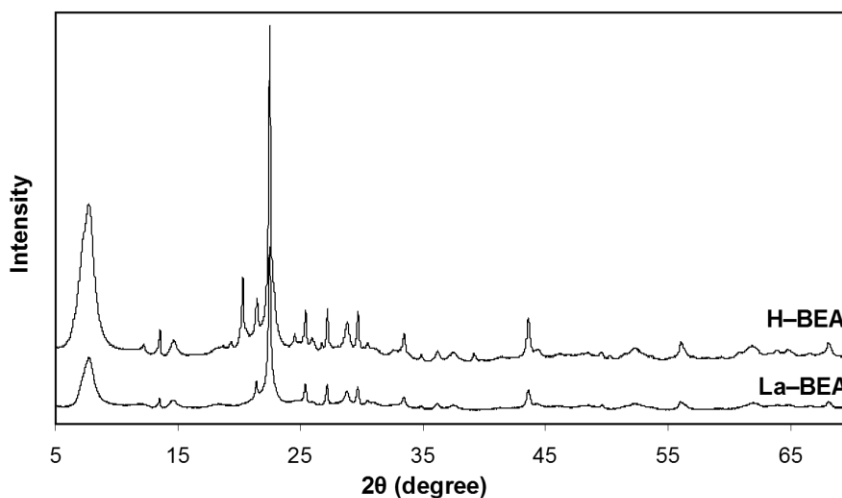**Figure 5-1.** SEM images of H-BEA and La-BEA catalysts.

Figure 5-2. XRD patterns of H-BEA and La-BEA catalysts.

The SEM images of La-BEA and H-BEA show similar particles with an average size of 0.3 μm (Figure 5-1), implying that the particle size did not change during the cation exchange process. However, the partial loss of crystallinity upon La^{3+} cation exchange

was detected by X-ray diffraction (XRD) (Figure 5-2). The strong reflections of La-BEA at 2θ of 7.5 and 22.5° were dramatically decreased compared to H-BEA. This indicates that the ion exchange and calcination procedures led to a partial loss of crystallinity of BEA.

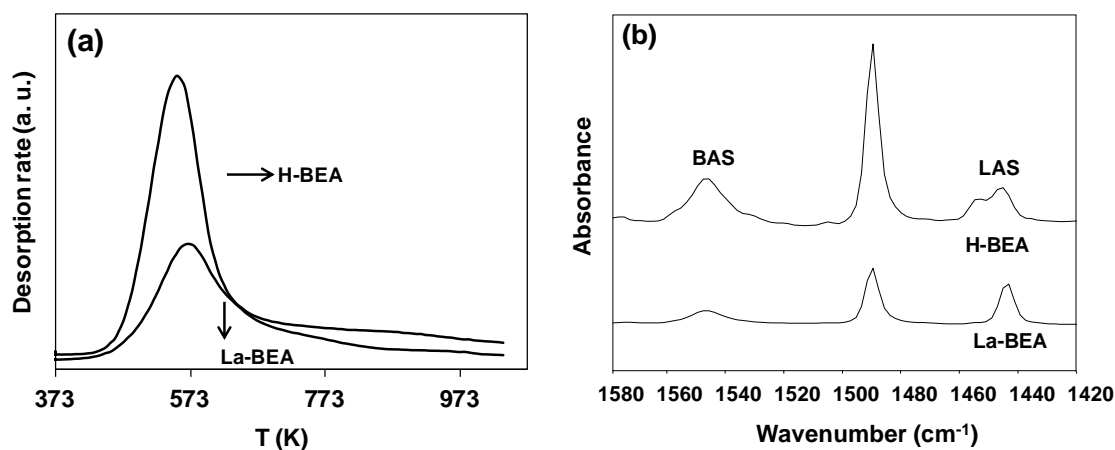### *Characterization of acid sites of BEA catalysts*

Figure 5-3. (a) Temperature programmed desorption of ammonia and (b) IR spectra of adsorbed pyridine on H-BEA and La-BEA catalysts.

The distributions and concentrations of acid sites were measured by temperature programmed desorption of NH_3 (TPD-NH_3). The maximum NH_3 desorption from the H-BEA and La-BEA zeolites appeared at 553 and 573 K, respectively (Figure 5-3a). The acid concentrations on H-BEA and La-BEA from TPD-NH_3 were 0.280 and 0.131 mmol g^{-1}, respectively (Table 5-1). Acid sites were also probed by IR spectroscopy of adsorbed pyridine (Py-IR; Figure 5-3b). The concentrations of Brønsted acid sites (BAS) and Lewis acid sites (LAS) were determined from the IR absorption bands at 1550 and 1450 cm^{-1}, respectively. The measured LAS concentrations for H-BEA and La-BEA were comparable at 0.066 and 0.065 mmol g^{-1} (Table 5-1), but the BAS of H-BEA (0.201 mmol g^{-1}) was almost 4 times as high as that of La-BEA (0.058 mmol g^{-1}). The sums of acid concentrations from TPD-NH_3 were 10% higher than those determined by IR spectroscopy of adsorbed pyridine (Table 5-2), attributed to differences in the sampling techniques.

Table 5-2. Acid Site Concentrations of Phenol and Cyclohexanol on H-BEA and La-BEA

Acid sites	H-BEA	La-BEA
Acidity (Py-IR) (mmol·g^{-1})	0.267	0.123
Brønsted acid sites (BAS) (mmol·g^{-1})	0.201	0.058
Lewis acid sites (LAS) (mmol·g^{-1})	0.066	0.065
Acidity (TPD-NH$_3$) (mmol·g^{-1})	0.280	0.131

Characterization of framework structure of BEA catalysts

Table 5-3. Fitting parameters of the ^{29}Si MAS NMR spectra of H-BEA and La-BEA.

Si (nAl)	H-BEA			La-BEA		
	Chemical shift (ppm)	Line width (ppm)	Relative area (%)	Chemical shift (ppm)	Line width (ppm)	Relative area (%)
$n = 3$	−91.7	0.7	0.06	−91.7	1.4	0.2
$n = 1$	−101.4	2.6	6.6	−101.4	2.6	6.4
$n = 0$	−104.6	2.2	4.6	−104.6	2.3	4.0
	−110.7	2.7	39.2	−110.7	2.8	39.9
	−113.9	2.7	28.8	−111.4	18.8	25.7
	−114.8	19.8	20.8	−114.0	2.6	26.5

The ^{29}Si MAS NMR spectra of H-BEA and La-BEA (Figure 5-4a) show six peaks from Si atoms with zero to four nearest Al atoms. The fitting parameters of the ^{29}Si NMR spectra of hydrated H-BEA and La-BEA are compiled in Table 5-3. Based on Loewenstein's rule, Si/Al ratios in the framework of zeolite were determined to be 60 and 62 for H-BEA and La-BEA catalysts, respectively, which agrees well with the AAS results indicating Si/Al ratios of 64 and 70, respectively.
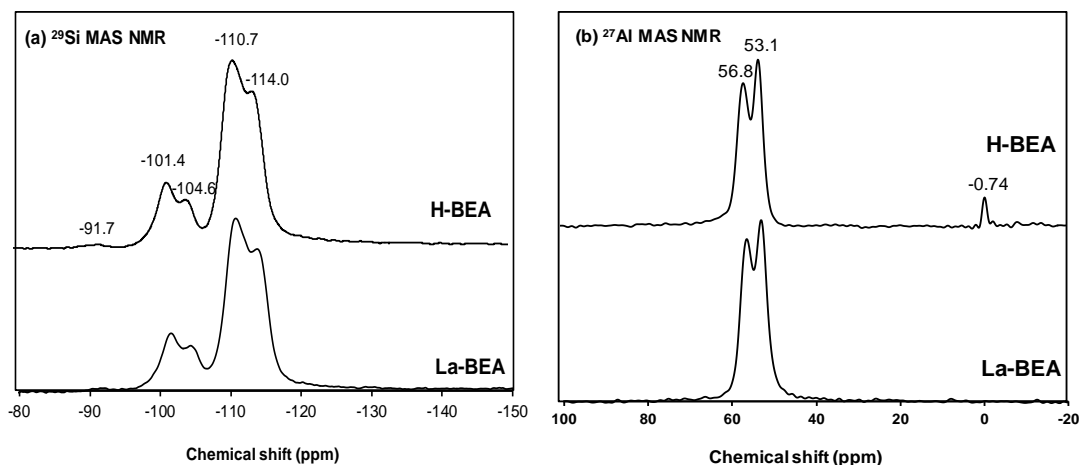
Figure 5-4. (a) ^{29}Si and (b) ^{27}Al MAS NMR spectra of H-BEA and La-BEA.

The local environments of the Al atoms in H-BEA and La-BEA were investigated by ^{27}Al MAS NMR spectroscopy (Figure 5-4b). The overlapping peaks at 53 and 57 ppm (from both H-BEA and La-BEA) are attributed to tetrahedrally coordinated Al (T_d Al) in the zeolite framework with protons or La^{3+} as charge compensating cations, respectively. The peak H-BEA at 0 ppm is assigned to octahedrally coordinated Al (O_h Al), present as extraframework species. The fitting results are compiled in Table 5-4, and the decreasing octahedral aluminum concentration from H-BEA (0.008 mmol g^{-1}) to La-BEA (0 mmol g^{-1}) indicates that dealumination occurred during the calcination after ion exchange in the aqueous solution. In particular it is noteworthy that all extralattice octahedral aluminum has been removed from the zeolite material. In comparison, the AAS results (shown in Table 5-1) showed that La-BEA lost 0.010 mmol g^{-1} Al from the ion exchange treatment on H-BEA. The concentration of T_d aluminum in the lattice was slightly lower than the acid site concentration measured by IR spectroscopy of adsorbed pyridine, i.e., 0.214 mmol g^{-1} from ^{27}Al MAS NMR and 0.267 mmol g^{-1} from Py-IR for H-BEA, as well as 0.095 and 0.123 mmol g^{-1} from ^{27}Al MAS NMR and Py-IR for La-BEA, respectively. This indicates that weak Brønsted acid sites such as silanol nests generated by dealumination should contribute to the overall Brønsted acid site concentration.

Table 5-4. Fitting parameters of the ^{27}Al MAS NMR spectra of hydrated H-BEA and La-BEA.

H-BEA Assignment	δ (ppm)	QCC (MHz)	Relative area (%)	Conc. $(mmol \cdot g^{-1})$[a]
Td Al^{3+} close to H$^+$	56.8	3.0	51.3	0.114
	53.1	2.4	45.2	0.100
Seperate EFAL phase[b]	-0.74	1.0	3.5	0.008
La-BEA Assignment	δ (ppm)	QCC (MHz)	Relative area (%)	Conc. $(mmol \cdot g^{-1})$[a]
Td Al^{3+} close to H$^+$	56.8	2.7	44.5	0.095
Td Al^{3+} close to La^{3+}	53.1	3.1	55.5	0.118
Seperate EFAL phase[b]	-	-	-	-

[a] Based on the total Al concentration as determined by AAS.

[b] Separated extra-framwork Al phase.

Characterization of adsorption properties of BEA catalysts
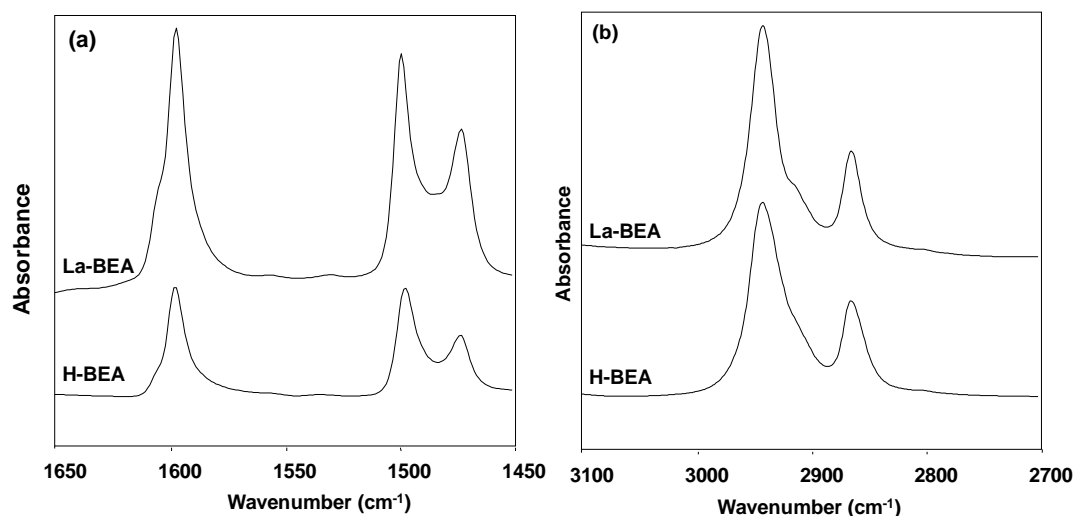

Figure 5-5. IR sgpectra of adsorbed (a) phenol and (b) cyclohexanol on
H-BEA and La-BEA from the gas phase at 313 K (*p* = 0.5 mbar).

The adsorption properties of H-BEA and La-BEA were investigated in the presence of 0.5 mbar of gas phase organic reactants at 313 K (Figure 5-5). La-BEA had triple the capacity of H-BEA for adsorption of phenol (at the representative adsorption of

$1610\,\mathrm{cm}^{-1}$) at these conditions (Figure 5-5a). This suggests that alkaline La^{3+} cations adsorbed acidic phenol more strongly than acidic protons did. The adsorption capacities for cyclohexanol (at the representative adsorption of $2950\,\mathrm{cm}^{-1}$), however, were equal on La-BEA and H-BEA (Figure 5-5b). In general, the intrinsic properties of La-BEA led to much higher adsorption of the reactant phenol and intermediate cyclohexanol.

5.3.2. Catalytic reaction measurements

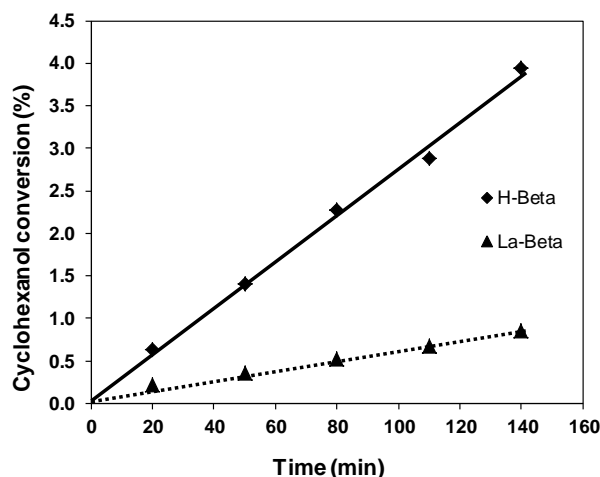*Kinetics of cyclohexanol dehydration on H-BEA and La-BEA.*

Figure. 5-6 Cyclohexanol conversion with H-BEA (solid line) and La-BEA (dased line) as a function of time. Reaction conditions: cyclohexanol (60 g), catalyst (0.040 g), H_2O (80 ml), 473 K, 4 MPa H_2 (ambient temperature), stirred at 700 rpm.

Cyclohexanol dehydration in liquid water catalyzed by H-BEA or La-BEA yielding only cyclohexene was measured with a very high substrate to catalyst ratio in batch mode at 473 K as a function of time (Figure 5-6). To use conditions analogous to hydroalkylation, hydrogen (4 MPa H_2) was introduced to each experiment before reaction. Cyclohexanol conversion to cyclohexene increased linearly with time (Figure 5-6), showing that the catalysts did not deactivate. The dehydration rate was 5 times higher with H-BEA ($0.23\,\mathrm{mol\,g^{-1}\,h^{-1}}$) than with La-BEA ($0.045\,\mathrm{mol\cdot g{-}1\cdot h{-}1}$) (Table 5-5). In our previous work, we showed that the BAS of HZSM-5 are the primary active sites for dehydration in the aqueous phase.[5,16] The dehydration TOFs (per mole of converted

reactant on per mole of active sites (BAS) per hour) on H-BEA and La-BEA were 1142 and 776 $mol \cdot mol_{BAS}^{-1} \cdot h^{-1}$, respectively, indicating that the introduction of La^{3+} moderately reduced the specific activity of the residual Brønsted acid sites.

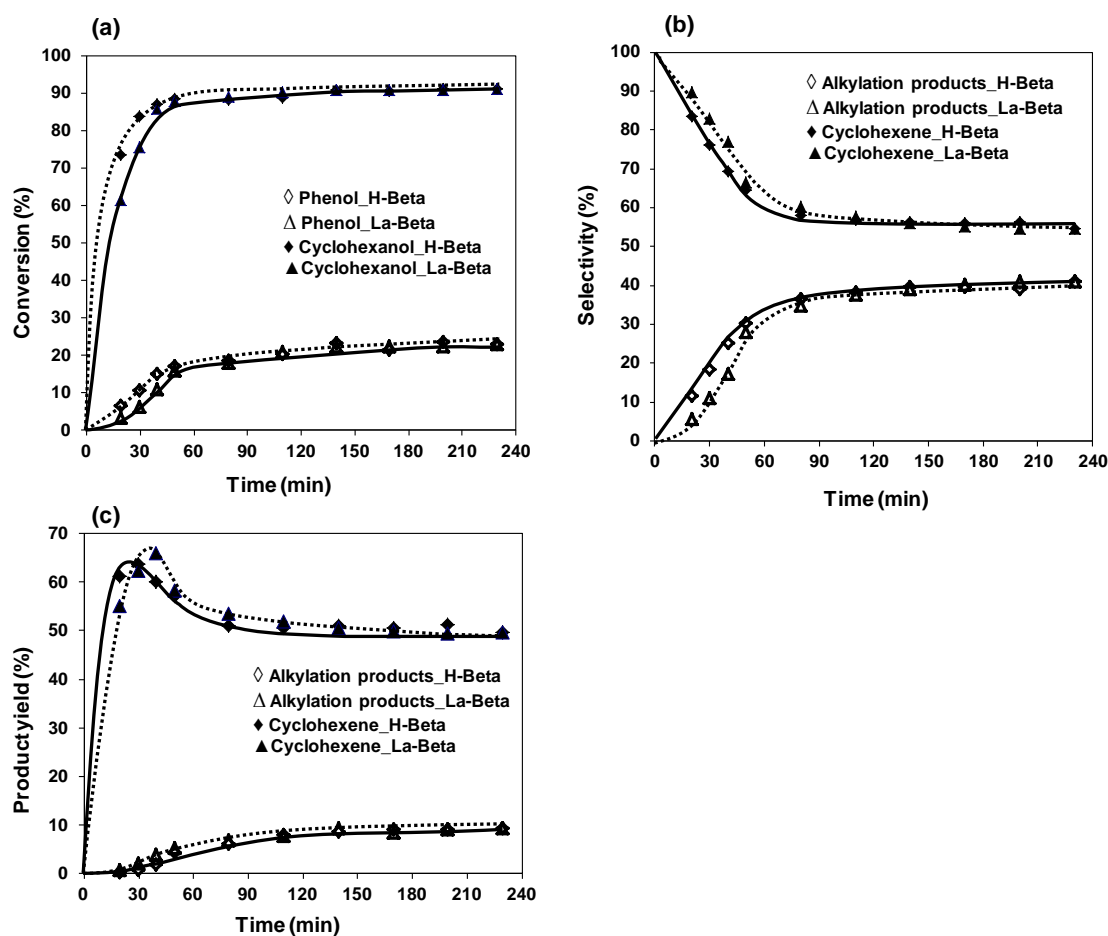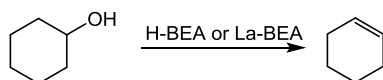*Kinetics of phenol−cyclohexanol alkylation on HBEA and La-BEA*

Figure 5-7. The product distribution from alkylation of phenol and cyclohexanol with H-BEA (solid line) or La-BEA (dashed line) as a function of time, (a) conversion, (b) selectivity, (c) yield. Reaction conditions: phenol (15 g), cyclohexanol (15 g), catalyst (0.40 g), H_2O (80 ml), 473 K, 4 MPa H_2 (ambient temperature), stirred at 700 rpm.

(1) Aquous phase dehydration of cyclohexanol

(2) Aquous phase alkylation of phenol with cyclohexanol
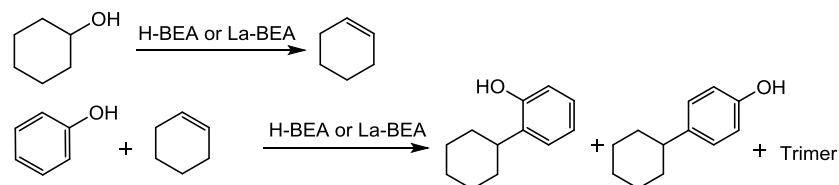
(3) Aquous phase hydroalkylation of phenol
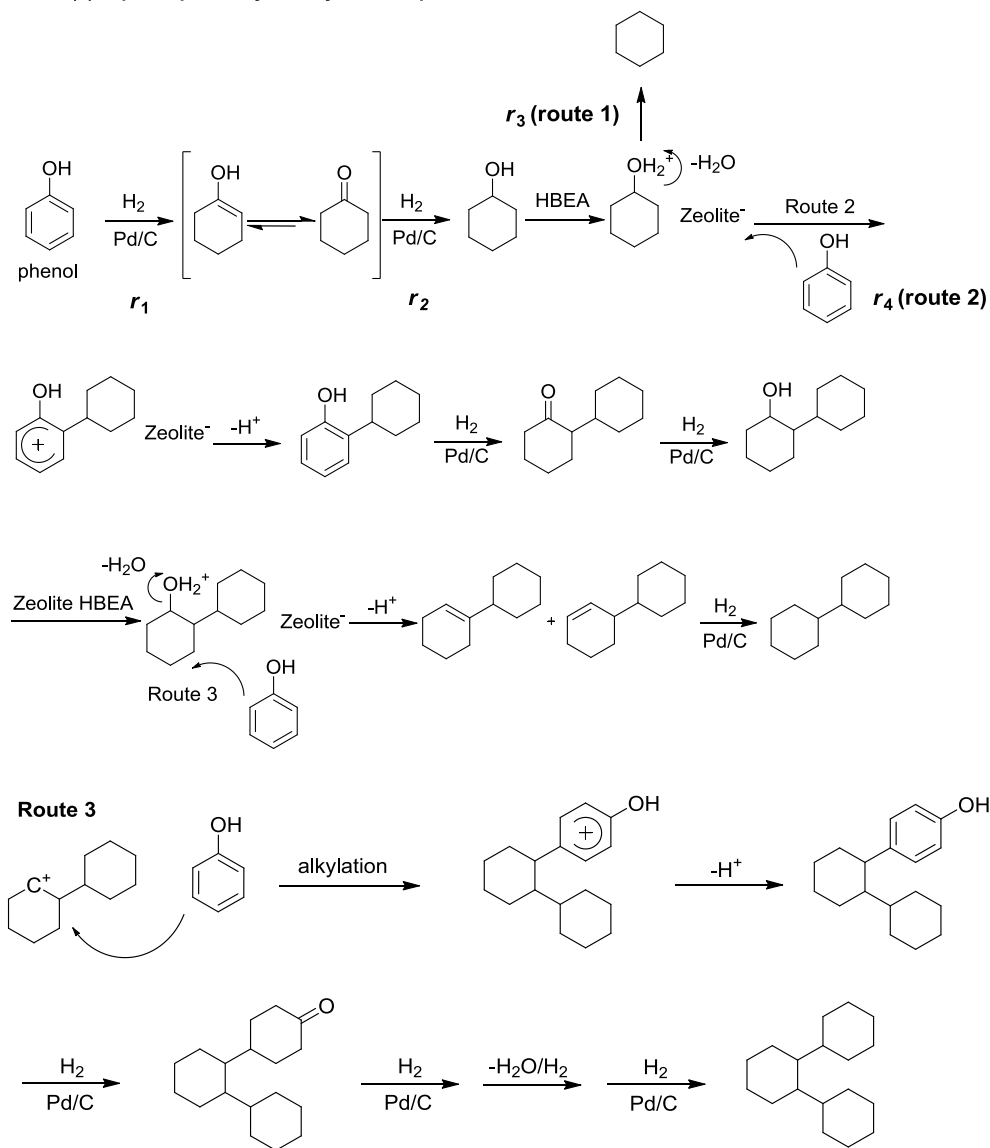
Scheme 5-1. Proposed pathways for dehydration of cyclohexanol, alkylation of phenol and cyclohexanol and hydroalkylation of phenol in aqueous phase.

The alkylation of phenol and cyclohexanol (1:1 molar ratio) was conducted in the aqueous phase using HBEA and La-BEA at 473 K (Figure 5-7). Two product groups were observed, i.e., cyclohexene, which was the dominating product, and 2- and 4-cyclohexylphenols, the products of alkylation. Both product groups approach equilibrium levels under the conditions measured; thus only the early stages of the reaction will be discussed.

The negligible selectivity to alkylated products at initial conversions indicates that alkylation proceeds firstly via cyclohexanol dehydration to cyclohexene (see Figure 5-7b and Scheme 5-1). The cyclohexanol and phenol conversions were 88 and 20%, respectively, with H-BEA or La-BEA catalysts after reaching the dehydration and alkylation equilibrium (reversible reaction) (Figure 5-7a). Thus, cyclohexanol was dehydrated to cyclohexene as a primary product, and alkylation occurred as a secondary reaction (Table 5-5). With time the cyclohexene selectivity decreased from 100 to 55%, as the cyclohexene was consumed in alkylation (Figure 5-7b). The yield of cyclohexene first increased to 65% over both catalysts and then decreased to 50% due to its further alkylation with phenol as the reaction time proceeded (see Figure 5-7c). The yields of alkylation products increased from 0 to 20% as the reaction time increased. The conversion rate and the selectivity toward alkylation were slightly higher in the case of H-BEA than with La-BEA, both reaching a value of $0.033 \, \mathrm{mol \, g^{-1} \, h^{-1}}$. It should be emphasized that the TOFs of alkylation were 1791 and $5690 \, \mathrm{mol \, mol_{BAS}^{-1} \, h^{-1}}$ for H-BEA and La-BEA, respectively, indicating a higher intrinsic activity in the presence of La^{3+} (see also Table 5-5).

Kinetics of phenol hydroalkylation−deoxygenation on H-BEA and La-BEA in the presence of Pd/C

When the Pd/C hydrogenation catalyst is combined with H-BEA or La-BEA (acting as solid acid), the conversion of phenol becomes more complex. Phenol can be hydrogenated to cyclohexanol (designated $r_1 + r_2$); then it is either dehydrated to cyclohexene, which is rapidly hydrogenated to cyclohexane (designated r_3), or alkylated with phenol to form 2- and 4-cyclohexylphenols (designated r_4). The latter compound or

heavier alkylation products can be deoxygenated through dehydration and hydrogenation to form the final C_{12} and C_{18} cycloalkanes (Scheme 5-1).[7]
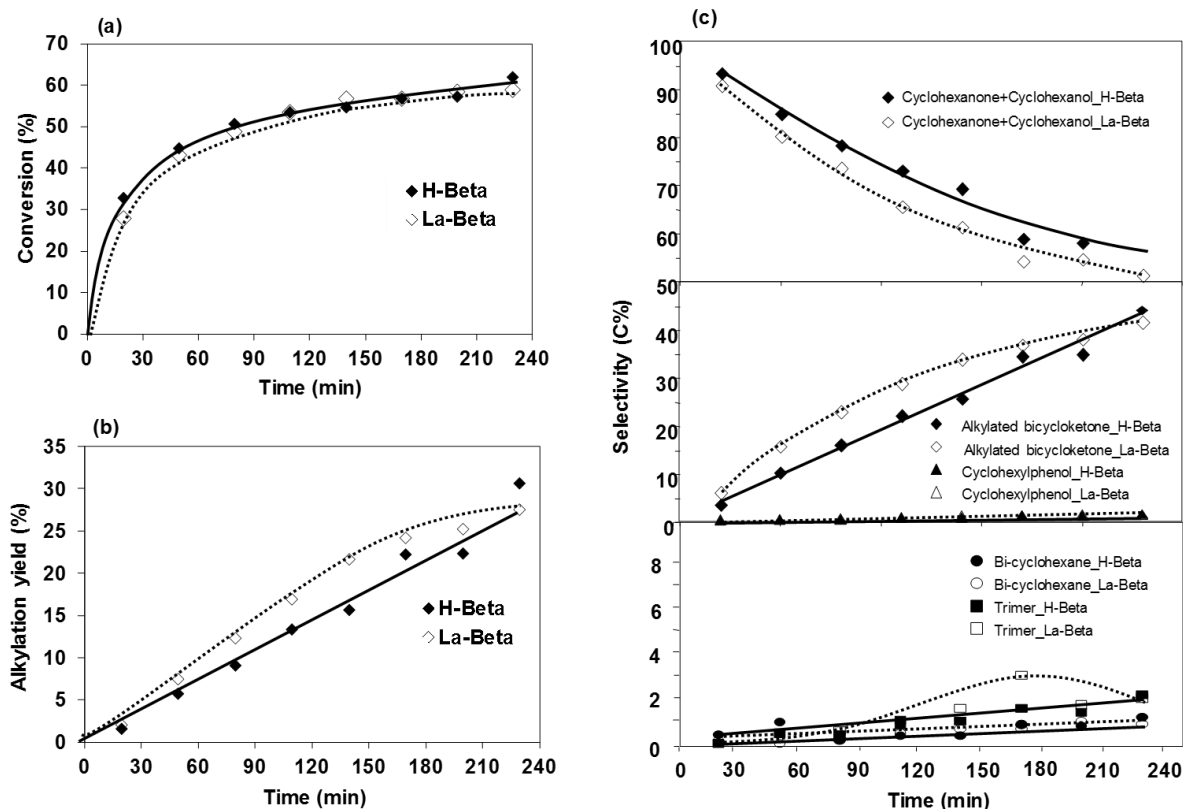

Figure 5-8. Product distributions from phenol hydroalkylation with Pd/C and H-BEA (solid line) or La-BEA (dashed line) as a function of time. Reaction conditions: phenol (15 g), solid acid (0.20 g), Pd/C (0.040 g), H_2O (80 ml), 473 K, 4 MPa H_2 (ambient temperature), 700 rpm.

As shown in Figure 5-8a, the phenol conversion reached 60% and the alkylation yield reached 25% on both catalysts within 200 min. The initial product was cyclohexanol with 100% selectivity at t = 0 (Figure 5-8c), decreasing to 50% due to alkylation leading ultimately to bicyclohexane and tricyclohexane. As the alkylation rate (0.036 mol g^{-1} h^{-1}) was much slower than the hydrogenation rate (1.0 mol g^{-1} h^{-1}) in the presence of H-BEA (Table 5-5), alkylated phenol was not detected, but partially hydrogenated cyclohexyl-cyclohexanone (CCN) was the major product, increasing to 45% selectivity with increasing reaction time.

In addition, deoxygenated bicyclohexane and cyclohexyl trimer were observed with 1−3% selectivities from Pd/C and H-BEA or La-BEA catalysts. The hydroalkylation rates on La-BEA in the presence of Pd/C reached 0.046 $mol_{alkylation}$ g^{-1} h^{-1}, which was higher than the rate with H-BEA (0.034 $mol_{alkylation}$ g^{-1} h^{-1}). The hydrodeoxygenation selectivity to cyclohexane was lower than 1.5% (Figure 5-8c), indicating that the cyclohexanol intermediate is preferentially alkylated with phenol rather than being dehydrated (and hydrogenated).

Comparison of initial rates in the coupled reactions of hydrogenation, dehydration, alkylation, and hydroalkylation

Table 5-5a. Initial rates of hydrogenation of phenol over Pd/C. [3]

Reaction	Pd/C
Hydrogenation of phenol with Pd/C	r_1
Rate $(mol·g^{-1}·h^{-1})$	1.0
TOF $(mol·mol_{Pd\ surf.}^{-1}·h^{-1})$	4200
Hydrogenation of cyclohexanone with Pd/C	r_2
Rate $(mol·g^{-1}·h^{-1})$	5.1
TOF $(mol·mol_{Pd\ surf.}^{-1}·h^{-1})$	21000

Table 5-5b. Initial rates of dehydration, alkylation and hydroalkylation
of cyclohexanol and phenol on H-BEA and La-BEA.

Reaction	H-BEA	La-BEA
Dehydration of cyclohexanol on BEA (r_3)		
Rate $(mol·g^{-1}·h^{-1})$	0.23	0.045
TOF $(mol·mol_{BAS}^{-1}·h^{-1})$	1142	776
Alkylation of phenol and cyclohexanol on BEA (r_4)		
$Rate_{alkylation}$ $(mol_{alkylation}·g^{-1}·h^{-1})$	0.036	0.033
$TOF_{alkylation}$ $(mol_{alkylation}·mol_{BAS}^{-1}·h^{-1})$	1791	5690
Hydroalkylation of phenol with acid and Pd/C		
Rate $(mol_{alkylation}·g^{-1}·h^{-1})$	0.034	0.046

Hydrogenation, dehydration, and alkylation proceed in tandem during phenol hydroalkylation over bifunctional catalysts. The initial rates are compiled in Table 5-5. The rates of hydrogenation of phenol and cyclohexanone over Pd/C were 1.0 and 5.1 mol g^{-1} h^{-1}, respectively. On HBEA, the rate of dehydration of cyclohexanol was 0.23 mol g^{-1} h^{-1}, and the rate of alkylation of phenol by cyclohexanol was 0.036 mol g^{-1} h^{-1}. By comparison, the dehydration and alkylation rates in the presence of La-BEA were 0.045 and 0.033 mol g^{-1} h^{-1}, respectively. This result shows that though the isolated dehydration activity may be quite different, the alkylation activity is comparable on two BEA catalysts, suggesting that isolated dehydration is catalyzed by protons in BEA catalyst without a significant effect of the presence of La^{3+}, but that the alkylation activity of Brønste acid sites is enhanced by La^{3+}.

In the phenol hydroalkylation with Pd/C and H-BEA or La-BEA without cyclohexanol as a supplied co-reactant, hydrogenation controlled the concentration ratio of phenol to cyclohexanol reactants during the working conditions. The excess of phenol drove the alkylation if the hydrogenation conversion was slow. However, too slow hydrogenation conversion supplied insufficient cyclohexanol, resulting in even lower alkylation rates. Therefore, the ratio of metal sites catalyzing hydrogenation to acid sites catalyzing dehydration and alkylation has to be optimized. In a previous report, only Pd showed high phenol hydroalkylation selectivity in the presence of H-BEA in water.[7] Other metals such as Pt, Ru, Rh, and Ni directly catalyzed cyclohexane formation from phenol through hydrogenation−dehydration. The slow alkylation reaction requires a long contact time for the alkylating molecules to achieve high conversion. The Pd hydrogenation catalyst that sustains a high concentration of the cyclohexanone intermediate enables a relatively higher rate of alkylation. In our previous contribution,[7] the optimized phenol/Pd ratios were in the range 2254−4508 mol/mol at 473 K, attaining 67−85% yields of alkylation products. When the phenol/Pd ratio was lowered to 564 mol/mol, the dominant product was cyclohexane (yield 98%). On the basis of the calculated individual hydrogenation rates on phenol and cyclohexanone over Pd/C (see Table 5-5), it can be estimated that after 0.5 h the ratio of phenol/cyclohexanol was ca. 9:1, if the phenol/Pd ratio was 2254 (0.040 g of 5 wt. % Pd/C and 4.0 g of phenol). Such a

high ratio of phenol to cyclohexanol during the conversion would enhance the alkylation efficiency in phenol self-hydroalkylation.

Subsequent to phenol hydrogenation, the dehydration and alkylation of cyclohexanol took place in parallel. In a previous study,[7] we have concluded that H-BEA with a high concentration of Brønsted acid sites such as H-BEA 25 (Si/Al = 12.5) was more selective to alkene formation, but H-BEA150 (Si/Al = 75) favored a higher alkylation selectivity.

In addition, the ratio of metal to acid sites was also crucial for determining the product distribution; that is, a very small amount of H-BEA (0.1 g, in the presence of 0.04 g of 5 wt. % Pd/C) was ineffective for cyclohexanol dehydration at 433 K, but the increasingly added concentrations of H-BEA 150 (0.1−1.0 g) preferred to dehydrate cyclohexanol (63% selectivity), and subsequently the added H-BEA 150 concentrations (1.0−2.0 g) took alkylation precedence over dehydration at attaining an alkylation selectivity of 36%. Therefore, in the previous study,[7] the optimized metal to acid ratio to enhance hydroalkylation selectivities, i.e., the Pd to H^+ ratio was 1/22 mol/mol, suggesting that acid sites are more abundant than metal sites in the dual function catalysts. The maximum productivity would be reached if the hydrogenated product, cyclohexanol, is quantitatively consumed as it is formed. On the basis of the individual rates one would estimate the ratio of Pd to H^+ to be 1/21, i.e., adjusting the alcohol formation rates from phenol with Pd/C (TOF = 5.1 mol $mol_{Pd\ surf.}^{-1}\ h^{-1}$) to match the rate of its consumption by alkylation (TOF = 1791 $mol_{alkylation}\ mol_{BAS}^{-1}\ h^{-1}$) with H-BEA (see Table 5-5). This matches well with the experimental ratio of 1/22.

In essence, if the alkylation selectivity with cyclohexanol needs to be enhanced, the dehydration rates should be retarded, as the dehydrated cyclohexene is swiftly and in part irreversibly converted to cyclohexane. The challenge lies in the fact that for the hydroalkylation of phenol both critical reactions are catalyzed by Brønsted acid sites. Hence, the specific activity of the alkylation function has to be enhanced and employing a catalyst selective to alkylation is crucial for determining the final product distribution. In a comparison, HBEA shows higher dehydration rates, but catalyzes almost identical alkylation rates, compared to La-BEA. Thus, in the sequence of parallel dehydration and alkylation reactions, La-BEA delivers higher selectivity to alkylation. In addition, the higher adsorption of phenol and cyclohexanol on the surface of La-BEA (Figure 5-5)

further increases the alkylation rates. The experimental results also support this hypothesis (Figure 5-8b,c), that La-BEA is more selective for hydroalkylation.

Fitting phenol hydroalkylation in the kinetics model

Scheme 5-2 simplifies the elementary reactions involved in the phenol hydroalkylation in the presence of dual functional catalysts. It starts with partial hydrogenation of phenol to cyclohexanone (referred to as "A"), which is formed from keto−enol tautomerism of cyclohexene-ol (referred to as "B"), and cyclohexanone can be fully hydrogenated to cyclohexanol (referred to as "C"). Cyclohexanol can be either dehydrated/hydrogenated to cyclohexane (referred to as "D") or alkylated with phenol (A) to heavier products (referred to as "E").
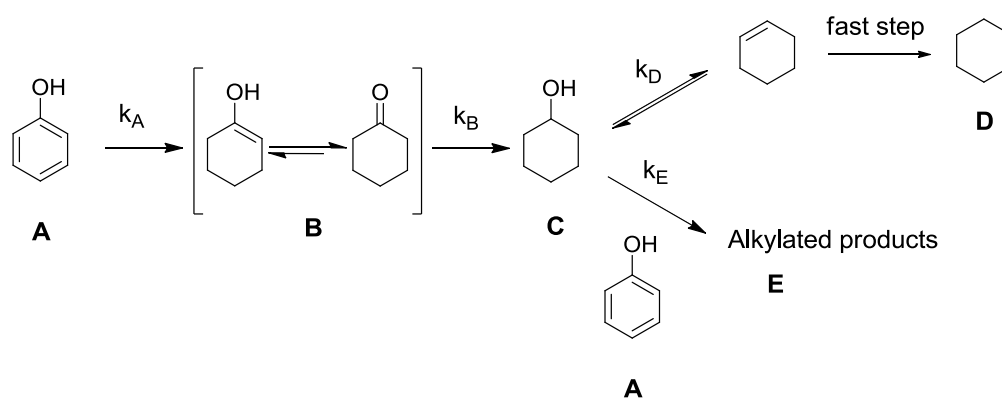
Scheme 5-2. Reaction sequence for phenol hydroalkylation including hydrogenation, dehydration, and alkylation elementary steps.

Table 5-6. Rate constants used for fitting phenol hydroalkylation.

	k_A (h^{-1})	k_B (h^{-1})	k_D (h^{-1})	k_E (h^{-1})
Pd/C, H-BEA	0.15	0.17	0.060	0.046
Pd/C, La-BEA	0.14	0.16	0.015	0.042

The differential kinetic rate equations involved in the phenol hydroalkylation are the following:

$$\frac{d[A]}{d\tau} = -k_A [A] - k_E [A][C]$$

$$\frac{d[B]}{d\tau} = k_A [A] - k_B [B]$$

$$\frac{d[c]}{d\tau} = k_B [B] - k_D [C] - k_E [C]$$

$$\frac{d[D]}{d\tau} = k_D [C]$$

$$\frac{d[E]}{d\tau} = k_E [C][A]$$

The rate of consumption of A

$$-r_A = \frac{d[A]}{d\tau} = -k_A [A] - k_E [A][C]$$

has a unit of mol h^{-1}, k is a rate constant with a unit of h^{-1}, and [A] is the concentration of phenol during the reaction.

Table 5-6 displays the used apparent rate constants (the product of the true rate constant and the adsorption equilibrium constant of the reactant) for fitting phenol hydroalkylation with Pd/C, HBEA, or La-BEA in the kinetic model (for reaction conditions, see Figure 5-8). The simulation results are in good agreement with the experimental data, suggesting that the proposed mechanism and kinetic model for phenol hydroalkylation and hydrodeoxygenation are reasonable. The fitted results (Figure 5-9) indicate that the concentration of reactant phenol (A) continuously decreases and the hydrogenated cyclohexanone and cyclohexanol (B + C) appear as the primary products, while alkylation (E) and hydrodeoxygenation products (D) occur as the secondary products. These fitted data show that k_A, k_B, and k_E are comparable but k_D on H-BEA is 4 times greater than that on La-BEA, while the BAS on H-BEA is consistently 4 times higher compared to that on La-BEA. Thus, it supports the hypothesis that the protons on BEA catalyze alcohol dehydration without a strong positive impact of La^{3+}, but that in the presence of La^{3+} the catalytic activity of Brønsted acid for alkylation is enhanced.

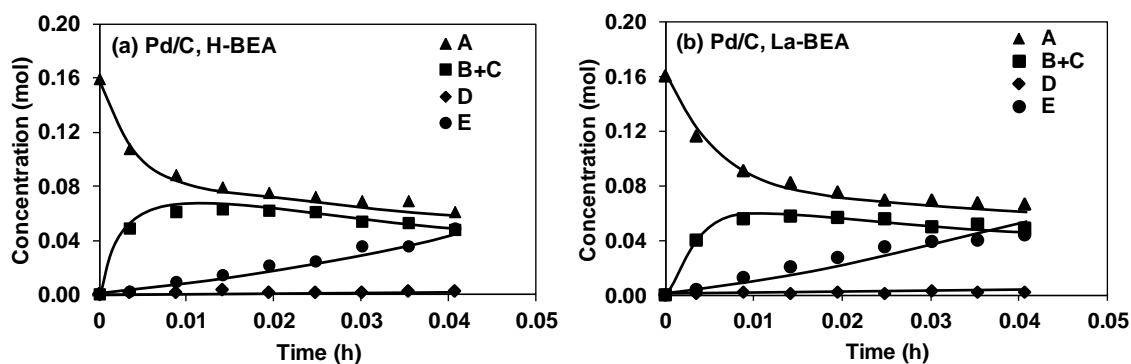**Figure 5-9.** Kinetics from the experiment data (solid points)
and fitted curves from the kinetics model (solid line).
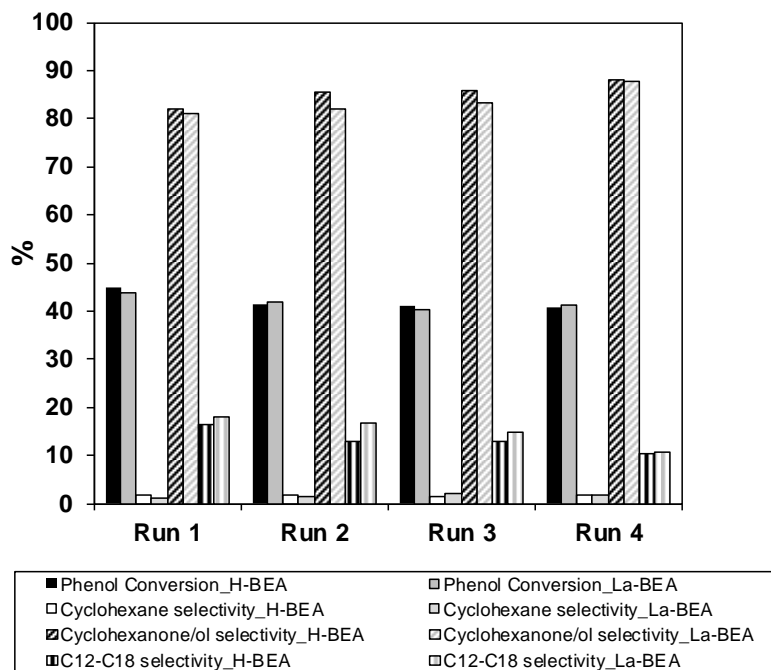
5.3.3. Catalyst recycling test

Figure 5-10. Catalytic recycling with Pd/C and H-BEA or La-BEA for hydroalkylation
of phenol. Reaction conditions: phenol (20 g), H-BEA or La-BEA (0.4 g), Pd/C (0.080 g), H_2O
(80 ml), 473 K, 6 MPa H_2 (reaction temperature), 0.5 h, and stirring at 700 rpm.

To test the catalyst stability for phenol hydroalkylation at the hydrothermal conditions used, the activities were examined in four consecutive catalytic runs employing the same aliquot of catalyst (Figure 5-10). The recycling data showed that the activities of used catalysts did not decrease during four catalytic runs, attaining ca. 40% conversions and selectivities of 20% hydroalkylation and 80% hydrodeoxygenation in each run. This result indicates that the combination of metal and acid catalysts had high activity and stability under hydrothermal conditions.

After reaction the color of zeolites H-BEA and La-BEA had changed from white to orange. As the used zeolite was more abundant than Pd/C, the color of the Pd/C did not obscure the change of zeolite color. The yellow compounds were extracted into acetone and analyzed by MALDI-TOF mass spectrometry. The obtained MALDI-TOF-MS spectrum (Appendix) showed that the yellow compounds are likely an oligomeric product mixture such as the polyphenol nuclear compounds formed by bialkylation with phenol. The heavier compounds were formed in low amounts (carbon balance in the reaction exceeded 95%), and the nearly unchanged activities during the recycling (Figure 5-10) indicated that such polymers did not block the active sites for phenol hydroalkylation.

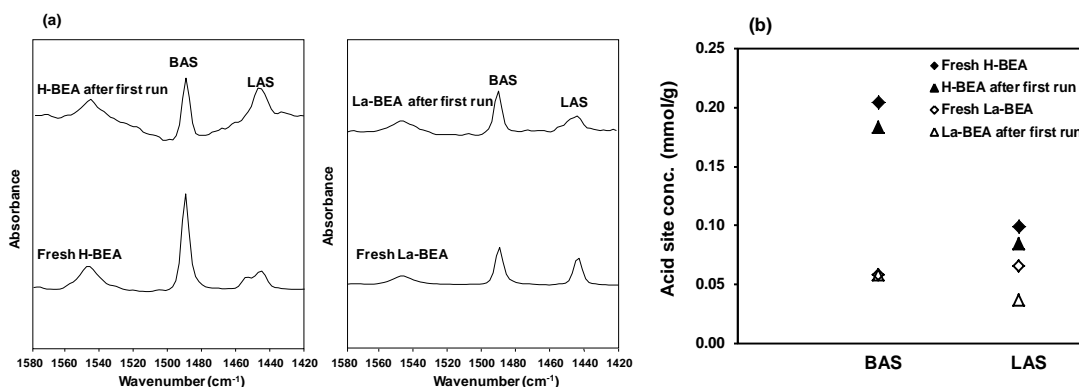**Figure 5-11.** (a) IR spectra of adsorbed pyridine and (b) acid site distribution on the fresh and used catalysts.

The acid sites of used H-BEA and La-BEA were also measured by IR spectroscopy of adsorbed pyridine and compared to the fresh catalysts (Figure 5-11a). The values determined for Brønsted and Lewis acid sites were plotted in Figure 5-11b. For H-BEA, BAS and LAS were both slightly decreased. For La-BEA the BAS were almost

unchanged, but the LAS decreased by 50% due to the hydrothermal reaction and recycling treatment (Figure 5-11b). BAS sites are active for dehydration in aqueous phase[16]; thus the acid catalyzed dehydration and alkylation reactivity with H-BEA or La-BEA was preserved due to retention of BAS sites during the four runs.

5.4. Conclusions

In the phenol hydroalkylation with catalysts Pd/C and H-BEA or La-BEA, hydrogenation, dehydration, and alkylation proceed together. The hydrogenation rate controls the ratio of alkylation reactants, i.e., phenol and cyclohexanol. A high ratio of phenol to cyclohexanol promotes the alkylation, which requires in turn the hydrogenation to be slow relative to the phenol concentrations. Additionally, the ratio of metal to acid sites, in the present case 1:21 Pd/H^+ for the combination of Pd/C and H-BEA, has to be adjusted to be able to attain comparable cyclohexanol formation rates from phenol hydrogenation and consumption rates from alkylation with phenol.

Following the phenol hydrogenation step, the subsequent dehydration/hydrogenation and alkylation of cyclohexanol compete. La-BEA was proved to be more selective for hydroalkylation, probably due to the dominant alkylation over dehydration in the cascade reactions. While La^{3+} does not exert a significant influence on Brønsted acid sites for dehydrogenation, it positively influences their catalytic activity for alkylation. The catalysts did not deactivate during four catalytic runs, suggesting that such catalyst combination is stable in hot water under selected conditions.

5.5. Acknowledgements

5.6. Appendix
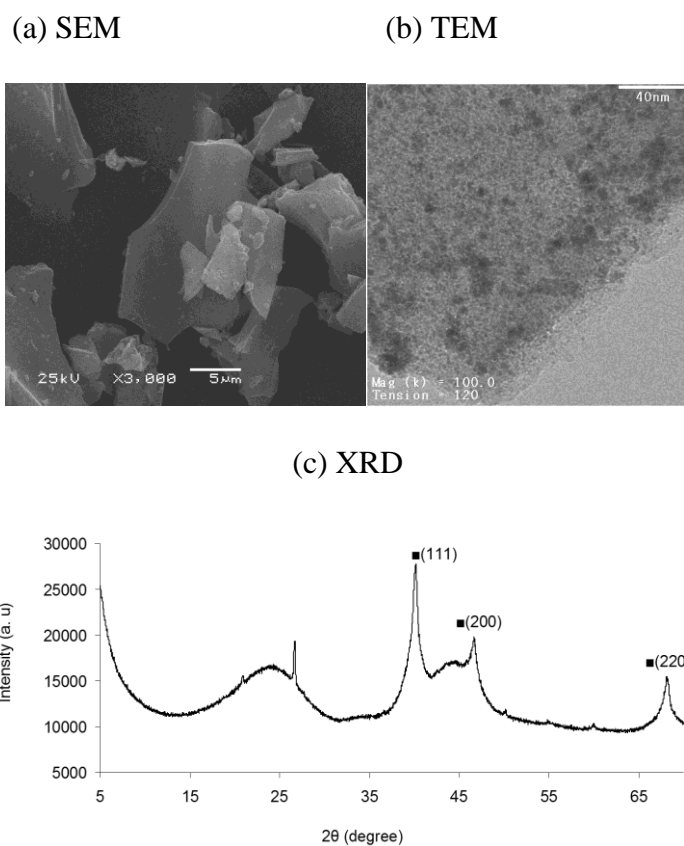
(a) SEM   (b) TEM

(c) XRD

Figure 5A-1. Characterization of (a) SEM, (b) TEM, (c) XRD on 5 wt.% Pd/C.

Table 5A-1. Surface area and pore volume information of Pd/C.

	Pd/C
Element composition	
Pd (wt.%) (AAS)	5.0
BET surface area ($m^2 \cdot g^{-1}$)	1062
Mesopore surface area ($m^2 \cdot g^{-1}$)	90
Micropore surface area ($m^2 \cdot g^{-1}$)	972
Pore volume ($cm^3 \cdot g^{-1}$)	0.54
Mesopore volume ($cm^3 \cdot g^{-1}$)	0.12
Micropore volume ($cm^3 \cdot g^{-1}$)	0.42
Mean pore diameter (nm)	3.7

Figure 5A-2. The MALDI-TOF-MS spectrum of the yellow compounds (anthrahydroquinone) produced from phenol hydroalkylation with Pd/C and H-BEA catalysts.
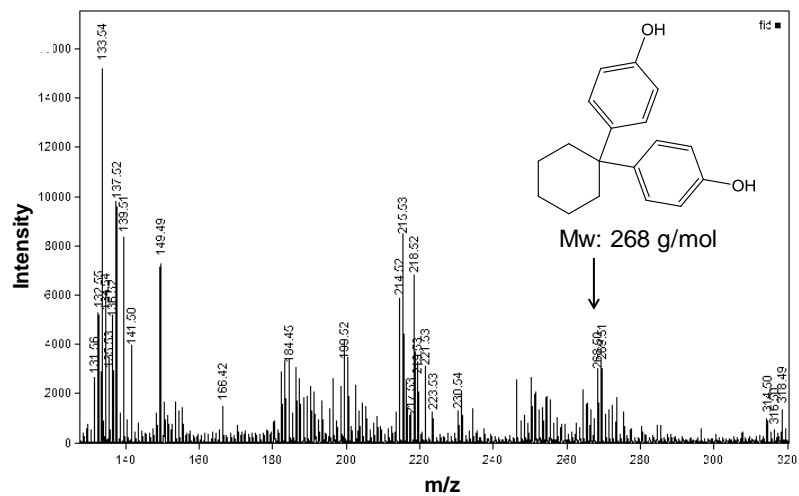
5.7. References

[1]   Corma, A.; Iborra, S.; Velty, A. *Chem. Rev.* **2007,** *107,* 2411.

[2]   Zhao, C.; Kou, Y.; Lemonidou, A. A.; Li, X.; Lercher, J. A. *Angew. Chem. Int. Ed.* **2009**, *48,* 3987.

[3]   Zhao, C.; He, J.; Lemonidou, A. A.; Li, X.; Lercher, J. A. *J. Catal.* **2011,** *280,* 8.

[4]   Zhao, C.; Kou, Y.; Lemonidou, A. A.; Li, X.; Lercher, J. A. *Chem. Commun.* **2011***, 46*, 412.

[5]   Hong, D. Y.; Miller, S. J.; Agrawal, P. K.; Jones, C. W. *Chem. Commun.* **2010,** *46,* 1038.

[6]   Zhao, C.; Lercher, J. A. *Angew. Chem. Int. Ed.* **2012,** *51,* 5935.

[7]   Zhao, C.; Camaioni, D.; Lercher, J. A. *J. Catal.* **2012,** *288*, 92.

[8]   Crossley, S.; Faria, J.; Shen, M.; Resasco, D. E. *Science* **2010,** *327*, 68.

[9]   Sitthisa, S.; An, W.; Resasco, D. E. *J. Catal.* **2011,** *284,* 90.

[10] Zhu, X.; Lobban, L.L.; Mallinson, R. G.; Resasco, D. E. *J. Catal.* **2011,** *281*, 21.

[11] Vispute, T. P.; Zhang, H.; Sanna, A.; Xiao, R.; Huber, G. W. *Science* **2010,** *330,* 1222.

[12]   Gaare, K.; Akporiaye, D. *J. Phys. Chem. B* **1997,** *101,* 48.

[13]   Sievers, C.; Onda, A.; Olindo, R.; Lercher, J. A. *J. Phys. Chem. C* **2007,** *111*, 5454.

[14]   Sheemol, V. N.; Tyagi, B.; Jasra, R. V. *J. Mol. Catal. A* **2004***, 215,* 201.

[15]   Sievers, C.; Liebert, J. S.; Stratmann, M. M.; Olindo, R.; Lercher, J. A. *Appl. Catal. A: Gen* **2008,** *336,* 89.

[16] Peng, B.; Zhao, C.; Mejá-Centeno, I.; Fuentes, G. A.; Jentys, A.; Lercher, J. A. *Catal. Today* **2012,** *183,* 3.

Chapter 6

Summary and Conclusions

The aim of this thesis is to synthesize small and uniform nickel nanoparticles supported on zeolites as bifunctional catalysts for the hydrodeoxygenation of microalgae oil and phenolic compounds derived from lignin depolymerization. The hydroalkylation of phenol over dual functional Pd/C and zeolite BEA is also investigated for the completeness of the kinetic studies, as it represents a new route to produce heavier hydrocarbons from sugar or phenolic compounds based bio-oil by combining oxygen removal process with the C–C coupling of the reactive intermediates. The focuses are 1) relating the superior performances of the improved Ni/HBEA catalysts to the intrinsic properties of metal nanoparticles, 2) understanding the individual and cooperative roles of metal and acid sites in the bifunctional catalyst, 3) clarifying individual reaction steps in the integrated reaction network occurred during hydrodeoygenation of microalgae oil and substituted phenols.

Compared with conventional impregnation technique (d = 24.7 ± 12.8 nm), nickel nanoparticles incorporated into zeolite by deposition-precipitation (DP) method are much smaller and more uniformly distributed (d = 2.5 ± 0.7 nm). Formation of surface nickel silicate/aluminate during the improved synthesis routes leads to stronger metal-support interaction which effectively prevents sintering of nanoparticles during the reduction treatment and catalytic reactions. Lower concentrations of Brønsted acid sites (BAS) caused by their partial exchange with Ni^{2+} cations involved in the two precipitation processes do not influence the hydrodeoxygenation rates, but alter the products distribution with lower selectivity to isomerized alkanes and higher selectivity towards decarbonylation product. Small-sized Ni nanoparticles facilitate high initial activity in the fresh sample and good size uniformity ensures catalyst stability for the prolonged usage.

During the cascade reactions of microalgae oil conversion, dehydration of the intermediately formed 1-octdecanol is dependent on the nature and stabilities of surface intermediates as well as the locations of Brønsted and Lewis acidic sites in the BEA zeolite. The long alkyl chain of C_{18} alcohol strongly interacts with the zeolite pores, causing an inefficient utilization of BAS especially in samples with high concentrations of acid sites. A dimer mediated mechanism is proposed for dioctadecyl ether formation (inter-molecular dehydration), with a lower apparent activation energy in comparison to

octadecene formation (intra-molecular dehydration) which proceeds via surface-bound alkoxide species. The energy barrier for the rate-limiting step of alkene formation is independent of location based on DFT calculations. Whereas the sterically demanding formation of dioctadecyl ether is concluded to take place mainly on BAS and LAS at the pore mouth or the external surface, respectively. At 533 K, octadecene is the primary dehydration product over H-BEA, the dioctadecyl ether formed at the beginning is quickly further converted. Moreover, weak LAS suffice to catalyze ether formation while BAS are required for the dehydration towards alkenes or further cleavage of dioctadecyl ether.

The DP method is also applied to prepare the bifunctional Ni/HZSM-5 catalyst which is employed to explore the hydrodeoxygenation of phenol, catechol and guaiacol in the aqueous phase. The C-O bond cleavage of phenol on Ni/HZSM-5 proceeds similarly as catalyzed by Pd in the presence of aqueous mineral acids, with primary hydrogenation of the aromatic ring followed by cyclohexanol dehydration and subsequent cyclohexene hydrogenation. For catechol and guaiacol conversion, Ni catalyzes hydrogenolysis of the C–O bonds in addition to arene hydrogenation. Catechol is converted by parallel hydrogenation (forming cyclohexane-1,2-ol, 89%) and hydrogenolysis (forming phenol, 11%). The C–O bond of cyclohexane-1,2-diol is readily cleaved either by hydrogenolysis over Ni, or by dehydration and pinacol rearrangement on acid sites. Guaiacol undergoes primarily hydrogenolysis (75%) to phenol, and the hydrogenation producing 2-methoxycyclohexanol accounts for only 25%. 2-Methoxycyclohexanol reacts further either via hydrogenolysis by Ni to cyclohexanol or via acid catalyzed demethoxylation and rearrangement steps. The hydrodeoxygenation activities of the phenolic monomers are much higher than their respective saturated analogues, due to the more stringent steric constraints imposed by the sp^3 hybridized orbitals. Moreover, the presence of proximal acid sites remarkably increases the activities of Ni by a synergistic action, with the initial turnover frequency (TOF) of phenol hydrodeoxygenation increases in parallel with the acid site concentration.

In addition to hydrodeoxygenation route towards the production of cyclohexane, phenol also undergoes hydroalkylation over Pd/C and BEA zeolite in the aqueous phase.

During the reaction, phenol is first hydrogenated by metal particles, followed by competitive dehydration and alkylation of in situ formed cyclohexanol catalyzed by acid sites. The alkylation step is favored at a high phenol to cyclohexanol ratio, which requires a relatively slow phenol hydrogenation step. An optimized H^+/Pd ratio is 21, as it facilitates comparable rates of cyclohexanol formation via phenol hydrogenation and consumption by alkylation with phenol. Compared with parent H-BEA, La-BEA is more selective for hydroalkylation due to the lowered concentration of Brønsted acid sites which leads to a suppressed dehydration step in the cascade reactions.

In conclusion, the comprehensive knowledge of various preparation methods and in-depth understanding of individual reaction kinetics will allow us to prepare bifunctional catalysts with carefully adjusted active metal and acid sites which can balance the rates of sequential or parallel individual steps in the overall cascade reactions. This would open new possibilities to design tailored and stable catalysts for highly selective conversion of biomass feedstocks into green (free of sulfur, oxygen, and polyaromatics), sustainable, and high-grade transportation fuels.

Chapter 7

Zusammenfassung und Folgerungen

Das Ziel dieser Arbeit ist kleine und einheitliche Nickel Nanopartikel zu synthetisieren, welche auf Zeolithen, als bifunktionellen Katalysatoren zur Hydrodeoxygenierung von Mikroalgenöl und phenolische Komponenten aus der Depolymerisation von Lignin stammend, getragen sind. Zur Vollständigkeit der kinetischen Untersuchungen wird auch die Hydroalkylierung von Phenol auf bifunktionellem Pd/C und Zeolith BEA untersucht, weil es eine neue Route repräsentiert, schwerere Kohlenwasserstoffe aus Zucker oder phenolischen Komponenten zu produzieren, welche auf Bioöl basieren, indem Deoxygenierung mit C-C Verknüpfung von reaktiven Intermediaten kombiniert wird. Die Schwerpunkte sind 1) das überlegene Verhalten der verbesserten Ni/HBEA Katalysatoren mit den intrinsischen Eigenschaften der Metall Nanopartikel zu verbinden, 2) die einzelne und zusammenwirkende Funktion des Metalls und des Säurezentrums des bifunktionellen Katalysators zu verstehen, 3) die einzelnen Reaktionsschritte des gesamten Reaktionsnetzwerkes aufzuklären, welche bei der Hydrodeoxygenierung von Mikroalgenöl und substituierten Phenolen auftreten.

Verglichen mit konventioneller Imprägnierungstechnik (d = 24,7 $\pm$ 12,8 nm) sind Nickel Nanopartikel, die in einen Zeolithen durch DP-Methode ("Deposition-Precipitation") inkorporiert sind, viel kleiner und einheitlicher verteilt (d = 2,5 $\pm$ 0,7 nm). Die Bildung von Nickelsilikaten/-aluminaten auf der Oberfläche während der verbesserten Syntheseart führt zu stärkerer Metall-Träger-Wechselwirkung, welche effektiv das Sintern von Nanopartikeln während der reduktiven Behandlung und der katalytischen Reaktion verhindern. Niedrigere Konzentrationen von Brønsted-sauren Zentren (BAS), verursacht durch ihren teilweisen Austausch mit Ni^{2+} Kationen, welche in den beiden Fällungsschritten beteiligt sind, beeinflussen die Raten der Hydrodeoxygenierung nicht, aber verändern die Produktverteilung hin zu niedrigerer Selektivität von *iso*-Alkanen und höherer Selektivität von decarbonylierten Produkten. Kleine Ni Nanopartikel ermöglichen hohe Anfangsaktivität der frischen Proben und gute Homogenität der Größe garantiert Katalysatorstabilität für einen anhaltenden Gebrauch.

Während der Kaskadenreaktion der Umsetzung von Mikroalgenöl ist die Dehydratisierung des sofort gebildeten 1-Octadecanols von der Art und Stabilität der Oberflächen Intermediate, sowie der Position der Brønsted- und Lewis-sauren Zentren

des BEA Zeoliths abhängig. Die lange Alkylkette des C_{18} Alkohols wechselwirkt stark mit den Poren des Zeoliths, was zu einer ineffizienten Nutzung von BAS führt – besonders in Proben mit hoher Konzentration an Säurezentren. Ein Dimer vermittelter Mechanismus wird zur Bildung eines Di-octadecylethers (intramolekulare Dehydratisierung) angenommen, welcher im Vergleich zur Bildung von Octadecen (intramolekulare Dehydratisierung) eine geringere apparente Aktivierungsenergie besitzt und über eine auf der Oberfläche gebundene Spezies erfolgt. Nach DFT-Berechnungen ist die Energiebarriere des geschwindigkeitsbestimmenden Schrittes der Bildung des Alkens unabhängig vom Ort. Hingegen kann gefolgert werden, dass die sterisch anspruchsvolle Bildung des Di-octadecylethers hauptsächlich an den BAS und LAS der Porenöffnung bzw. der äußeren Oberfläche stattfindet. Bei 533 K ist Octadecen das primäre Dehydratisierungsprodukt auf H-BEA. Der zu Beginn gebildete Di-octadecylether wird schnell weiter umgesetzt. Darüber hinaus sind schwache LAS ausreichend um die Etherbildung zu katalysieren, während BAS für die Dehydratisierung zum Olefin oder weitere Spaltung des Di-octadecylethers notwendig sind.

Die DP-Methode wird auch angewandt um bifunktionelle Ni/HZSM-5 Katalysatoren darzustellen, welche eingesetzt werden um die Hydrodeoxygenierung von Phenol, Catechol und Guajacol in Wasserphase zu untersuchen. Die C-O-Bindungsspaltung von Phenol auf Ni/HZSM-5 verläuft ähnlich wie auf Pd in Gegenwart einer wässrigen Mineralsäure, indem zuerst der aromatische Ring hydriert wird, gefolgt von der Dehydratisierung von Cyclohexanol und der anschließenden Hydrierung von Cyclohexen. Bei der Umsetzung von Catechol und Guajacol katalysiert Ni die Hydrogenolyse der C-O-Bindung zusätzlich zur Hydrierung des Aromaten. Catechol wird durch parallele Hydrierung (Bildung von Cyclohexan-1,2-diol; 89%) und Hydrogenolyse (Bildung von Phenol; 11%) umgesetzt. Die C-O-Bindung von Cyclohexan-1,2-diol wird leicht, entweder durch Hydrogenolyse an Ni oder Dehydratisierung und Umlagerung von Pinacol an sauren Zentren, gespalten. Guajacol unterliegt primär Hydrogenolyse zu Phenol (75%) und die Hydrierung, welche 2-Methoxycyclohexanol bildet, macht nur 25% aus. 2-Methoxycyclohexanol reagiert entweder über Hydrogenolyse durch Ni zu Cyclohexanol oder saure katalysierte Demethoxylierung und Umlagerungsschritten weiter. Die Aktivität bezüglich Hydrodeoxygenierung der phenolischen Monomere ist

viel höher als die der entsprechenden gesättigten Analoga, weil die sp^3-hybridisierten Orbitale viel strengere sterische Einschränkungen auferlegen. Darüber hinaus erhöht die Anwesenheit von nahegelegenen Säurezentren die Aktivität von Ni durch eine synergistische Wirkung beträchtlich, indem die anfängliche Wechselzahl (TOF) der Hydrodeoxygenierung von Phenol parallel mit der Konzentration der Säurezentren steigt.

Zusätzlich zur Hydrodeoxygenierungsroute für die Darstellung von Cyclohexan wird Phenol auf Pd/C und BEA-Zeolith in wässriger Phase hydroalkyliert. Während der Reaktion wird Phenol zuerst durch Metallpartikel hydriert, gefolgt von der kompetitiven Dehydratisierung und Alkylierung von in situ gebildetem Cyclohexanol, welches durch saure Zentren katalysiert wird. Der Alkylierungsschritt wird bei hohem Phenol-Cyclohexanol-Verhältnis bevorzugt, was eine relativ langsame Geschwindigkeit der Phenol Hydrierung erfordert. Das optimierte H^+/Pd-Verhältnis ist 21, indem es, durch Hydrierung von Phenol und Umsetzung bei der Alkylierung mit Phenol, vergleichbare Raten der Bildung von Cyclohexanol ermöglicht. Im Vergleich zu der Vorstufe H-BEA ist La-BEA selektiver bezüglich Hydroalkylierung wegen der niedrigeren Konzentration von Brønsted-sauren Zentren, was in der Kaskadenreaktion zu einem unterdrücktem Dehydratisierungsschritt führt.

Schließlich wird uns das umfassende Wissen über verschiedene Präparationsmethoden und tiefgreifendes Verständnis der einzelnen Reaktionskinetiken ermöglichen, bifunktionelle Katalysatoren mit genau eingestellten aktiven Metall- und Säurezentren darzustellen, welche die Raten der einzelnen seriellen- oder parallelen Schritte in der Gesamtreaktionskaskade ausgleichen. Dies würde neue Möglichkeiten eröffnen, maßgeschneiderte und stabile Katalysatoren zur hochselektiven Umsetzung von nachwachsenden Rohstoffen zu grünen (frei von Schwefel, Sauerstoff und Polyaromaten), nachhaltigen und hochwertigen Kraftstoffen zu entwickeln.

Curriculum Vitae

Wenji Song was born on March 31st 1987 in Suzhou, P. R. China. During her studies at Suzhou High School, she won the silver medal in the provice-wide high school chemistry competition, and was admitted into the School of Chemical & Biomedical Engineering at Nanyang Technological University (Singapore) in August 2015 with the wavier of Entrance examination, A levels and bridging courses. She persued the Accelerated Bachelor Programme in Engineering with a minor in business and graduated in February 2009 with the thesis entitled *"Fabrication of Organic Thin Film Transistor (OTFT)"*. Since August of the same year, she studied as a master student in the Industrial Chemistry program jointly offered by National University of Singapore and Technische Universität München (Germany), when she was awarded *"GIST-DAAD scholarship"* by German Academic Exchange Service in both academic semesters. In March 2011, she received her master degree in Science with high distinction. She did her master thesis *"n-Pentane Conversion over Steamed H-ZSM5 Zeolite"* under the supervision of Prof. Johannes A. Lercher, at the Chair of Technical Chemistry II at Technische Universität München, where she continued to study catalysis and started her Ph. D. thesis in May 2011. Her recent research interests are the selective conversion of biomass derived feedstocks into hydrocarbons over bifunctional catalysts based on metal nanoparticles and zeolites, with a focus on the kinetics of individual reaction steps.

List of Publications

Journals

Chen Zhao, <u>Wenji Song</u>, and Johannes A. Lercher* *"Aqueous phase hydroalkylation and hydrodeoxygenation of phenol by dual functional catalysts comprising of Pd/C and H/La-BEA", ACS Catal.* **2012,** *2,* 2714-2723.

<u>Wenji Song</u>, Chen Zhao,* and Johannes A. Lercher* *"Importance of size and distribution of Ni nanoparticles for hydrodeoxygenation of microalgae oil", Chem. Eur. J.* **2013,** *19,* 9833-9842. [Cover paper]

<u>Wenji Song</u>, Yuanshuai Liu, Eszter Bar áth, Chen Zhao,* and Johannes A. Lercher* *"Synergistic effects of Ni and acid sites for hydrogenation and C−O bond cleavage of substituted phenols", Green Chem.* **2015,** *17,* 1204-1218.

<u>Wenji Song</u>, Yuanshuai Liu, Eszter Bar áth, Lucy Wang, Chen Zhao, Donghai Mei,* and Johannes A. Lercher* *"Dehydration of 1−octadecanol over H-BEA: A combined experimental and computational study",* submitted to *ACS Catal.* **2015**.

Poster Presentations

<u>Wenji Song</u>, Baoxiang Peng, Chen Zhao, and Johannes. A. Lercher* *"Ni nanoparticles supported on HBEA by diverse preparation methods and their catalysis in deoxygenation of steraic acid",* 45. Jahrestreffen Deutscher Katalytiker, Weimar (Germany), 03/2012.

<u>Wenji Song</u>, Yuanshuai Liu, Chenz Zhao, Johannes. A. Lercher* *"Understanding the relation between metal and acid sites for C-O bonds cleavage of phenol and its derivatives",* 46. Jahrestreffen Deutscher Katalytiker, Weimar (Germany), 03/2013.